

NORTHWESTERN UNIVERSITY

Quantitative Study of Granular Flow, Mixing, and Segregation Using the  
Discrete Element Method (DEM)

A DISSERTATION

SUBMITTED TO THE GRADUATE SCHOOL  
IN PARTIAL FULFILLMENT OF THE REQUIREMENTS

for the degree

DOCTOR OF PHILOSOPHY

Field of Chemical Engineering

By

Pengfei Chen

EVANSTON, ILLINOIS

December 2008

© Copyright by Pengfei Chen 2008

All Rights Reserved

## ABSTRACT

Quantitative Study of Granular Flow, Mixing, and Segregation Using the Discrete Element Method (DEM)

Pengfei Chen

Granular materials exhibit a wide variety of fascinating physical properties that can be observed both in nature and industry. The goal of this work is to better understand the flow, mixing, and segregation of granular materials in a prototypical system, the rotating tumbler, using numerical modeling, specifically, the Discrete Element Method (DEM). Three topics are considered.

First, we study the subsurface flow field of mono-disperse particles in half-full cylindrical tumblers with different axial lengths: quasi-2D, as well as short and long tumblers. Our results show that the flow field is significantly altered near endwall regions. Simulations with longer tumblers or tumblers with one frictionless endwall clearly indicate that this phenomenon is a direct result of endwall friction and that it extends less than one tumbler radius ( $R$ ) from the endwall. When frictional endwalls are closer than  $2R$ , these regions merge partially (for the short tumbler) or completely (for the quasi-2D tumbler).

The onset mechanism of axial segregation in long cylindrical tumblers forms the second aim of study. Particular attention is focused on the axial flow field of two species during the development of axial segregation. Results show a small axial flow between segregation bands, a result which was not reported before. The mechanism for axial segregation is identified as arising from the non-uniform distribution of axial velocity and species concentration on transverse planes.

The third topic is axial segregation in spherical tumblers which is examined both experimentally and numerically. Two different patterns are observed: for low fill levels, band of large particles appear at the equator; for high fill levels, the opposite occurs. The fill level of the tumbler at which the transition occurs varies depending on particle size and rotational speed of the tumbler. DEM simulations produce identical results and particle trajectories indicates different flow performances of two species of particles in the two reversed segregation patterns.

## Acknowledgements

First I would like to thank my advisors, Professor Julio M. Ottino and Professor Richard M. Lueptow, for introducing me to the fascinating field of granular physics. I deeply appreciate their patient instructions and continuous support they have given me during my study and research at Northwestern University.

I would also like to express my gratitude to my fellow group members for their helpful discussions and support: Ashley G. Smart, Benjamin L. Severson, R. Dean Malmgren, Gabriel Juarez, Ivan Christov, Prof. Jiajun Wang, Nick Pohlman, Stanley J. Fiedor, Stephen E. Cisar, and Steven M. Meier. In addition, I thank Bryan Lochman for enjoyable research collaborations with him.

I thank my family and friends for their love and encouragement. Finally, I would especially like to thank my wife, Ying Zhou, for her continuing support and patience. I dedicate this dissertation to her.

## Table of Contents

ABSTRACT	3
Acknowledgements	5
List of Figures	8
Chapter 1. Introduction	14
1.1. Why Study Granular Materials and Segregation?	15
1.2. Systems Investigated	16
1.3. Thesis Outline	28
Chapter 2. Methodology	29
2.1. Numerical Methods often Used in Granular Physics	29
2.2. Implementation of DEM in the Simulations	44
2.3. Handling of Data Structure to Speed Simulations	47
Chapter 3. Subsurface Granular Flow in Rotating Tumblers: A Detailed Computational Study	51
3.1. Introduction	52
3.2. Numerical Parameters	55
3.3. Flowing Layer Structure Beneath the Visible Free Surface	58
3.4. Streamwise Velocity Field Beneath the Visible Free Surface	63
3.5. Velocity Fluctuations Beneath the Visible Free Surface	70
3.6. Axial Velocity in the Tumbler	76
3.7. Conclusions	81

Chapter 4. The Onset of Granular Axial Segregation in Rotating Cylindrical Tumblers	85
4.1. Introduction	86
4.2. Numerical Parameters	89
4.3. Axial Segregation Structure	90
4.4. Axial Drift Velocity Field during Axial Segregation	94
4.5. Axial Flow Rate during Axial Segregation	102
4.6. Axial Segregation without Endwalls	112
4.7. Conclusions	117
Chapter 5. Inversion of Band Patterns in Spherical Tumblers	120
5.1. Introduction	120
5.2. Experimental Results	121
5.3. Numerical Simulation Results	125
5.4. Conclusions	138
Chapter 6. Outlook	140
References	144
Appendix A. Discussion of Negative Diffusivity in Axial Segregation	156

## List of Figures

1.1	Coordinate system in a cylindrical tumbler.	19
1.2	Experimental pictures of four flow regimes of granular materials in a rotating tumbler.	19
1.3	Various kinds of rotating tumblers used in the thesis.	21
1.4	Examples of segregation of particles of differing sizes (S-systems) and densities (D-systems) in circular tumblers rotated within the continuous flow regime.	23
1.5	Example of axial segregation of particles of differing sizes in a long cylindrical tumbler rotated around its horizontal axis.	25
1.6	MRI data for axial segregation of a mixture of small and large particles rotated in a long cylinder. From Hill <i>et al.</i> (1997 <i>b</i> ).	26
1.7	The space-time images of band dynamics of axial segregation experiments from Fiedor & Ottino (2003).	27
2.1	Comparison of degree of realism of physical description and ability to explore parameter space of the computational models.	30
2.2	Illustration of the collision between two particles.	36
2.3	Comparison of linear spring-dashpot force model and Hertz force model.	42

2.4	Illustration of the procedure to generate an initial random distribution of particles in a half full tumbler with two different sizes.	46
2.5	Comparison of the efficiency of two data structures to store the contact list in DEM simulation	50
3.1	Comparison of streamwise velocity $u(\text{m/s})$ from DEM simulation with experimental results.	57
3.2	Streamtraces of the particle flow on the free surface.	59
3.3	Boundaries of flowing layer for 1.5mm particles at $z = 0m$ in three tumblers.	60
3.4	Boundaries of flowing layer for 1.5mm particles at $x = 0m$ in three tumblers.	61
3.5	Flowing layer structure for 1.5mm particles at different depths for three tumblers.	64
3.6	Contours of streamwise velocity at different depths in the long tumbler of $L = 0.10m$ ( $L/D = 1.43$ ) for 1.5mm particles.	65
3.7	Contours of streamwise velocity at different depths in the long tumbler of $L = 0.10m$ ( $L/D = 1.43$ ) with a frictionless endwall at $z = -0.05m$ for 1.5mm particles.	66
3.8	Contours of streamwise velocity at different depths in the short tumbler of $L = 0.05m$ ( $L/D = 0.71$ ) for 1.5mm particles.	68
3.9	Contours of streamwise velocity at different depths in the quasi-2D tumbler of $L = 0.01m$ ( $L/D = 0.14$ ) for 1.5mm particles.	69
3.10	Contours of normalized streamwise velocity at different depths in the long tumbler of $L = 0.10m$ ( $L/D = 1.43$ ) for larger 3mm particles.	70

		10
3.11	Normalized streamwise velocity $u/u_o$ profiles at different depths in the long tumbler ( $L = 0.10m$ , $L/D = 1.43$ ) for 1.5mm particles.	71
3.12	Normalized velocity fluctuations on the free surface ( $y = 0m$ ) at $x = 0m$ , along the length of the three tumblers for 1.5mm particles.	73
3.13	Normalized velocity fluctuations on the free surface at $z = 0m$ along the streamwise direction of three tumblers for 1.5mm particles.	74
3.14	Comparison of profiles of the normalized velocity fluctuations along the depth at $x = 0m$ in the long tumbler ( $L = 0.10m$ , $L/D = 1.43$ ) for 1.5mm particles: at the center and near the endwall.	76
3.15	The axial flow fields at different depths in the long tumbler ( $L = 0.10m$ , $L/D = 1.43$ ) for 1.5mm particles.	78
3.16	Profile of the axial velocity along the $y$ direction at different axial positions at $x = -0.02m$ in the long tumbler ( $L = 0.10m$ , $L/D = 1.43$ ) for 1.5mm particles.	79
3.17	The free surface axial velocity at $x = -0.02m$ along the axial direction for 1.5mm particles matches near the frictional endwalls regardless of the tumbler length.	81
3.18	Free surface axial velocity along the streamwise direction and 0.01m from the frictional endwall for 1.5mm particles matches regardless of the tumbler length.	82
3.19	Axial velocity profile with depth at $x = -0.02m$ and 0.01m away from the frictional endwall for three cases with 1.5mm particles match, regardless of the tumbler length.	83
4.1	Evolution of the cross-sectionally averaged species concentrations along the axial length during the development of axial segregation.	91
4.2	Snapshots of slices at different axial positions at two representative times of axial segregation.	92

		11
4.3	Structures of small and large particle volumes at different times at two representative times of axial segregation.	94
4.4	Evolution of the velocity field on the free surface and below the surface during the development of axial segregation.	95
4.5	Different dynamic angles of repose of three representative cross sections at two times during the development of the axial segregation.	98
4.6	Comparison of axial velocities of two species at three representative positions during the development of the axial segregation (averaged over 4-5 rotations).	100
4.7	Comparison of axial velocities of two species at five representative positions during the further development of the axial segregation (averaged over 20-21 rotations).	101
4.8	Magnitude of the axial flow rate of the mixture in the upstream and downstream portions along the axial length during the development of axial segregation.	104
4.9	Comparison of the axial flow rate of the mixture in the upstream portion and concentration gradient of small particles averaged over two time periods of axial segregation.	106
4.10	The variance of generalized axial diffusivity with the development of axial segregation along the axial length during the development of axial segregation.	108
4.11	The magnitude difference of the axial flow rate of small particles in the upstream and downstream portions during the development of axial segregation.	110
4.12	Illustration of onset of axial segregation in the long tumbler.	111
4.13	Illustration of imbalance distribution of the axial flow rate of small and large particles in upstream and downstream portions during axial segregation.	112

4.14	Evolution of the cross-sectionally averaged species concentration along the axial length at different times for the periodic boundary conditions with $\omega = 3.14\text{radians/s}$ .	114
4.15	Evolution of the cross-sectionally averaged species concentration along the axial length at different times for the periodic boundary conditions with $\omega = 6.28\text{radians/s}$ .	115
4.16	Snapshots of slices at different axial positions at two times for the periodic boundary conditions with $\omega = 6.28\text{radians/s}$ .	116
4.17	Difference of dynamic angles of repose of two cross sections after 50 rotations for the periodic boundary conditions with $\omega = 6.28\text{radians/s}$ .	117
4.18	The velocity field over 49-50 rotations for the periodic boundary conditions with $\omega = 6.28\text{radians/s}$ on free surface and below the surface.	118
5.1	Two representative surface segregation patterns occur for $1\text{mm}$ black ( $S$ ) and $4\text{mm}$ clear ( $L$ ) glass beads rotated at $20\text{ rpm}$ about a horizontal axis.	122
5.2	Two axial segregation patterns depend on the fill level, the particle size ratio, and the absolute particle sizes.	124
5.3	Segregation patterns depend on the rotation rate.	125
5.4	Segregation patterns for the simulation after 100 rotations at $20\text{ rpm}$ for $2\text{mm}$ and $4\text{mm}$ particles in a $14\text{cm}$ diameter tumbler.	127
5.5	Snapshots of slices at different axial positions after the segregation has reached steady state.	128
5.6	Steady-state structures of small and large particle volumes averaged over $2/3$ rotations represented by the concentration of small particles.	130

5.7	Evolution of the concentration of small particles in a transverse cross-section along the axial length.	131
5.8	Evolution of the velocity field averaged from the flow of all particles on the free surface for <i>SLS</i> pattern and the axial velocity along the depth of individual species.	133
5.9	Evolution of the velocity field averaged from the flow of all particles on the free surface for <i>LSL</i> pattern and the axial velocity along the depth of individual species.	134
5.10	Trajectories of the <i>2mm</i> and <i>4mm</i> particles on the free surface for two segregation patterns at three times in simulation.	136
5.11	Trajectories of small and large particles on the free surface for mono-disperse systems at 20% full and 60% full.	137
A.1	Illustration of axial transport during axial segregation in cylindrical tumblers.	156

## CHAPTER 1

### **Introduction**

Granular matter is a prototype for collective systems far from thermodynamic equilibrium, and displays a variety of fascinating behaviors that have been observed in nature and industrial processing. Although in recent decades there has been an increased focus on the study of the physics of flowing granular materials, this area is far from being fully understood and at many levels the theoretical description of granular materials is still in its infancy. One of the most intriguing properties of granular materials is the tendency of the components in granular mixtures differing in the size or density to segregate when undergoing flow, vibration, or shearing. Segregation is often undesirable in industrial processing and has attracted much interest from the science and engineering community. However, the onset mechanisms for granular segregation have only been investigated qualitatively and under limited circumstances. The goal of this research is to provide a detailed quantitative analysis of granular flow, mixing, and segregation in long rotating tumblers, a commonly used industrial apparatus for granular material processing, as well as in spherical tumblers, which provide alternative endwall conditions. In this chapter, elements of the physics of granular segregation and the systems are introduced. It is followed by an outline of the thesis.

### 1.1. Why Study Granular Materials and Segregation?

The term “granular material” refers to a collective system consisting of macroscopic particles, which might be grains, sand or rocks in geomechanics, coal or minerals in mining, pills in the pharmaceutical industry, and planet dust in astrophysics. Granular materials are encountered across a wide range of natural and industrial situations, and an understanding of the physics of granular materials is important for multiple reasons. Although the interaction between a pair of granular particles is relatively well understood, many fundamental collective properties of granular materials, granular flow in particular, are still unclear. Granular materials often behave differently from regular liquids and solids (Jaeger & Nagel, 1992). A source of difficulty is the dissipative property of particle collisions, placing granular materials in the realm of a driven dissipative system far from thermodynamic equilibrium. Moreover, since the fluctuations are almost the same amplitude as the mean values, many properties of flowing granular systems cannot be adequately described by considering mean quantities. All of these facts indicate that a theoretical description of granular materials is far from simple or straightforward. For example, due to the discrete nature of granular systems there are no general, fundamental constitutive equations governing the rheology of granular materials that are applicable for all conditions.

A particularly challenging issue of granular physics is segregation. The tendency of granular materials varying in size, density, or shape to segregate during processing has caused substantial frustration in industry, since segregation works against the goal of mixing (Ottino & Khakhar, 2000). A variety of agitations such as flow (Oyama, 1939; Makse *et al.*, 1997; Clement *et al.*, 1995) or vibration (Rosato *et al.*, 1987) can cause

partial or complete granular segregation. Research on granular mixing and segregation is much less advanced than fluid mixing (Ottino, 1989) since there is no counterpart in granular physics theory that is analogous to the Navier-Stokes equations in continuum fluid mechanics. A large amount of theoretical, experimental, and computational work has been performed related to granular segregation as well as its underlying mechanisms in recent decades. Yet there are still many unanswered questions since most existing work on this topic is qualitative – quantitative analysis is still very limited. The work considered in this thesis concentrates on segregation in granular systems under flow mainly using numerical simulations. As a point of departure to understanding flow and segregation, this thesis also consider flow of mono-disperse granular materials.

## **1.2. Systems Investigated**

### **1.2.1. Categories of Systems**

Two classes of granular systems are often investigated: dry granular systems (DGS) and liquid granular systems (LGS). The difference between them is the interstitial medium. In DGS the medium is either vacuum or air and particle collisions dominate. In LGS particles are completely immersed in a less dense liquid and liquid viscosity may compete with or overwhelm particle collisions. With only a few exceptions, nearly all research on granular materials and flow in the last decades focused on DGS, although LGS are important in a wide range of practical industrial applications. Under a wide range of conditions in granular mixing and segregation, DGS and LGS have qualitatively similar dynamic behaviors (Fiedor & Ottino, 2003).

There are two main modes of granular segregation:

- Segregation due to shearing flow: segregation is caused by the relative flow of particles in shear (Oyama, 1939; Makse *et al.*, 1997; Clement *et al.*, 1995);
- Segregation from vibration, often vertical: the relative motion of the particles is introduced by shaking the container (Rosato *et al.*, 1987).

Factors that can give rise to segregation are:

- Difference in particle size;
- Difference in particle density;
- Difference in particle shape;
- Difference in particle resilience,

where the differences in particle size and density are by far the most important factors and other factors are comparatively unimportant, especially in industrial applications (Ristow, 2000).

Many different physical environments have been used to investigate mixing and segregation including chute flows and heaping (Ristow, 2000). Another common device is the rotating tumbler. As indicated by the work of the Groupement de Recherche Milieux Divisés (MiDi, 2004), the surface shearing motion of mono-disperse granular materials or bi-disperse granular mixtures in partially-filled rotating tumblers with a horizontal axis is often used to as a standard to study granular flow, mixing, and segregation.

This thesis focuses on the flow, mixing, and segregation of dry granular materials differing in size caused by the shearing flow in rotating tumblers. Many results and concepts described in this thesis can be extended beyond rotating tumblers.

### 1.2.2. Granular Flow in Rotating Tumblers

Let us consider a partially filled rotating tumbler. As tumbler rotation starts, the friction force between the tumbler walls and the granular particles inside the tumbler carries the granular bulk in solid body rotation (with minor rearrangements), and the angle of the surface of the bulk material relative to the horizontal plane increases as the rotation continues. At a critical value of the angle, the static force interactions between particles fail to sustain the gravitational force, and a granular flow occurs down the free top surface of the granular bed. As shown in figure 1.1, the flow field inside the tumbler has two distinct regions: a fixed (solid body) bed of particles rotating with the tumbler and a flowing layer along the free surface. Continuing particle transport between the solid body bed and the flowing layer makes a rotating tumbler an ideal controlled research setting, as the flow region is continuously being replenished, which is harder to achieve in chute and heaping flows, the other two devices often used for studying granular flow.

Henein *et al.* (1983) identified four different regimes of the flow of granular materials in rotating tumblers as the rotation rate is increased, depending on the Froude number of the system,  $F_r = \omega^2 R/g$ : avalanching, continuous, cataracting, and centrifuging, which are shown in figure 1.2. Here,  $\omega$  is angular velocity of rotation,  $R$  is radius of the tumbler, and  $g$  is the gravitational acceleration. The dimensionless Froude number represents the ratio of the centrifugal force to the gravitational force. At low rotational rates (small Froude numbers), the flow occurs in discrete avalanches. After each avalanche, which occurs at a critical slope called the angle of marginal stability,  $\theta_m$ , the bulk relaxes to a smaller slope called the angle of repose,  $\theta_r$ . As the tumbler continues to rotate, the system gradually increases the slope (accumulates gravitational potential) without flow

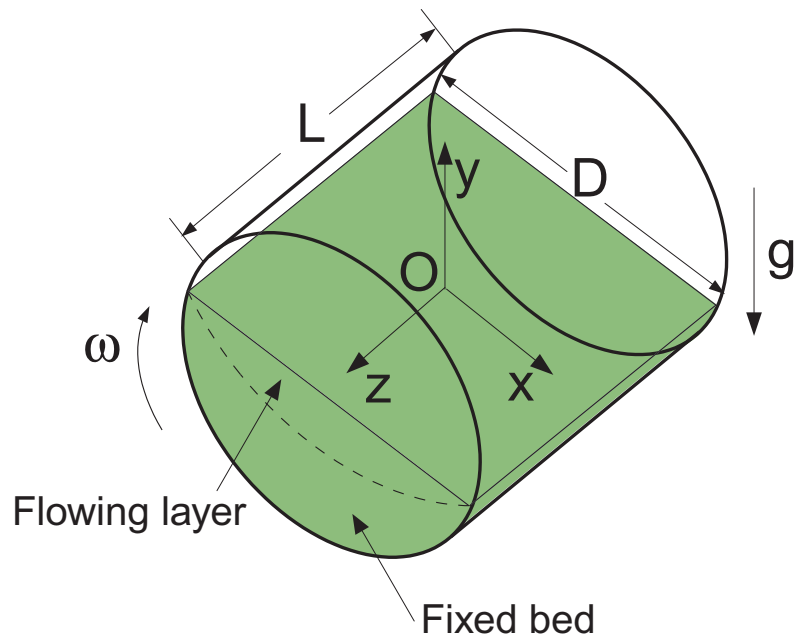


Figure 1.1. Coordinate system in a cylindrical tumbler. Rotational axis is the  $z$ -direction. Flow direction is along the  $x$ -direction.

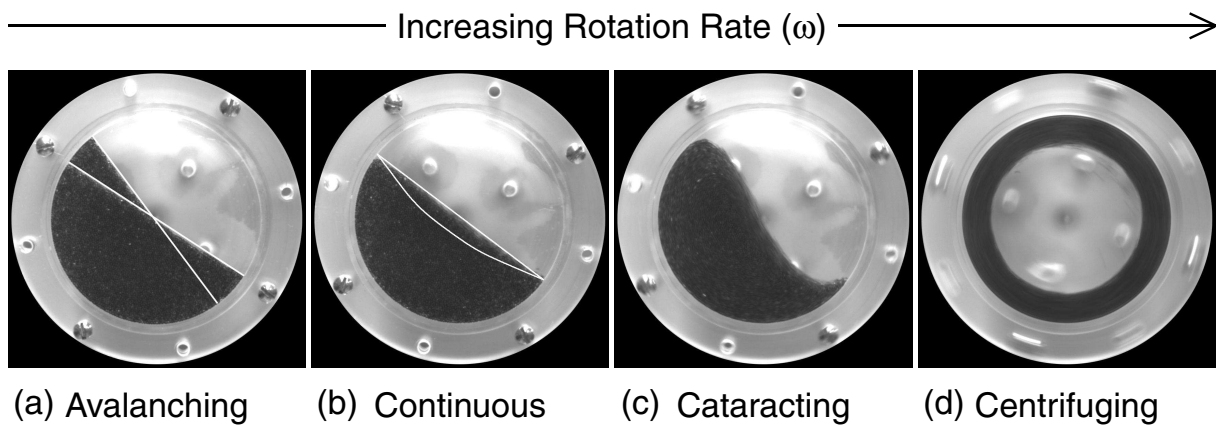


Figure 1.2. Experimental pictures of the four flow regimes of granular materials in a rotating tumbler (Fiedor, 2006).

again until the next avalanche, and so on. As the rotation rate is increased, the time between avalanches becomes smaller and smaller, so that a continuous surface flow (some people call this regime rolling or cascading) can be observed when discrete avalanches cannot be detected. The angle of the slope in this case is between  $\theta_m$  and  $\theta_r$ , the dynamic angle of repose,  $\theta_d$ . If the inertial effects are small, the free surface is nearly flat. At higher rotation rates, inertial effects become greater, and a curved ( $S$  - shaped) top surface occurs (see figure 1.2(c)), which is called the cataracting regime of flow. For  $F_r \geq 1$ , the centrifugal force is equal to or greater than the gravitational force, and all granular particles are pushed against the tumbler wall (see figure 1.2(d)). The motion is simply solid body rotation. This is the centrifuging regime.

We consider three types of rotating tumblers: a quasi-two-dimensional (quasi-2D) circular tumbler whose diameter is much larger than the tumbler length (figure 1.3(a)), a long three-dimensional (3D) cylindrical tumbler whose length is of the same order of magnitude or larger than the tumbler diameter (figure 1.3(b)), and a spherical tumbler (figure 1.3(c)).

### 1.2.3. Granular Segregation in Rotating Tumblers

Particle collisions in the flowing layer result in collisional diffusion which tends to mix particles. By contrast, in bi-disperse systems, granular materials with different properties tend to segregate into regions with a higher concentration of one species. Two types of striking granular segregation are observed in rotating tumblers for bi-disperse particles: radial segregation and axial segregation (Ristow, 2000). Radial segregation appears within a few rotations after the tumbler rotation starts. Then, over longer time scales ( $O(10-100)$

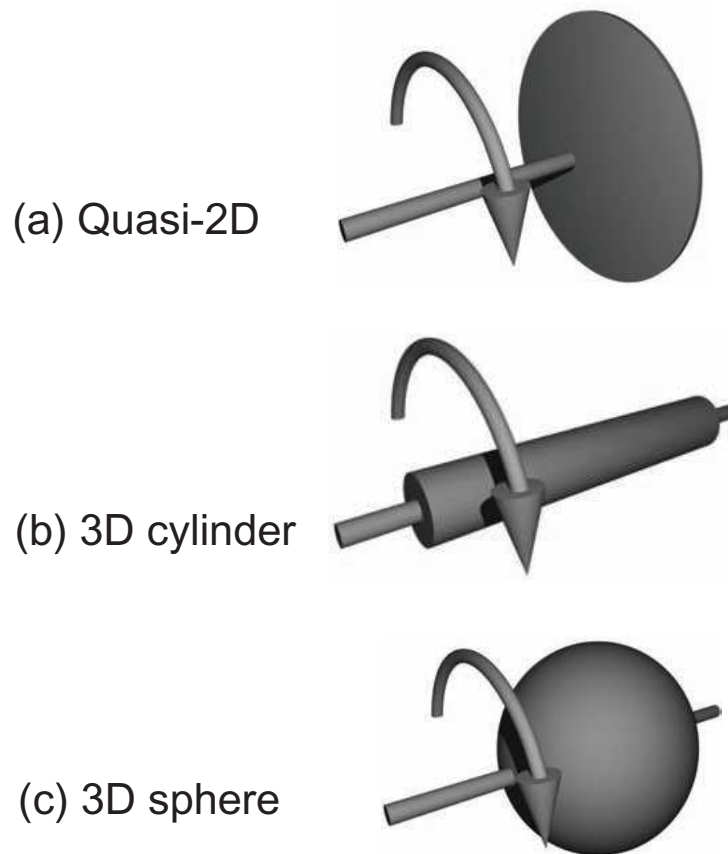


Figure 1.3. Various kinds of rotating tumblers used in the thesis. (a) Quasi-2D tumbler; (b) 3D cylindrical tumbler; (c) 3D sphere (Meier, 2008).

tumbler rotations), if the tumbler is long enough, a secondary segregation may occur as particles separate into more or less regularly spaced bands along the rotational axis. Due to the opacity of granular materials, the radial segregation is mainly studied through the clear end of quasi-2D tumblers and the axial segregation in long tumblers is mainly studied by the direct observation of the visible free surface.

Within the scope of radial segregation, two particular types of granular segregation have received the most attention, as depicted in figure 1.4: S-systems, where particles

have the same density but differ in size and D-systems where the same size particles have different densities. Nearly all studies of radial segregation to date have been restricted to these two types of binary systems. Radial segregation in D-systems is relatively simple (Khakhar *et al.*, 1997; Ristow, 1994): segregation occurs so that there is a core region of denser particles and lighter particles occupy the periphery of the tumbler. The mechanism underlying this phenomenon is “buoyancy.” As they flow in the flowing layer of a tumbler, denser particles tend to fall to lower levels than lighter ones, penetrate to the bottom of the flowing layer, and deposit near the middle of the length of the flowing layer as a segregated core. Lighter particles remain in the upper portion of the flowing layer and deposit near its end to surround the core of heavy particles.

Normally the segregation patterns in S-systems are similar to those in D-systems with a core region of smaller particles with larger particles around the periphery, as shown in figure 1.4. The accepted mechanism of size segregation is percolation, a term first used by Savage & Lun (1988) in studying the size segregation in chute flow. During flow the probability of forming a large void for larger particles to drop down is smaller than the probability of forming voids adequate for smaller particles. So the smaller particles are more likely to percolate downward through the voids in flowing layer and settle at the lower part of flowing layer eventually forming a core region. The percolation mechanism for the radial segregation in S-systems has been much investigated in the last decade: Clement *et al.* (1995) and Cantelaube & Bideau (1995) experimentally studied this kind of segregation in avalanches and continuous flow regimes; Dury & Ristow (1997) used the discrete element method to study computationally the dynamics and rate of segregation in S-systems by varying the angular velocity of the tumbler and the thickness of the

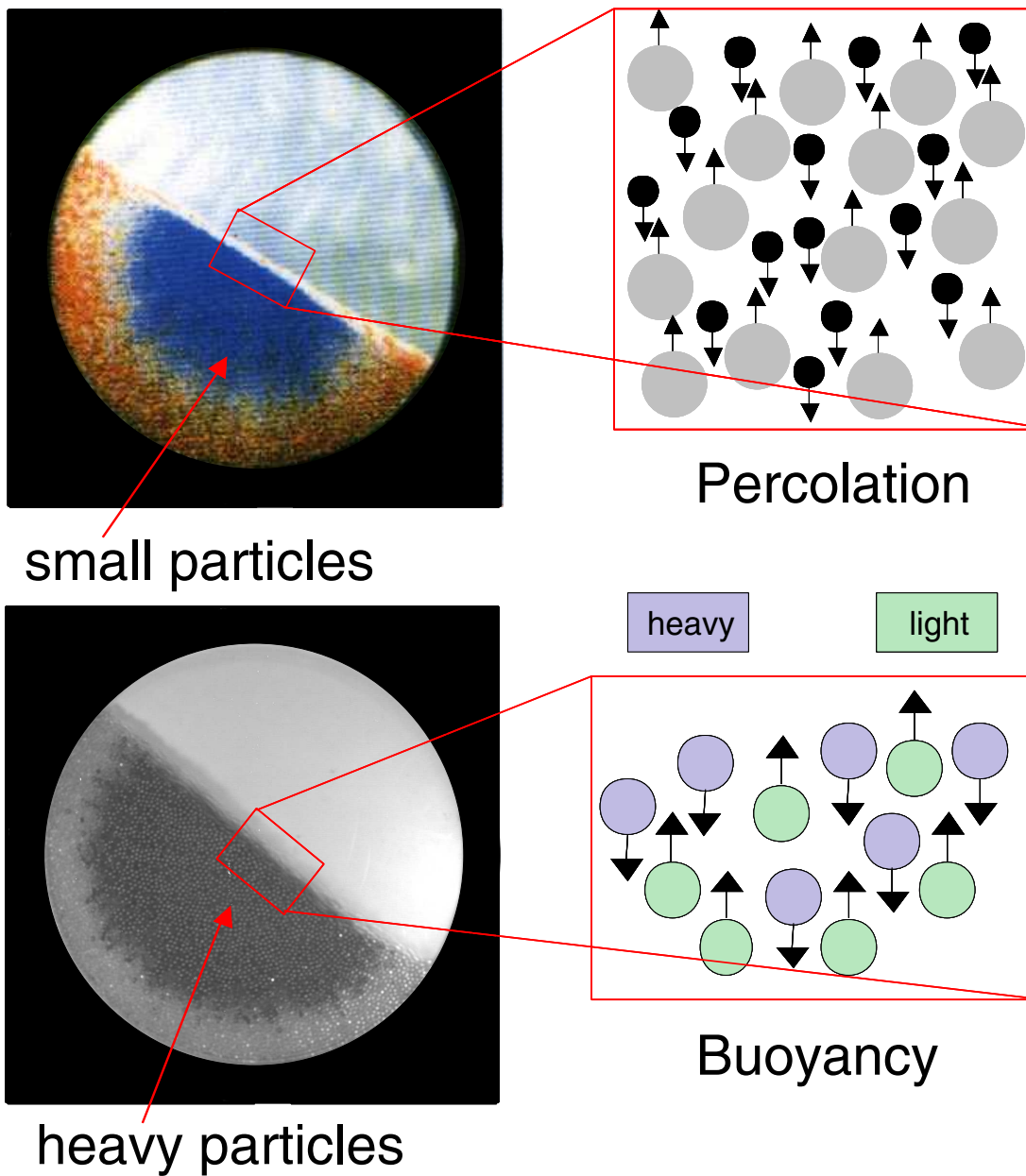


Figure 1.4. Examples of segregation of particles of differing sizes (S-systems) and densities (D-systems) in circular tumblers rotated within the continuous flow regime. Images taken from Hill *et al.* (Hill *et al.*, 1999) and Jain *et al.* (Jain *et al.*, 2005a).

flowing layer; a continuum model to explain radial segregation patterns was developed by Khakhar *et al.* (2001). Other mechanisms may arise beyond percolation, Thomas (2000) experimentally found that the mass effect from the large size ratio of particles of same density may dominate over the percolation effect: at size ratios greater than 5, a reverse segregation occurs with larger particles sinking into the core, while smaller ones lie at the periphery of the tumbler. Another effect arising in S-systems was considered by Khakhar *et al.* (2001): instead of the standard radial core pattern, they found that a radial streak pattern occurs when particles with large size ratios are rotated in an approximately half-filled tumbler at a very small rotation speed (but still in the continuous flow regime). Hill *et al.* (2005) found that the radial streak patterns depend greatly on the fill fraction of granular materials in the tumbler, and Meier *et al.* (2008) recently observed the coarsening of streaks for long runs of more than  $O(100)$  tumbler rotations, if the fill fraction is just above half full.

The second type of segregation in rotating tumblers is axial segregation. Axial segregation was first observed by Oyama (1939), but the understanding of the onset mechanisms of the axial segregation is much less advanced than radial segregation since it is nearly impossible to follow and visualize the individual particle motion during the whole course of axial segregation development, unlike radial segregation in quasi-2D tumblers. Most researchers have only investigated this phenomenon qualitatively.

In a typical segregation experiment, one starts with a well-mixed initial state of small and large particles. As shown in figure 1.5, most direct observations focus on the composition of the visible surface layer (Zik *et al.*, 1994; Fiedor & Ottino, 2003; Hill & Kakalios, 1994, 1995). As seen from the outside, segregation may appear to be complete in that



Figure 1.5. Example of axial segregation of particles of differing sizes in a long cylindrical tumbler rotated around its horizontal axis. Image is from Fiedor's experimental work (Fiedor, 2006). Black particles are small and clear particles are large.

each band contains a single particle species, with narrow transition regions separating the bands; the segregation may also be partial, in the sense that the bands may be composed of a higher concentration of one species or the other. More elaborate studies have examined the interior using magnetic resonance imaging (MRI) techniques (Hill *et al.*, 1997*b,a*), as shown in figure 1.6: beneath the surface, radial segregation on the transverse cross sections still exists along the whole length of the tumbler regardless of whether axial segregation occurs or not; the axial segregation patterns visible at the outer surface are in fact from the exposure of the radial segregation core of one species whose shape undulates along the axis to the outer surface. It appears that in all cases axial segregation is preceded by radial segregation. This order of events seems to be necessary for axial banding to occur, suggesting a close relationship between radial and axial segregation.

For long runs, complex time-dependent axial segregation band patterns occur. Nakagawa (1994) first considered the long-term evolution of axial segregation. Prior to that, experiments were run for shorter periods of time than it would take to reach equilibrium. Nakagawa ran experiments for many days and found that the final steady state achieved as

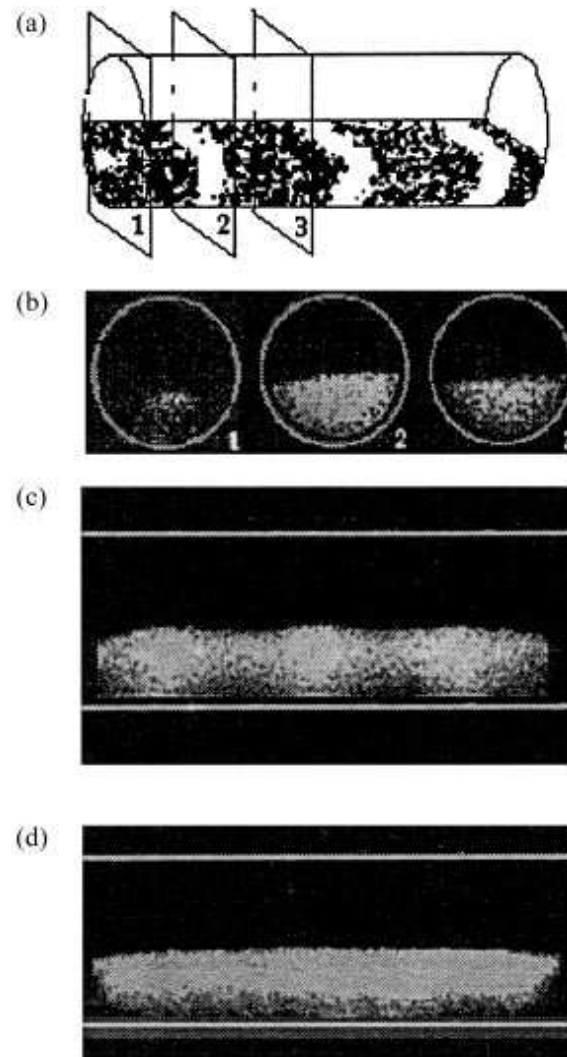


Figure 1.6. MRI data for a mixture of small and large particles rotated in a 24 cm long cylinder. (a) Schematic illustration of the axial segregation state as viewed from outside; (b) Radial segregation pattern on the cross planes taken at the locations shown in (a); (c) Image of the core of radial segregation of small particles along the plane parallel to the axis of the cylinder; (d) Image along the same plane after the cylinder was rotated at 4 rpm for approximately 45 min indicating that the radial segregation remained even though the axial bands had disappeared. From Hill *et al.* (1997b).

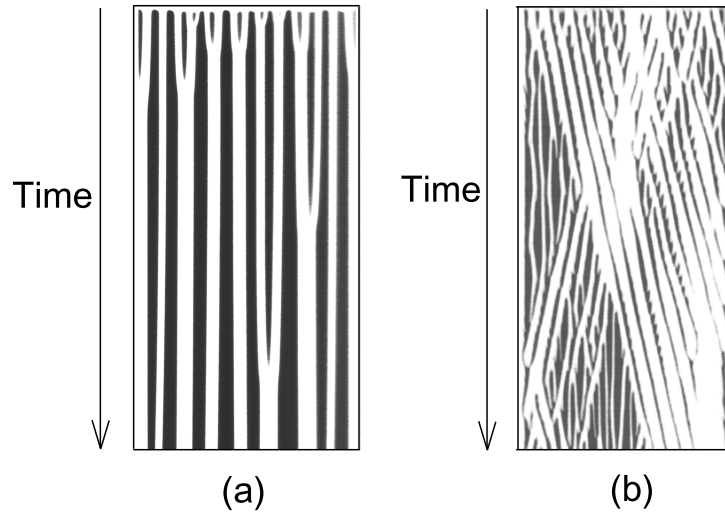


Figure 1.7. The space-time images of band dynamics of axial segregation experiments from Fiedor & Ottino (2003). Images taken by the camera at each rotation are cropped to the length of the tumbler and a height of one pixel. The cropped images are then stacked on top of each other to create a spatiotemporal series. The mixture of  $300\mu\text{m}$  black glass beads and  $900\mu\text{m}$  clear glass beads are half filled in a  $6.35\text{ cm}$  diameter,  $76\text{ cm}$  long cylindrical tumbler. (a) Band coarsening in a LGS system with water as interstitial fluid,  $\omega=3\text{ rpm}$ ; (b) Traveling waves in a DGS system with air as interstitial fluid,  $\omega=25\text{ rpm}$ .

few as three bands. As shown in figure 1.7, there are mainly two modes of time-dependent band dynamics of axial segregation:

- Band coarsening: narrower bands merge to form wider bands (Frette & Stavans, 1997). Later Fiedor & Ottino (2003) found that during coarsening the total number of bands in the system follows a logarithmic decay for both DGS and LGS systems although they have different decay rates;
- Traveling wave patterns associated with band motion (Choo *et al.*, 1997, 1998; Fiedor & Ottino, 2003).

Although the long-term dynamics of axial segregation has been intensively investigated in recent decades, the fundamental mechanisms giving rise to axial segregation are still unresolved. The focus of this thesis is to shed light on this process.

### 1.3. Thesis Outline

The thesis chapters are arranged in the following manner:

- Chapter 2 introduces the numerical method used throughout the thesis;
- Chapter 3 compares the subsurface flow of mono-disperse granular systems in the cylindrical tumblers with different lengths to understand the differences in the flow field caused by the tumbler length;
- Chapter 4 investigates the onset mechanisms of axial segregation in long cylindrical tumblers;
- Chapter 5 considers the axial segregation in spherical tumblers to investigate the effect of a change in the endwall shape on the axial segregation patterns;
- Chapter 6 gives possible extensions of current work to improve our fundamental understanding of granular physics.

Chapters 3-5 are presented as independent units and can stand on their own. Each chapter has an abstract, an introduction, a report of results, and a conclusion.

## CHAPTER 2

### Methodology

This chapter reviews simulation techniques that are used to model the dynamics of granular systems. Attention is given to the discrete element method (DEM) and its implementation in simulations. Since the time-consuming calculation of memory-related term is needed in DEM simulations, the binary-tree data structure used in the simulation to sort a data set stored in a random order, which is the case in DEM simulations, is briefly introduced.

#### 2.1. Numerical Methods often Used in Granular Physics

Models often used in granular physics can be divided into three classes: agent-based, continuum, and discrete element method (DEM). None of these models is suitable in all circumstances. Figure 2.1 shows a schematic comparison in term of the realism and their ability to explore the parameter space.

##### 2.1.1. Agent-based Models

Agent-based models can include a large number of particles, and the simulation time is short, but particle motion is not based on physical equations, but rather a set of local rules generally not based on first principles. Two such models are often used in granular physics: the Monte Carlo Method and the Cellular Automata Model.

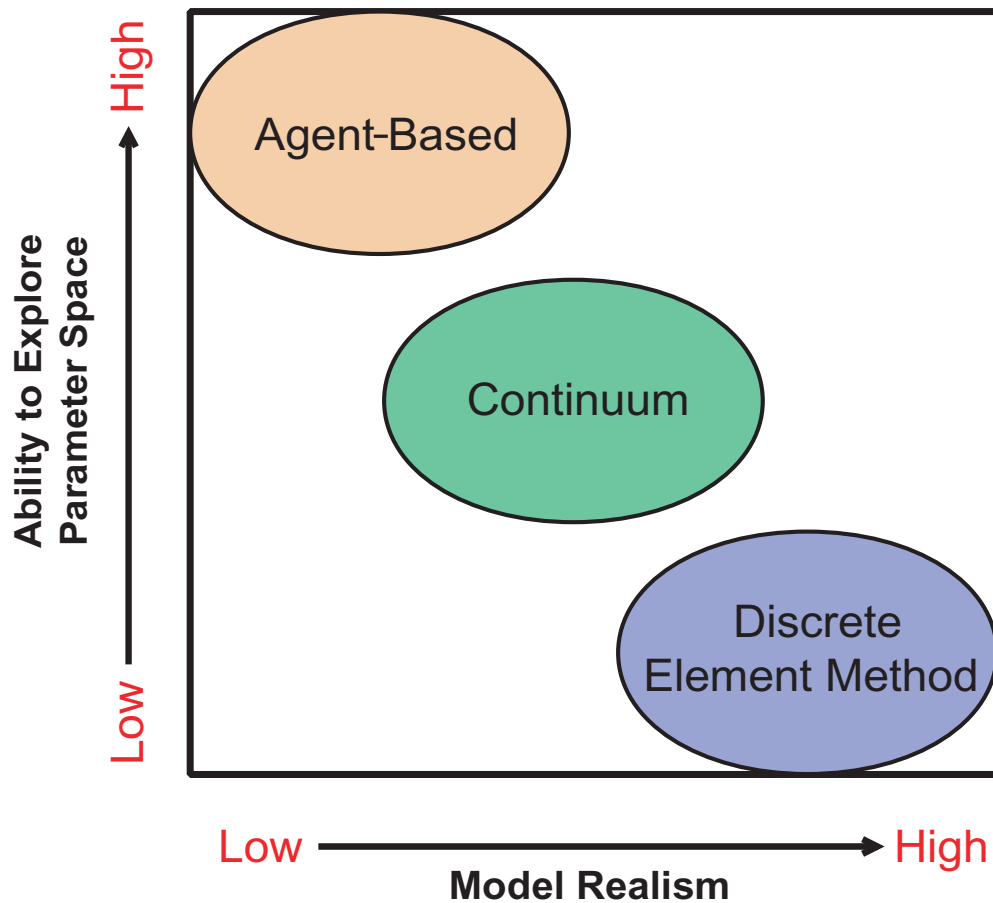


Figure 2.1. Comparison of degree of realism of physical description and ability to explore parameter space of the computational models.

The Monte Carlo method was introduced for granular materials about two decades ago to simulate the size segregation of binary granular mixtures undergoing vertical vibrations (Rosato *et al.*, 1986, 1987). The idea of the method is to find new granular particle positions by considering a rule to minimize the potential energy of the whole system. This method successfully captured the geometrical effects of the process and has been used to test a segregation model in ternary systems that describes the relaxation process

of the surface angle in vertically vibrated granular systems (Duke *et al.*, 1990). However, as pointed out by Ristow (2000), the Monte Carlo Method has several limitations that hinder its wide application in the field of granular physics: there is no physical time scale and the normal restitution coefficient has to be zero. Therefore, it is difficult to assign physical material properties to computations using this method.

The concept of a *Cellular Automata* was first introduced by von Neumann and Ulam and they used it to study biological self-reproduction (Wolfram, 1983). The use of Cellular Automata to study granular materials can be tracked to the introduction of the concept of *self-organized criticality* to study the avalanche of a sandpile (Bak *et al.*, 1987). In this model, the space is discretized into cells which can either be occupied by a particle or not. The particle motion is modeled under a set of collision rules that apply when certain conditions are met, *e.g.* the local angle of repose exceeds a certain threshold. This model has been used to study the outflow of particles in two-dimensional hoppers: the outflow rate (Baxter & Behringer, 1990), stagnation zones (Baxter & Behringer, 1991), and segregation processes (Fitt & Wilmott, 1992). Yanagita (1999) produced axial segregation of two kinds of particles that differed only in their frictional properties in rotating tumblers. Cisar *et al.* (2006, 2007) investigated radial segregation, stable lobed patterns, and chaotic mixing in various quasi-two-dimensional, regular polygonal tumblers using Cellular Automata. However, since the surface angle defined in Cellular Automata is given by the topology of the lattice, only identical particles can be studied by this method, which greatly limits the application of this method in granular physics. Moreover, similar to Monte Carlo Model, there is no direct connection between the update time and physical time in Cellular Automata.

### 2.1.2. Continuum Model

The two models described above are Lagrangian approaches, that is they follow individual particles. On the other hand, granular flow has been widely investigated also as a continuum from an Eulerian viewpoint.

Inspired by the governing equations in fluid mechanics, Haff (1983), Jenkins & Savage (1983), Lun *et al.* (1984), and Johnson & Jackson (1987) developed conservation equations for mass, momentum, and energy (accounting for dissipation) of granular materials in which the kinetic theory of granular materials (solving the *Boltzmann* collisional equation of granular particles in the analogy with ideal gases) are used to obtain the stress tensors for the constitutive closure relations. The results from these models are in good agreement with experimental results for dilute planar Couette shear flows, but, as pointed out by Savage (1982), the application of models is challenging in dense granular flows where the assumption of binary collisions does not hold.

It is far from straightforward to apply the continuum models to more complex flows, such as the flow in the thin flowing layer of rotating tumblers. A continuum model particularly designed for the granular flow in rotating tumblers was proposed by Khakhar *et al.* (1997) based on a kinematic description of the flow in the flowing layer. Unlike fluid mechanics, where the length scales of the flows are much larger than the molecular dimensions as well as the mean free paths, the continuum description of granular materials has intrinsic shortcomings since the influence from microscopic structure of granular materials (imperfectly understood currently) on the macroscopic flows cannot be neglected.

### 2.1.3. Discrete Element Method (DEM)

The discrete element method, which is based on the methodology of molecular dynamics for the study of liquids and gases (Allen & Tildesley, 2000) to model the collisions of a large number of individual particles, is undoubtedly more realistic than the methods introduced above. It is, however, more computationally intensive, although remarkable reduction in computational times can be achieved by utilizing geometrical insights for particular cases (McCarthy & Ottino, 1998). In the discrete element method, the bulk flow of the granular material is determined through explicit calculation of the trajectories of each particle (usually modeled as spheres) at every time step.

Depending on the density of granular materials and character of the flow to be modeled, two different methods of calculating the trajectories are used: a rigid-particle model or event-driven model for low density, rapid flow and a soft-particle model for high density, slow flow. In the rigid-particle model, the contact time is zero and only binary collisions occur, so the dynamics of the system is controlled by a sequence of discrete events. The velocities of the involved particles are altered by the collisions according to a collision law which is characterized by coefficients of restitution. During the time intervals between collisions, the particles move along known ballistic trajectories. Therefore, the positions of the particles at the time of the next collision can be computed in one step. The assumption of instantaneous collisions used in the rigid-particle model does not hold for high density flows, since in such cases the collision time is critical to the dynamics of the flow. Therefore, the soft-particle method is used for this work.

The earliest application of the soft-particle discrete element method (or discrete element method, for short) in granular materials can be traced back to Cundall & Stack

(1979). Since then, this method has been applied to model a large variety of granular flows: rotating tumblers (Dury & Ristow, 1997, 1999*a*), fluidized beds (Gallas *et al.*, 1992), hopper flow (Ristow & Herrmann, 1994), pipe flow (Tsuji *et al.*, 1992), silo filling (Cleary, 2000), and tumbling blenders (Moakher *et al.*, 2000). In 1986, this method was first used to study the segregation of the granular materials (Haff & Werner, 1986). Ristow (1994) first published simulations of radial density segregation and then radial size segregation (Dury & Ristow, 1997, 1999*b*; Rapaport, 2002; Li & McCarthy, 2005) in rotating tumblers.

Similar to molecular dynamics (Allen & Tildesley, 2000), the discrete element method uses an explicit, constant time step to integrate Newton’s second law to describe the translational and rotational motion of individual “soft” particles. The main difference between DEM and conventional molecular dynamics is that the particles in molecular dynamics are represented by mass points while they have finite volumes in DEM. So besides calculating the normal force between contacting particles as in molecular dynamics, we also need to consider the tangential force on the contact surface from the oblique collisions between particles and then the rotation of particles from the tangential force. Starting from Newton’s second law of motion (translational and angular), for a particle  $i$  with radius  $r_i$  and mass  $m_i$

$$(2.1) \quad m_i \frac{d\mathbf{v}_i}{dt} = \sum_j (\mathbf{F}_{ij}^n + \mathbf{F}_{ij}^s) + m_i \mathbf{g}$$

$$(2.2) \quad I_i \frac{d\omega_i}{dt} = \sum_j (\mathbf{r}_i \times \mathbf{F}_{ij}^s)$$

where  $\mathbf{v}_i$ ,  $\omega_i$ , and  $I_i$  are the translational velocity, angular velocity, and moment of inertia of the particle  $i$ , respectively. The total force on each particle consists of the external force, gravity, as well as contact forces from all contacting particles, which have normal ( $\mathbf{F}_{ij}^n$ ) or tangent ( $\mathbf{F}_{ij}^s$ ) components with respect to the surface of contact. In each discrete time step, the forces and torques on each particle are summed, and the net results are used to obtain the new velocity and position of the particle.

The accuracy of the discrete element method is almost wholly determined by the force models. These forces can be grouped into two categories: external forces and contact forces. Most DEM simulations include gravity as the only external force, except for few cases where interstitial fluid forces (Tsuji *et al.*, 1992; Li & McCarthy, 2005) or Van der Waals forces (Yen & Chaki, 1992; Severson *et al.*, 2007) are also included. The problem of two contacting bodies under general conditions is complicated (Johnson, 1989), and it has been the focus of research for more than one hundred years (Hertz, 1882). Thus, many more or less strongly simplified force schemes have been suggested and employed in DEM simulations (Schafer *et al.*, 1996; Ristow, 2000). The collision between two particles is sketched in figure 2.2, and the most common contact force models are reviewed in detail below.

**2.1.3.1. Normal Forces.** Two types of forces are commonly used in DEM to model the collisional dynamics in the normal direction during collisions: an elastic restoration

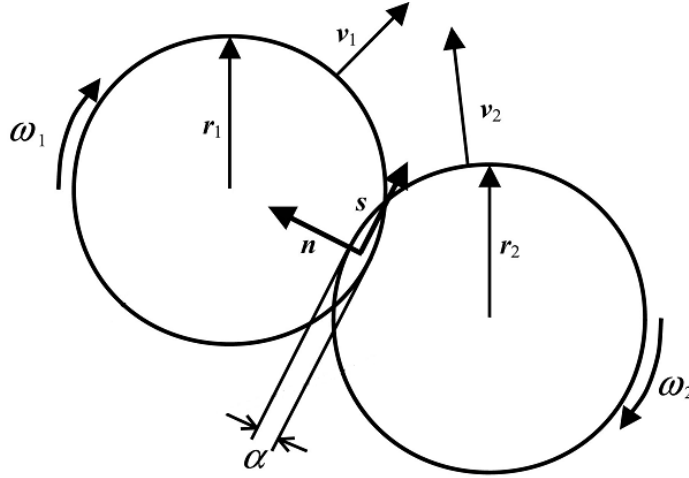


Figure 2.2. Illustration of the collision between two particles.

force,  $\mathbf{F}_e^n$ , modeled as a spring, and a damping force accounting for energy dissipation,  $\mathbf{F}_d^n$ , modeled as a dashpot. The normal force is represented as

$$(2.3) \quad \mathbf{F}_{ij}^n = \mathbf{F}_e^n + \mathbf{F}_d^n$$

Experimental measurements of force-displacement indicate an almost linear loading as a function of approach during the collisions (Mullier *et al.*, 1991; Drake & Walton, 1995; Goldsmith, 2001). So a linear spring has been used to model the elastic restoration normal force in numerous numerical simulations (Cundall & Stack, 1979; Dury & Ristow, 1997; Ristow, 2000; Schafer *et al.*, 1996), thus

$$(2.4) \quad \mathbf{F}_e^n = k_n \alpha \hat{\mathbf{x}}_{ij}$$

where  $k_n$  denotes the spring constant and  $\alpha$  is the overlap of the two particles during contact (see figure 2.2).  $\hat{\mathbf{r}}_{ij} = \hat{n}$  represents the unit normal vector (center to center) in the direction from particles  $j$  to  $i$ .

Possible mechanisms for dissipation (transformation of kinetic energy into other forms of energy and then into heat) during a collision arise from a combination of three components depending on the normal impact velocity: plastic deformation, viscoelasticity of the material, and the elastic waves or vibration from the impact. The dissipation from vibration is often neglected. For very soft materials or high impact velocity collisions, plastic deformation dominates the dissipation. But for most hard granular materials and flow regimes, viscoelasticity accounts for most dissipation. The simplest, and most used viscoelastic dissipation force is a linear relation of the form

$$(2.5) \quad \mathbf{F}_d^n = -2\gamma_n m_{eff} \dot{\alpha} \hat{\mathbf{r}}_{ij} = -2\gamma_n m_{eff} (\mathbf{V}_{ij} \cdot \hat{\mathbf{r}}_{ij}) \hat{\mathbf{r}}_{ij}$$

where  $\mathbf{V}_{ij}$  denotes the relative velocity ( $\mathbf{V}_i - \mathbf{V}_j$ ) of two contacting particles  $i$  and  $j$  and  $m_{eff} = m_i m_j / (m_i + m_j)$  is the reduced mass of these two particles.  $\gamma_n$  is a phenomenological friction coefficient characterizing the damping of granular materials.

As suggested by (Ristow, 2000; Duran, 2000), the equation of relative motion in this case reads

$$(2.6) \quad \ddot{\alpha} + 2\gamma_n \dot{\alpha} + f_0^2 \alpha = 0$$

with  $f_0 = \sqrt{k_n/m_{eff}}$  or  $k_n = f_0^2 m_{eff}$ . The characteristic equation, using  $\alpha(t) \sim e^{\lambda t}$ , is

$$(2.7) \quad \lambda^2 + 2\gamma_n\lambda + f_0^2 = 0.$$

Considering an initial conditions such that  $\alpha(0) = 0$  and  $\dot{\alpha}(0) = \mathbf{v}_0$ , where  $\mathbf{v}_0$  is the relative velocity just before the collision, a solution is

$$(2.8) \quad \alpha(t) = \frac{\mathbf{v}_0}{f} \exp(-\gamma_n t) \sin(ft)$$

with  $f = \sqrt{f_0^2 - \gamma_n^2}$ , which is the frequency of the damped oscillation. Then the collision time  $\Delta t$  given by half the period for the sine function in equation 2.8 with the condition of  $\alpha(\Delta t) = 0$  is

$$(2.9) \quad \Delta t = \pi/f.$$

Thus,  $k_n$  is related to the collision time  $\Delta t$  and the friction coefficient  $\gamma_n$  as:

$$(2.10) \quad k_n = f_0^2 m_{eff} = (f^2 + \gamma_n^2) m_{eff} = \left[ \left( \frac{\pi}{\Delta t} \right)^2 + \gamma_n^2 \right] m_{eff}.$$

The restitution coefficient in the normal direction,  $e_n$ , is defined as the ratio of velocities before and after the collision:

$$(2.11) \quad e_n = -\frac{\dot{\alpha}(\Delta t)}{\dot{\alpha}(0)} = \exp\left(-\frac{\pi\gamma_n}{f}\right).$$

Therefore,  $\gamma_n$  is related to the collision time  $\Delta t$  and restitution coefficient  $e_n$  by

$$(2.12) \quad \gamma_n = -\frac{\ln e_n}{\Delta t}.$$

A more refined model considering the non-linear relationship for the elastic restoration force was given by Hertz (1882) and Johnson (1989) as a function of the deformation  $\alpha$  and the material properties  $Y$  (Young modulus) and  $\nu$  (Poisson ratio), so that

$$(2.13) \quad \mathbf{F}_e^n = \frac{2Y\sqrt{r_{eff}}}{3(1-\nu^2)}\alpha^{3/2}$$

where  $r_{eff} = r_i r_j / (r_i + r_j)$  is the effective radius of the colliding particles.

As mentioned by Ristow (2000), the Hertz approach can be extended to viscoelastic materials to derive the non-linear damping law (Hertzsch *et al.*, 1995)

$$(2.14) \quad \mathbf{F}_d^n = -\gamma_n^n \sqrt{\alpha} \dot{\alpha}$$

where  $\gamma_n^n$  is the damping coefficient for this non-linear force model.

**2.1.3.2. Tangential Forces.** Generally, the tangential force, or shear force, is related to the normal force by the Coulomb law of friction. That is,  $\mathbf{F}_s \leq \mu_s \mathbf{F}_n$  for static friction and  $\mathbf{F}_s = \mu_d \mathbf{F}_n$  for macroscopic slip friction, where  $\mu_s$  and  $\mu_d$  are the static and dynamic friction coefficients, respectively. But the relation between the tangential force and displacement for two particles in contact has proven more complicated. Mindlin (1949) found that in the outer regions of the contact area, where the normal stresses

are small since the strains are small, dynamic friction is expected, whereas in the inner regions, where large normal strains and stresses are present, static friction may occur. So there is an *annulus of microslip* surrounding an inner region of sticking in the contact area. Because the friction laws are strongly nonlinear, the size and form of the annulus of microslip depend on the loading-unloading history of the contact, making the prediction of tangential deformation and friction forces complicated.

The simplest form of a tangential force model neglects microslip. Viscous friction is used, and no history dependence is retained. If the viscous force is larger than the Coulomb frictional force, the contact “breaks” and the force is sliding friction based on Coulomb’s law

$$(2.15) \quad \mathbf{F}_{ij}^s = -\min(|\gamma_s \mathbf{v}_{ij}^s|, |\mu \mathbf{F}_{ij}^n|) \text{sign}(\mathbf{v}_s)$$

where  $\gamma_s$  is an empirical proportionality constant analogous to  $\gamma_n$ , but with no clear theoretical basis.  $\mathbf{v}_{ij}^s$  is the relative tangential velocity of two particles

$$(2.16) \quad \mathbf{v}_{ij}^s = \mathbf{v}_{ij} - (\mathbf{v}_{ij} \cdot \hat{\mathbf{r}}_{ij}) \hat{\mathbf{r}}_{ij} - \frac{\mathbf{r}_i \omega_i + \mathbf{r}_j \omega_j}{r_i + r_j} \times \hat{\mathbf{r}}_{ij}.$$

This approach is used in numerous DEM simulations (Buchholtz & Pöschel, 1994; Pöschel, 1993; Ristow *et al.*, 1994; Rapaport, 2002) since it has the advantage of computational simplicity. But this model cannot be used in static or quasi-static systems since in such cases the stability would require the existence of finite shear forces acting between particles to withstand gravitational force components in the shear direction of the contacts.

A more realistic tangential force model that records the history of tangential displacement and thus the tangential elasticity of collision was introduced by Cundall & Stack (1979). This model agrees well with experiments for the simulation of static behavior. The friction force in the tangential direction is modeled by a spring with stiffness,  $k_s$ , which exists until the particle surfaces separate from each other

$$(2.17) \quad \mathbf{F}_{ij}^s = -\min(|k_s \boldsymbol{\beta}|, |\mu \mathbf{F}_{ij}^n|) \text{sign}(\boldsymbol{\beta}).$$

Here the tangential displacement  $\boldsymbol{\beta}$  is given by

$$(2.18) \quad \boldsymbol{\beta}(t) = \int_{t_0}^t \mathbf{V}_{ij}^s dt$$

where  $t_0$  is the initial contact time between two particles. The tangential stiffness,  $k_s$ , determines the half period of tangential oscillation, just like  $k_n$  determines the half period of normal oscillation,  $\Delta t$ . The value of  $k_s$  has to be determined from the comparison of the simulations with experimental results.

The choice of force models depends on the range of impact velocities expected in a given simulation. All of the force models discussed in this section yield reasonably realistic responses for the collisions. Both the linear spring-dashpot and the Hertz normal force models were tested and no significant macroscopic differences between them was found. Figure 2.3 compares the two force models in terms of the streamwise velocity profiles at the center of the flowing layer ( $x = 0m$ ) for two axial positions: at the center of the tumbler ( $z = 0m$ ) and near the endwall, in a half-full tumbler with  $L = 0.06m$  and

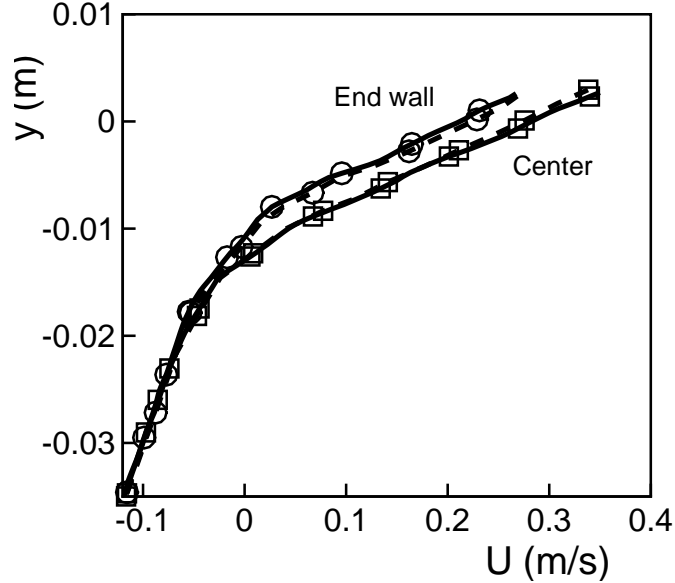


Figure 2.3. Comparison of linear spring-dashpot force model (solid curves) and Hertz force model (dashed curves) for the streamwise velocity  $u$ (m/s) at the center of the tumbler ( $\square$ ,  $z=0$ ) and near the endwall ( $\circ$ , bin adjacent to the endwall) in a half-full tumbler with  $d = 0.003m$ ,  $L = 0.06m$ , and  $D = 0.07m$ .  $\omega = 3.4\text{radians/s}$ .

$D = 0.07m$  ( $\omega = 3.4\text{radians/s}$ , mono-disperse particles with  $d = 0.003m$ ). The two models provide nearly identical results. Thus, the linear spring-dashpot normal force is used in this work since it requires less computational effort than the Hertz model, which requires a smaller time step. The memory-related tangential force model is more realistic than viscous force model, but it requires much more effort to deal with the history of the tangential displacement. Both tangential force models were tested for several cases. The macroscopic properties such as the segregation patterns from both tangential force models agree very well with each other, indicating that the choice of which one to use is rather flexible under the simulation conditions used in this work.

The velocity-Verlet algorithm (Ristow, 2000; Allen & Tildesley, 2000) is used in this work to update the positions and velocities of particles. It is applied in two stages and resembles a three-value predictor-corrector algorithm

$$\begin{aligned}
 \mathbf{x}_i(t + dt) &= \mathbf{x}_i(t) + dt\mathbf{v}_i(t) + \frac{1}{2}dt^2\dot{\mathbf{v}}_i(t) \\
 \tilde{\mathbf{v}}_i(t + dt) &= \mathbf{v}_i(t) + \frac{1}{2}dt\dot{\mathbf{v}}_i(t) \\
 \dot{\mathbf{v}}_i(t + dt) &= \dot{\mathbf{v}}_i(\mathbf{x}_i(t + dt), \tilde{\mathbf{v}}_i(t + dt)) \\
 \mathbf{v}_i(t + dt) &= \mathbf{v}_i(t) + \frac{1}{2}dt[\dot{\mathbf{v}}_i(t) + \dot{\mathbf{v}}_i(t + dt)]
 \end{aligned}
 \tag{2.19}$$

where  $\dot{\mathbf{v}}_i(t)$  denotes the acceleration of particle  $i$  at the instant  $t$  and  $\tilde{\mathbf{v}}_i(t + dt)$  is the predicted velocity of the particle at the instant  $t + dt$ . A similar algorithm is used to update the angular velocity of the particles.

Another important issue is numerical stability in DEM simulations. The general requirement is that the normal restitution coefficient,  $e_n$ , should be independent of the time step,  $dt$ . To check this requirement, Ristow (2000) conducted the numerical experiments for a particle-wall collision with different  $dt$ 's and suggested that a time step of  $1/30$  or less of the theoretical collision time,  $\Delta t$ , is required. Thus, we set  $dt = \Delta t/40$  in this thesis.

## 2.2. Implementation of DEM in the Simulations

### 2.2.1. Boundary Conditions

The interaction between particles and the outer boundary of the container can be addressed in two ways: 1) constructing wall particles on the boundaries with similar properties to the mobile particles; 2) using geometrically smooth surfaces with properties similar to the particle properties to represent the boundaries. The advantage of the first method over the second is that there is no need to check the relative positions of every particle with respect to the wall(s) every time step, since the positions of wall(s) may also change with time. Otherwise for every particle, it is necessary to determine how many and which wall edges contact it for every time step. This is very time-consuming, especially, for modeling of square, pentagon, or other shapes of containers. The cylinder end boundaries can be set to either a periodic boundary condition or a solid wall. In the case of periodic boundary conditions, any particle that leaves the simulation region immediately reenters the region through the opposite face. Particles near the boundary may interact with particles near the opposite boundary — a wrap-around effect. To simulate a solid endwall, flat geometrical surfaces are used to model the particle interaction with endwalls. This is necessary to avoid the use of a large number of wall particles to fill the entire area of the two endwalls. This increases the total number of particles in the system greatly. Thus, smooth surfaces were used for the tumbler walls.

### 2.2.2. Initial Particle Distribution

Most experiments about granular segregation are conducted from the well-mixed initial condition. Thus, an initial condition (*IC*) corresponding to a random packing of particles

(mono-disperse or bi-disperse) is needed in the numerical simulations. The *IC* is generated as follows (see figure 2.4):

- An initial random distribution of mass points are generated in a volume confined in the computational domain, for example, a rectangular box within the boundaries of the tumbler in figure 2.4 (a). Each mass point corresponds to a particle, and the particles have no volume. The number of particles is a little more than the required value, which is estimated from the required fill level of the tumbler and the volume fraction of random packing (64% for random close packing (Jaeger & Nagel, 1992)). The initial velocities and accelerations of particles are set to be zero. The tumbler is static;
- The radii of the mass points grow in every time step until they reach the specified values. To prevent regular packing, a normal distribution of particle sizes with variance of 0.1 of the specified diameter is used. If particles overlap, the normal repulsive force between the particles moves them away from one another;
- After the preset sizes of particles are achieved, the gravitational force is applied and all particles drop downward to the static wall of the tumbler;
- The particles settle down into a static pile with a hump, as shown in figure 2.4 (d);
- The particles above the required height, which is calculated from the fill level, are removed and a flat free surface remains (figure 2.4 (e));
- The tumbler starts to rotate. The time at which flow begins sets  $t = 0$ .

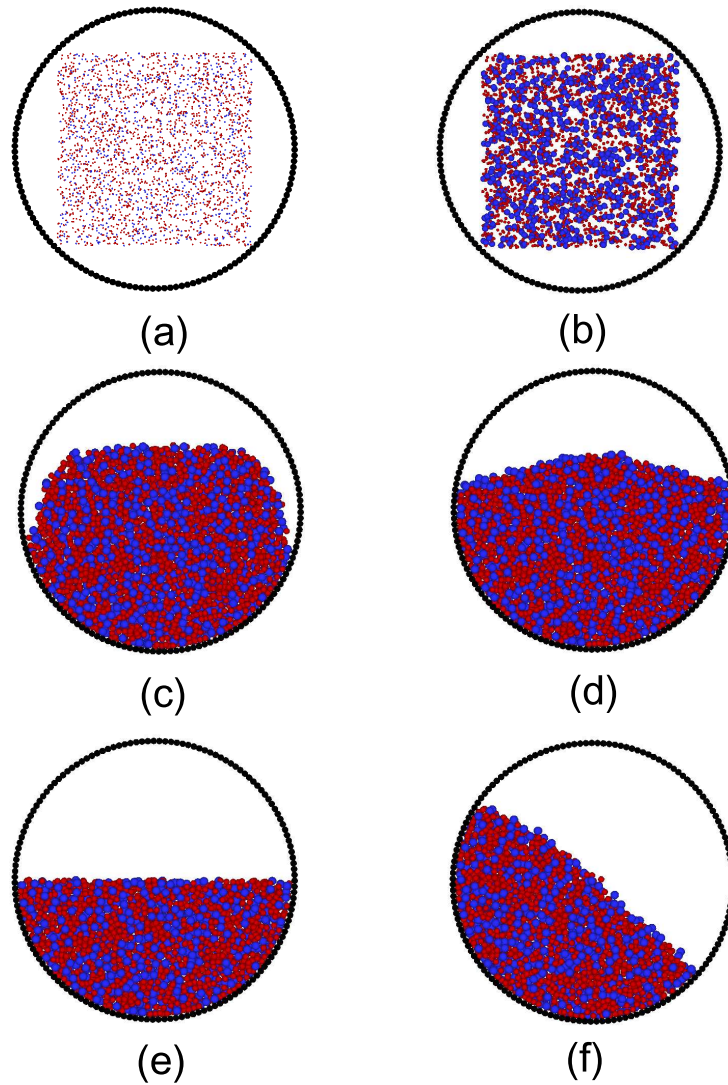


Figure 2.4. Illustration of the procedure to generate an initial random distribution of particles in a half full tumbler with two different sizes (black: wall particles; red: 3mm small particles; blue: 4mm large particles). (a) Initial random distribution of mass points; (b) Particles are growing in size; (c) Particles are dropping after the required particle sizes are reached; (d) Particles settle down with a hump; (e) Particles above the required height are removed leaving a flat free surface; (f) Particles are starting to rotate clockwise.

### 2.2.3. Data Acquisition

DEM simulations provide information at the microscopic level (particle positions, velocities, and accelerations) explicitly in every time step. This very detailed information can be converted into macroscopic terms (flow field, number density field *etc.*). To do this, the computational domain is divided into bins. All local basic properties such as velocity and number density of particles, are obtained by averaging the values for all particles within each bin (cuboid bins in this thesis). Then other properties including the velocity fluctuations and particle fluxes can be calculated from these basic properties. To get statistically meaningful results, long averaging times are sometimes necessary to minimize inherent random fluctuations.

## 2.3. Handling of Data Structure to Speed Simulations

As with molecular dynamics simulations, the computational time in a DEM simulation results from two main contributions: the calculation of pairwise forces and searching for contacts between particles. The latter can be accelerated by using methods common in molecular dynamics simulations: cell (linked) lists or neighbor lists, or their combination, which is used in this thesis due to our focus on dense systems (Allen & Tildesley, 2000; Rapaport, 2004). The discrete element method needs even more computational time to calculate the memory-related tangential force, which needs the computer dynamic memory to record and sort the contact list of the last time step. Since the contact list of each particle changes with every time step, it is necessary to be able to tell if every contact associated with this particle is a new contact or not: if it is a new one, we only need to calculate equation 2.18 from zero initial displacement directly, that is  $\boldsymbol{\beta}(t) = \mathbf{v}_s(t)\delta t$ ;

otherwise, we need to retrieve the tangential displacement from the contact list of last time step and then update the displacement as  $\beta(t) = \beta(t - \delta t) + \mathbf{v}_s(t)\delta t$ . Sometimes, the time used to check new contacts in the system and retrieve the data from old contacts is almost the same order as the time for the force calculation, especially for bi-disperse granular systems where the large size ratio of large to small particles may generate a long contact list for the large particles. Therefore, an efficient sorting algorithm is quite useful in the DEM simulation.

In common data structures, the database is sorted by a method called an “insertion sort” (Chapman, 2003). It works by placing the number of each particle contacting with the specified particle in its proper position in the list as it is read in, almost randomly in DEM simulation. As shown in figure 2.5(a), if the value of the particle number is smaller than any previous value in the list, then it is placed at the top; if the value is larger than any previous value in the list, then it is placed at the bottom; if the value is in between, then the number is inserted at the appropriate place in the middle of the list. So for the contact list of last time step shown in figure 2.5(a), there are a total of 11 particles contacting the No.50 particle. If a contact is read in, depending on where this particle number appears in the contact list of last time step, it is necessary to compare  $5\frac{1}{2}$  numbers on average before determining if it is a new contact or not and then retrieve the data associated with the desired contact if it is an old one.

In contrast, we introduce a binary tree structure (Chapman, 2003) to sort the contact list in our work. As shown in figure 2.5(b), when the new contacting particle number is read, it is compared to the No.50 particle, which is called the root number. If this new number is less than the root number, then we set it to the left side of the root number.

If the new number is greater than the root number, then it is set to the right side of the root number. If the new contacting number is greater than the root number but the right position of the root number is already occupied, then we compare the new number to this number occupying the right position, and insert the new number to the proper position below this number. This procedure is repeated as new contacts are added, producing an inverted tree structure, with the numbers in order. Therefore, if the contact list of the last time step of a specified particle is arranged in a binary tree structure as shown in figure 2.5(b), no more than four checks are required to locate any particular number. So the binary tree is a much more efficient way to search for and retrieve data than the common insertion sort structure. This advantage increases rapidly as the size of the database (contact list here) to be searched increases. Therefore, the binary tree structure is more suitable for a DEM simulation since the order of the contact list is read in the database randomly.

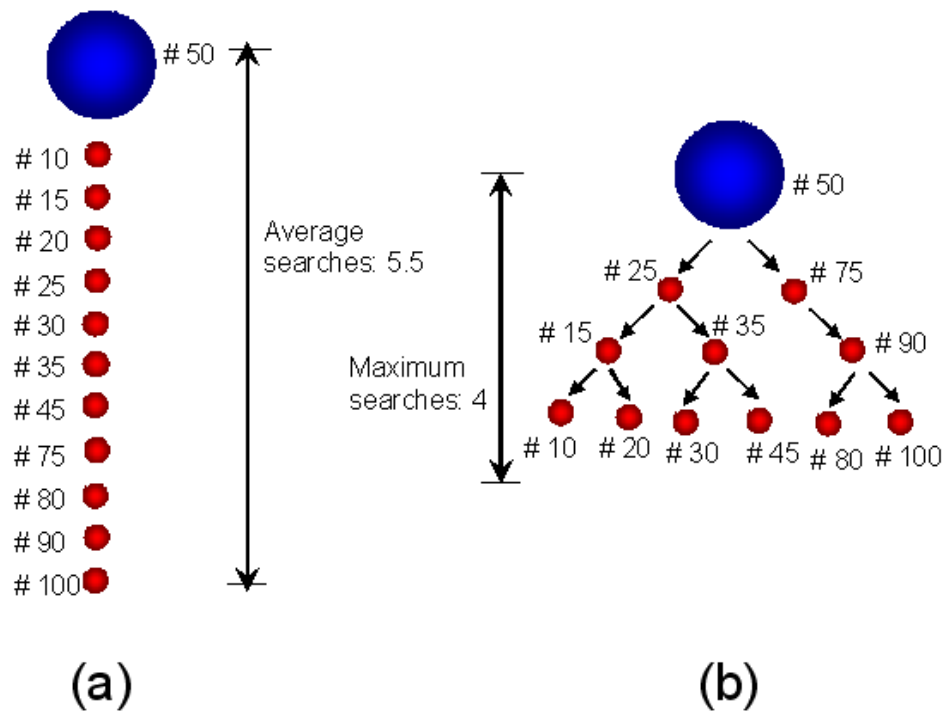


Figure 2.5. Comparison of the efficiency of two data structures to store the contact list of No.50 particle in DEM simulation: (a) insertion sort structure; (b) binary tree structure.

## CHAPTER 3

## Subsurface Granular Flow in Rotating Tumblers: A Detailed Computational Study

**Chapter Summary:** A prerequisite to understanding axial segregation of bi-disperse mixtures in long tumblers is the analysis of the flow field in mono-disperse systems, especially the subsurface flow. This is difficult to achieve experimentally due to the opacity of granular materials. Often granular flow is studied in quasi-2D rotating tumblers through transparent endwalls with the assumption that it represents the flow in a “slice” of long tumblers. But it is impossible to understand the role of axial flow in the system from quasi-2D experiments. Thus, a complete, detailed study of the flow field in long tumblers is necessary.

Information about the flow field in long tumblers is sparse and what little information available is focused on the visible surface flow. In this chapter, simulations of the flow, particularly the subsurface flow for mono-disperse granular systems in half-full cylindrical tumblers with different tumbler lengths, are used to study the flow field. Many important aspects of the flow field, such as the flowing layer structure, the streamwise velocity, velocity fluctuations, and axial flow near endwalls, depend on the tumbler length. By computationally omitting the friction at the endwalls, we confirm that these differences related to the tumbler length are a result of the frictional endwalls and the interaction of the effect between the two endwalls. When the tumbler is longer than one tumbler

diameter, the flow field caused by endwalls is localized and independent of the length of the tumbler. Consistent with prior measurements at the surface, a region of high speed flow with axial components of velocity occurs near each endwall in long tumblers. The high speed region with the associated axial flow near frictional endwalls persists through the depth of the flowing layer, though the regions of high velocity shift in position and the velocity is lower compared to the surface. In quasi-2D tumblers, the high speed regions near the endwalls merge resulting in a higher velocity than occurs in a long tumbler, but with a flowing layer that is not as deep. Velocity fluctuations are altered near the endwalls. Particle velocity fluctuations are greatest just below the surface and diminish through the depth of the flowing layer. [This work has appeared in a slightly different form in Physical Review E, *Vol.* 78, 021301, 2008.]

### 3.1. Introduction

The horizontal cylindrical rotating tumbler is a canonical system often used to study the thin flowing surface layer typical of flowing granular materials. Although granular flow has been much studied in recent years (MiDi, 2004; Ottino & Khakhar, 2000; Meier *et al.*, 2007), it is quite difficult to experimentally probe the nature of the flow beneath the visible surface due to the opacity of the particles. To overcome this problem, many researchers have made measurements of the flow in quasi-two-dimensional (quasi-2D) systems (Orpe & Khakhar, 2004; Jain *et al.*, 2002; Orpe & Khakhar, 2007; Clement *et al.*, 1995; Cantelaube & Bideau, 1995; Cantelaube *et al.*, 1997; Ristow, 1996; Komatsu *et al.*, 2001), where the axial dimension of the system is only a few particle diameters in length.

Although using a quasi-2D tumbler with transparent endwalls allows the easy measurement of many important properties of granular flow including profiles of the velocity and particle number density through the depth of the flowing layer, recent studies have shown that the flow near the middle of the length of the long tumblers is significantly different from that near the endwalls due to friction. Not only is the streamwise velocity just adjacent to the endwall slower than that at the center of the tumbler (Maneval *et al.*, 2005), but the velocity in quasi-2D tumblers is as much as two times higher than for long tumblers (Pohlman *et al.*, 2006b). Furthermore, the streamwise velocity in a long tumbler varies along the length of the tumbler, with a higher velocity in a region near the endwalls than at the center of the tumbler (Pohlman *et al.*, 2006a,b). Thus, it is clear that measurements of the velocity field in a quasi-2D system, while helpful in understanding certain aspects of the flow, do not exactly represent the flow in a “slice” of a long tumbler.

Moreover, the endwall boundary affects the mixing of mono-disperse particles (Santomaso *et al.*, 2004) and plays a role in initializing axial segregation bands of bi-disperse particles (Bridgwater *et al.*, 1969; Hill & Kakalios, 1994; Fiedor, 2006) near the endwall regions. Santomaso *et al.* (2004) suggested that there exists an axial flow near the endwalls of rotating tumblers causing the axial mass transport between transverse slices in that region. This axial flow has been confirmed based on measurements of the velocity on the surface of the flowing layer (Pohlman *et al.*, 2006b) and is corroborated in this study.

The opacity of the particles makes optical techniques for measuring the velocity field below the surface of a granular flow difficult. There are several experimental techniques that can be used to overcome the opacity: fibre-optic probes (Boateng & Barr, 1997) provide flow measurements at a single point, but the probe disturbs the flow locally; PEPT

(Positron Emission Particle Tracking) (Parker *et al.*, 1997) provides measurements deep in the flowing layer, but it is possible to track only one or two particles, not the entire flow field; MRI (Magnetic Resonance Imaging), which requires very expensive equipment, has been used to measure the flow field below the surface in granular systems (Nakagawa *et al.*, 1993; Fukushima, 1999; Maneval *et al.*, 2005), but its low spatial and temporal resolution makes it difficult have confidence that it can capture subtle properties of granular flow, such as the axial velocity.

Numerical simulation offers an attractive alternative to experiments that overcomes the problem of using optically-based measurement techniques in quasi- $2D$  tumblers and the difficulty of using cumbersome experimental techniques such as MRI and PEPT in long tumblers. Here we present a detailed numerical study of granular flow in rotating cylindrical tumblers using the discrete element method (DEM) (Cundall & Stack, 1979; Ristow, 2000; Schafer *et al.*, 1996). Our goal is to provide a detailed and complete examination of the entire three-dimensional flow field throughout the depth of the flowing layer in order to understand the differences between the flow in long tumblers and quasi- $2D$  tumblers. We pay particular attention to the axial flow generated from the frictional endwalls, which is helpful to understand the mechanisms of mixing and segregation near the endwall regions. Using DEM simulations not only has the advantage of allowing the examination of the flow structure beneath the free surface, it also permits the investigation of the dependence of the flow on parameters that are not easily controlled in experiments.

### 3.2. Numerical Parameters

We simulate tumblers that are half filled with granular particles and rotating at a speed such that the continuously flowing layer is nearly flat. To avoid the close-packed crystal structure, the particles have a normal size distribution with a variance of  $(0.1d)^2$ , where  $d$  is the mean size of particles (except where noted, we use  $d = 1.5mm$  in this chapter). The number of particles in the simulation was as many as 110,000, depending on the tumbler dimension and particle size. The parameters of simulations in this chapter are as follows: tumbler diameter is  $D = 2R = 0.07m$ ; the length of the tumbler is varied from  $L = 0.01m$  to  $L = 0.15m$ ; gravitational acceleration is  $g = 9.8m/s^2$ ; particle properties are for spherical vitamin-E particles (density  $\rho = 1100kg/m^3$ , restitution coefficient  $e = 0.89$  (Ristow, 2000)) to allow comparison of our simulations with MRI experiments (Maneval *et al.*, 2005) where spherical particles containing liquid cores were used. The only adjustable parameters in the model are the coefficients of friction and the collision time. To achieve the best match with MRI experiments (Maneval *et al.*, 2005), the friction coefficients among particles and between particles and walls are set to  $\mu = 0.6$ ; in order to save computer time, the collision time is  $\Delta t = 1.0 \times 10^{-4}s$ , which is realistic since the maximum overlap between particles is only a very small fraction of the sum of their radii (Dury & Ristow, 1997, 1998). The integration time step is  $dt = \Delta t/40 = 2.5 \times 10^{-6}s$  to meet the requirement of numerical stability (Ristow, 2000); the rotational speed is  $\omega = 3.4radians/s$ , consistent with the experiments (Maneval *et al.*, 2005). The curved cylindrical wall of the tumbler is modeled using wall particles with properties similar to the mobile particles to prevent the slip along the wall. Geometrically smooth surfaces are used to represent the two endwalls, which are assumed to have infinite mass and radius for

the calculation of the collision force between mobile granular particles and the endwalls. The coordinate system sets the origin at the center of the tumbler with the  $x$  axis along the streamwise direction, the  $y$  axis normal to the free surface, and the  $z$  axis along the tumbler axis, as shown in figure 1.1.

For analysis of the results, the computational domain is divided into bins (20 bins in each dimension). All local flow properties are obtained by averaging values for all particles within each bin. Although the flow is steady, inherent fluctuations necessitate a long time averaging (typically over one million timesteps) to minimize the standard deviation.

Using MRI, Maneval *et al.* (2005) recently measured the streamwise velocity profile experimentally at the midpoint of the flowing layer ( $x = 0$ ) for two axial positions: near the end wall and at the center of the tumbler. They tumbled  $3mm$  particles having a liquid core in a half-filled cylindrical tumbler ( $0.07m$  diameter and  $0.06m$  axial length, so  $L/d = 20$ ) at an angular velocity of  $3.4radians/s$ , resulting in a continuously flowing, nearly flat flowing layer. The time-averaged velocity profiles over 1.35 tumbler rotations for our particle dynamics simulation for  $3mm$  particles are plotted against corresponding experimental results in figure 3.1. The primary qualitative characteristics of the velocity profiles are captured by the DEM simulation: the magnitude of the streamwise velocity at different depths, the general nature of the velocity profiles including a nearly linear profile in the flowing layer ( $y \geq -0.01m$ ), a linear profile for the solid body rotation ( $y \leq -0.02m$ ), and the logarithmic transition between these two regions. More importantly, the differences between streamwise velocity profile at the center of the tumbler and near the endwall are well reproduced by the numerical simulation: particles near the endwall are always slower than particles at the same depth in the center of the tumbler. The

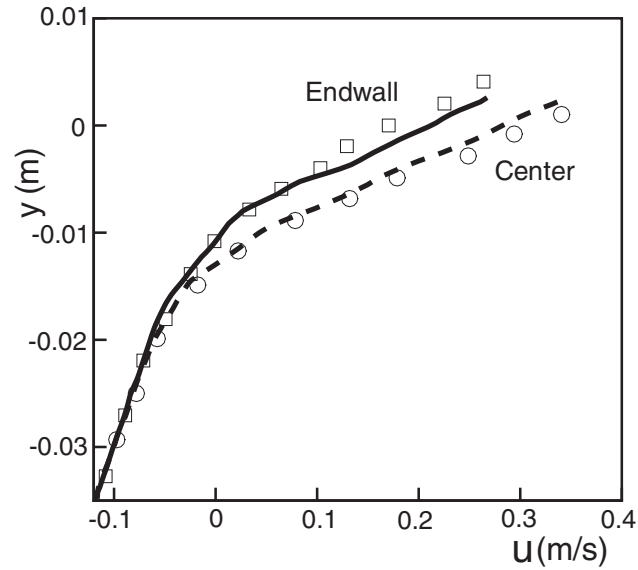


Figure 3.1. Comparison of streamwise velocity  $u$ (m/s) from DEM simulation (curves) with experimental results (data points) from Maneval *et al.* (2005) at the center of the tumbler ( $\circ$ , dashed curve,  $z=0$ ) and near the endwall ( $\square$ , solid curve, bin adjacent to the endwall).

slight differences between the measured and simulated velocity profiles likely arise from the difficulty in matching the parameters of the simulation ( $e$ ,  $\Delta t$ , and  $\mu$ ) to the values for the particles in the experiment. The value for  $e$  is fixed for vitamin-E particles (Ristow, 2000). The simulation is insensitive to the value for  $\Delta t$ . The only parameter that was adjusted to match the experiments was the frictional coefficient,  $\mu$ , and, in fact, the simulation is relatively insensitive to this as well. Another contact law, the Hertzian normal force law, was also considered, but did not significantly change the results.

Streamtraces obtained by the integration of the local average velocity vector ( $u$  and  $w$ ) for the flow on the free surface ( $y = 0$ ) for the case in figure 3.1 are shown in figure 3.2.

At the center of the tumbler ( $z = 0$ ), the streamtraces are straight indicating pure stream-wise flow. However, the curved streamtraces near the endwalls located at  $z = \pm 0.03m$  indicate that particles near the endwalls tend to move toward the center of the tumbler in the upstream part of the flowing layer and then move back toward the endwall in the downstream part. As would be expected, the velocity field is approximately symmetric about the center of the tumbler,  $z = 0$ . These results are consistent with the curved particle trajectories that have been observed in experiments (Pohlman *et al.*, 2006b). The results shown in figure 3.1 and figure 3.2 indicate that several important details of the actual flow field are captured by DEM simulations. Thus, the DEM technique used here provides an accurate representation of an actual experimental system and provides a solid foundation for the following examination of the subsurface granular flow.

The primary objective of this chapter is to explore the entire flow field in three-dimensional cylindrical tumblers, focusing on the flow beneath the visible surface. We present results for the structure of the flowing layer, streamwise velocity field, velocity fluctuation field, and axial flow field throughout the entire flowing layer. Of particular interest is the impact of the endwalls and the overall tumbler length on the subsurface flow.

### 3.3. Flowing Layer Structure Beneath the Visible Free Surface

We consider first the overall structure of the flowing layer. We define the flowing layer as the region in the tumbler where the streamwise velocity in the reference frame of the rotating tumbler is greater than 5% of the surface velocity at the center of the tumbler ( $(x, y, z) = (0, 0, 0)$ ),  $u_o$ . (This scheme is analogous to that used to define the edge of a

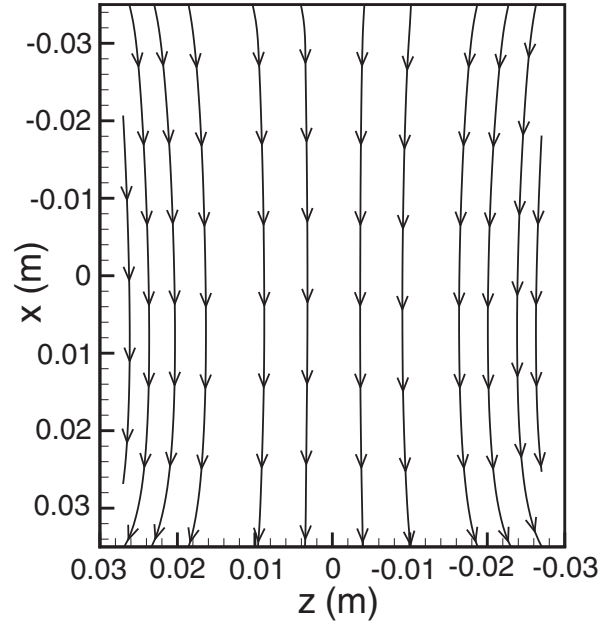


Figure 3.2. Streamtraces of the particle flow on the free surface. Flow is from top to bottom. Endwalls are located at  $z = \pm 0.03m$ . Curvature of the streamtraces near the endwalls is related to the friction at the endwalls.

boundary layer in fluid flow.) Since the numerical method provides the velocity in the laboratory frame, the solid body rotation of the tumbler is subtracted before identifying the boundary of the flowing layer. As with experiments, a region of creeping motion exists between the freely flowing material and the fixed bed of particles in solid body rotation (Komatsu *et al.*, 2001; Socie *et al.*, 2005).

First, we consider the lower boundary of the flowing layer on the  $z = 0$  and  $x = 0$  planes in figure 3.3 and figure 3.4 for three cases: a long tumbler with  $L = 0.10m$  ( $L/D = 1.43$ ), a short tumbler with  $L = 0.05m$  ( $L/D = 0.71$ ), and a quasi-2D tumbler with  $L = 0.01m$  ( $L/D = 0.14$ ). To compare them, the streamwise position ( $x$ ), depth ( $y$ ) are normalized

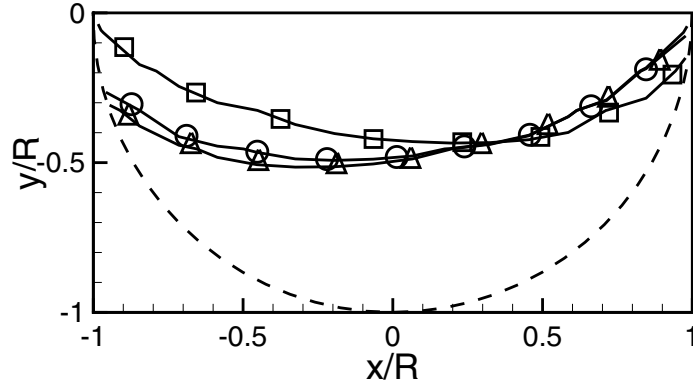


Figure 3.3. Boundaries of flowing layer for 1.5mm particles at  $z = 0m$  in three tumblers where  $y = 0$  corresponds to the surface of the flow:  $\Delta$ ,  $L = 0.10m$  ( $L/D = 1.43$ );  $\circ$ ,  $L = 0.05m$  ( $L/D = 0.71$ ); and  $\square$ ,  $L = 0.01m$  ( $L/D = 0.14$ ). Flow is from left to right. The dashed curve indicates the tumbler wall.

by the radius ( $R$ ) and axial position ( $z$ ) is normalized by the length ( $L$ ) of the tumbler. In addition, in figure 3.4 the flowing layer depth for a long tumbler where one endwall is frictionless is also shown to illustrate the influence of endwalls on the flowing layer structure. The region above each curve in figure 3.3 and figure 3.4 corresponds to the flowing layer and the region below the curve is in near-solid rotation.

From figure 3.3, it is clear that at the mid-length of the tumbler ( $z = 0$ ), the depths of flowing layer at the upstream end of the flow ( $x/R = -1$ ) as the flow is initiated in the long and short tumbler are much larger than that in the quasi-2D tumbler, which means in these two longer tumblers more particles participate the initialization of the inclined flow. More than this, the flowing layers of these three tumblers are not symmetric about the mid-length of the flowing layer ( $x = 0$ ): the flowing layers in long and short tumblers are skewed to the upstream portion, while the flowing layer of quasi-2D case is skewed to the downstream portion. Clearly, this skewness is related to the geometry of the tumbler.

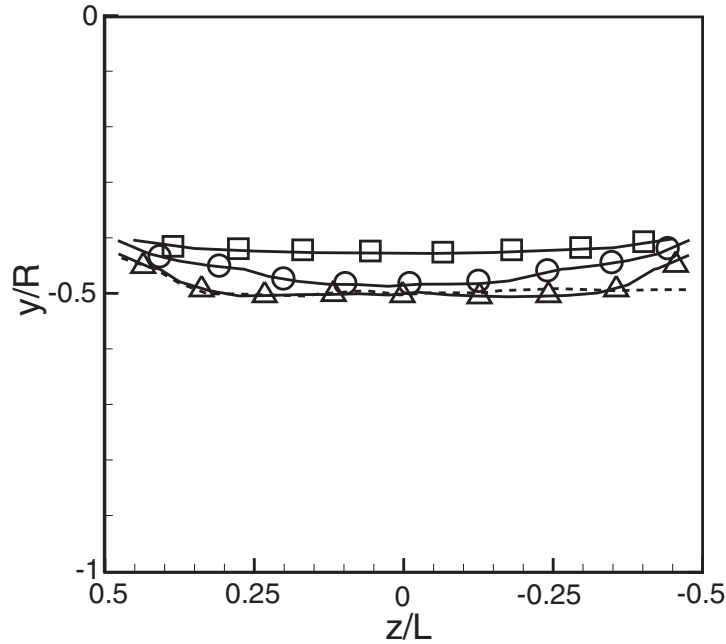


Figure 3.4. Boundaries of flowing layer for 1.5mm particles at  $x = 0m$  in three tumblers:  $\Delta$ ,  $L = 0.10m$  ( $L/D = 1.43$ );  $\circ$ ,  $L = 0.05m$  ( $L/D = 0.71$ ); and  $\square$ ,  $L = 0.01m$  ( $L/D = 0.14$ ). The dashed curve is for  $L = 0.10m$  ( $L/D = 1.43$ ) with a frictionless right endwall at  $z/L = -0.5$ .

Furthermore, for the first 2/3 of the flowing layer, the depth of the flowing layer in the long tumbler is larger than that in the short tumbler, and both are much larger than that for the quasi-2D tumbler, though both are less for the final 1/3 of the flowing layer.

This difference of the flowing layer depths is also illustrated in figure 3.4, which shows the flowing layer structure along the length of the tumbler at the mid-length of the flowing layer ( $x = 0$ ). Based on mass conservation, the thinner flowing layer for the quasi-2D tumbler at  $x = 0$  is consistent with the higher streamwise velocity in the shorter tumblers that has been measured in quasi-2D experiments (Pohlman *et al.*, 2006b). Moreover, as shown in figure 3.4, the depth of the flowing layer decreases near the endwalls for all

three tumblers, corresponding to the slower streamwise velocity near endwalls shown in figure 3.1. For the two shorter tumblers, the maximum flowing layer depth occurs at the mid-length of the tumbler, while for the longer tumbler the maximum depth is around  $z/L = \pm 0.2$ . Apparently, it is closely related to the high streamwise flow rate at these two positions due to the axial flow near endwalls in the long tumbler, which is discussed in more detail in a later section. This point is validated by the dashed curve of the long tumbler that has a frictionless endwall at  $z/L = -0.5$ . The flowing layer depth in this case is nearly constant from the frictionless wall to the mid-length of the tumbler but overlaps the depth profile for the case when both endwalls have friction for  $0 \leq z/L \leq 0.5$ . This clearly demonstrates that the decreased depth of the flowing layer near the endwalls and the two regions where the flowing layer is deeper in the long tumbler ( $z/L = \pm 0.2$ ) result from the frictional interactions between particles and the endwalls. Furthermore, the effects of the two endwalls on flowing structure are independent of each other.

An even better comparison of the structure of the flowing layer between the long tumbler and the two shorter tumblers is illustrated in figure 3.5, which shows contours of the flowing layer depth for these three tumblers. For the long tumbler, figure 3.5(a), the flowing layer is deepest at two regions slightly upstream of the axis of rotation. For the short tumbler and quasi-2D tumbler, shown in figures 3.5(b) and (c), the tumblers are short enough so that two regions merge into a single region so the flowing layer is deepest at the center of the length of the tumbler. Moreover, consistent with the skewness of the flowing layer shown in figure 3.3, the contours of the flowing layer depth are not symmetric about the axis of rotation of the tumbler at  $x = 0m$ . The layer is deepest upstream of the tumbler axis for  $L = 0.10m$  and  $L = 0.05m$ , and downstream for the

quasi- $2D$  tumbler. Similar results were obtained for 3mm particles in the above three tumblers, except that the layer was deepest downstream of the axis of rotation indicating that rheological properties of the particle flow also plays a role in the flowing layer depth.

### 3.4. Streamwise Velocity Field Beneath the Visible Free Surface

Closely related to the structure of the flowing layer in the long tumbler, there are two regions of high streamwise velocity, as shown in figure 3.6 for  $xz$  planes at different depths from the top surface to near the bottom of the flowing layer. In figure 3.6, contours of streamwise velocity are plotted after subtracting the solid body rotation and normalizing by the streamwise surface velocity at the center of the tumbler,  $u_o$ . The dashed curves are the boundaries of the flowing layer. It is evident that two high velocity regions exist at the surface and all depths in the flowing layer. The axial positions are always symmetric about the mid-length of the tumbler,  $z = 0m$ , consistent with experimental measurements of the surface velocity at  $x = 0$  (Pohlman *et al.*, 2006*a,b*). However, the position of the two high velocity regions changes with depth in the flowing layer. At the surface, figure 3.6(a), these regions are downstream of the axis of the tumbler,  $x = 0m$ , and very near the endwall (note that the streamwise velocity in these regions exceeds that at the center of the tumbler at the surface). Moving deeper in the flowing layer these regions shift upstream and away from the endwalls, so that very deep in the flowing layer the high velocity region occurs upstream of the axis of the tumbler (the high velocity regions in figure 3.6(d) are as far as  $D/2$  away from the tumbler endwalls). The locations

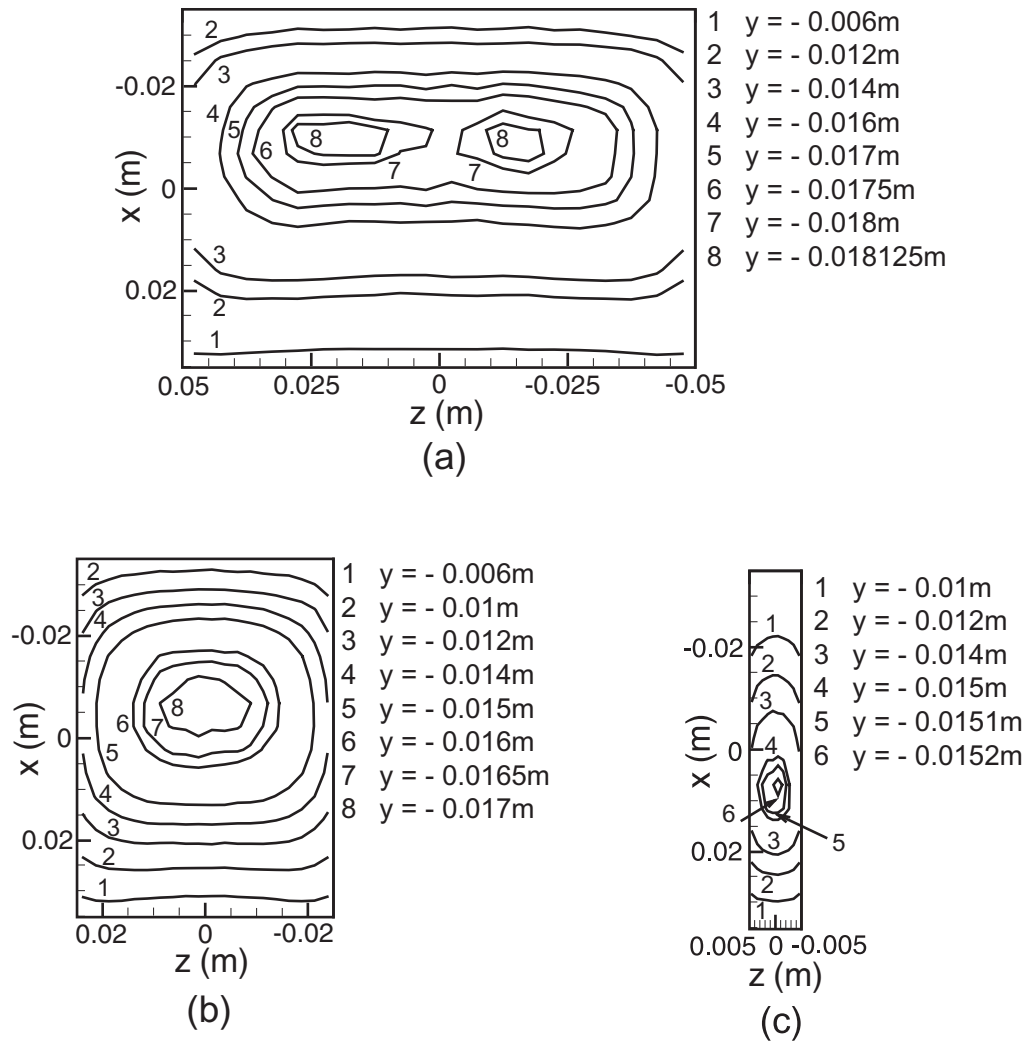


Figure 3.5. Flowing layer structure for 1.5mm particles at different depths for three tumblers shows how the length of the tumbler affects the depth of the flowing layer: (a)  $L = 0.10m$  ( $L/D = 1.43$ ); (b)  $L = 0.05m$  ( $L/D = 0.71$ ); (c)  $L = 0.01m$  ( $L/D = 0.14$ ). Flow is from top to bottom.

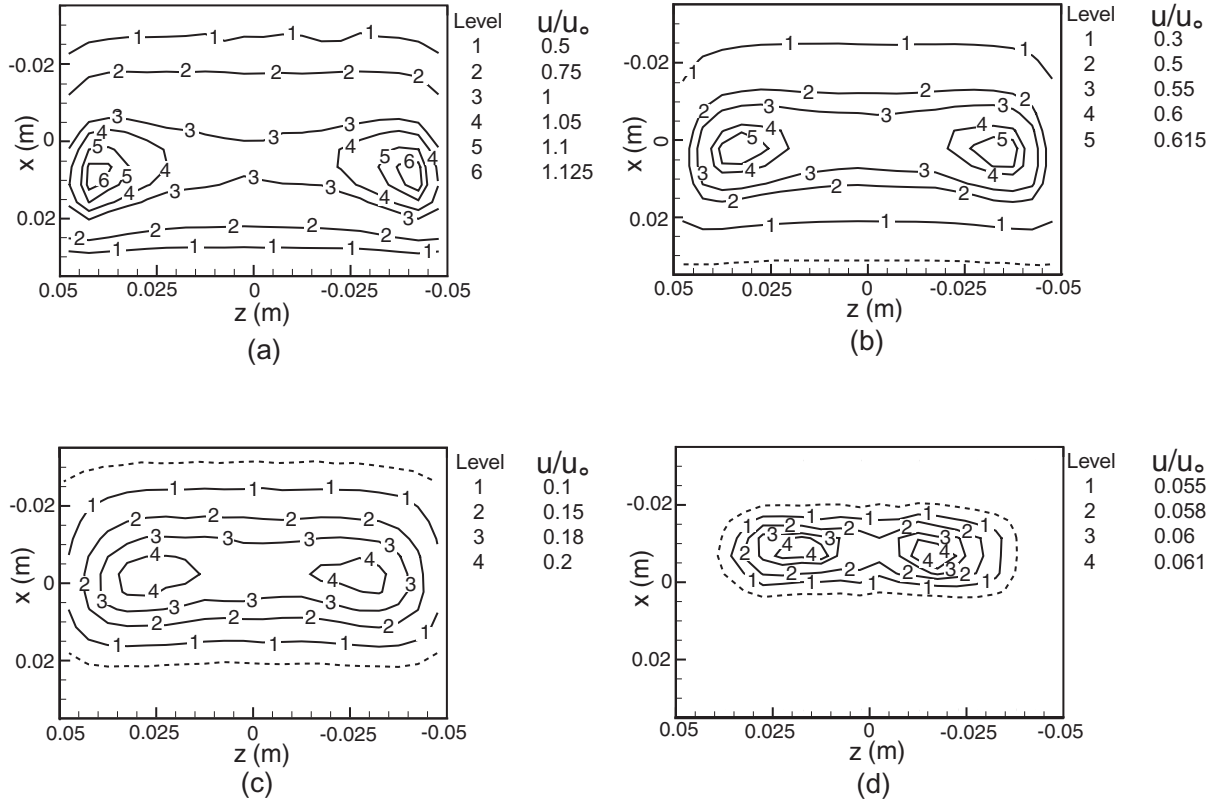


Figure 3.6. Contours of streamwise velocity at different depths in the long tumbler of  $L = 0.10m$  ( $L/D = 1.43$ ) for 1.5mm particles show how the high velocity regions shift position from the surface (a) to deep in the layer (d): (a)  $y = 0m$ ; (b)  $y = -0.006m$ ; (c)  $y = -0.012m$ ; (d)  $y = -0.017m$ . The dashed contour indicates the edge of the flowing layer at the depth indicated. Flow is from top to bottom.

of the high velocity regions deep in the layer (figure 3.6(d)) correspond to the deepest portion of the flowing layer (figure 3.5(a)).

Again, keeping one endwall frictionless validates that the friction from endwalls is the origin of these two regions with high streamwise velocity in the long tumbler. Figure 3.7

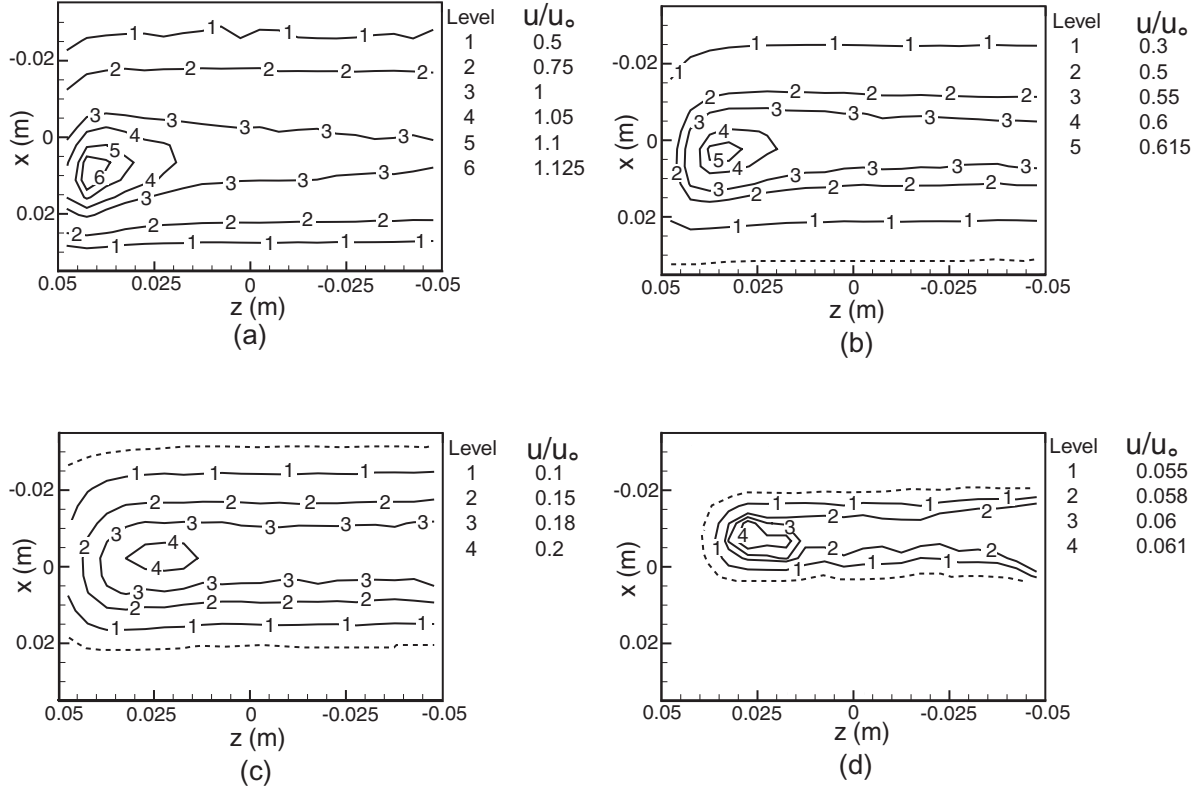


Figure 3.7. Contours of streamwise velocity at different depths in the long tumbler of  $L = 0.10m$  ( $L/D = 1.43$ ) with a frictionless endwall at  $z = -0.05m$  for 1.5mm particles. The high velocity region is associated with the frictional left endwall from the surface (a) to deep in the layer (d): (a)  $y = 0m$ ; (b)  $y = -0.006m$ ; (c)  $y = -0.012m$ ; (d)  $y = -0.017m$ . The dashed contour indicates the edge of the flowing layer at the depth indicated. Flow is from top to bottom.

shows the streamwise velocity contours for this case at the same four depths as illustrated in figure 3.6. Clearly, no high velocity region exists near the frictionless endwall, and the magnitude as well as positions of the high velocity regions associated with the frictional endwall are almost identical to those in figure 3.6. It is also clear that the effects of the

frictional endwall are negligible throughout the depth of the flowing layer by about  $D/2$  from the endwall, consistent with measurements of the surface velocity (Pohlman *et al.*, 2006b).

Simulations for the short and quasi- $2D$  tumblers show the effect of the interaction between two endwalls on the streamwise velocity field. In figure 3.8, for the short tumbler, there still exist two regions of high streamwise velocity in the upper portion of the flowing layer, but these two regions move toward each other deeper in the layer until they merge at the center of the tumbler at around  $y = -0.004m$ , as shown in figure 3.8(b). Below this depth, there is only one region of high streamwise velocity, which occurs at the center of the tumbler (figure 3.8(c) and figure 3.8(d)). For the quasi- $2D$  case, which is shown in figure 3.9, only one region with high streamwise velocity exists throughout the depth of the flowing layer. The streamwise positions of regions of high streamwise velocity for the short and quasi- $2D$  tumbler move upstream with the depth, just as in the long tumbler. However, the high speed region for the quasi- $2D$  case is always downstream of the mid-length of the flowing layer unlike the short and long tumblers where it is upstream of the mid-length deep in the layer. The locations of the high speed regions deep in the layer for the short and quasi- $2D$  tumblers (figure 3.8(d) and figure 3.9(b)) correspond to the deepest portion of the flowing layer (figures 3.5(b) and (c)). The shift in location of the greatest depth downstream as  $L/D$  decreases might be attributed to friction at the walls slowing the particles in the highly constrained space, so the region of the fastest flow occurs further downstream.

To assess the effect of the particle size, the same long tumbler was simulated using larger particles ( $d = 3mm$ ). Figure 3.10 shows contours of the streamwise velocity on

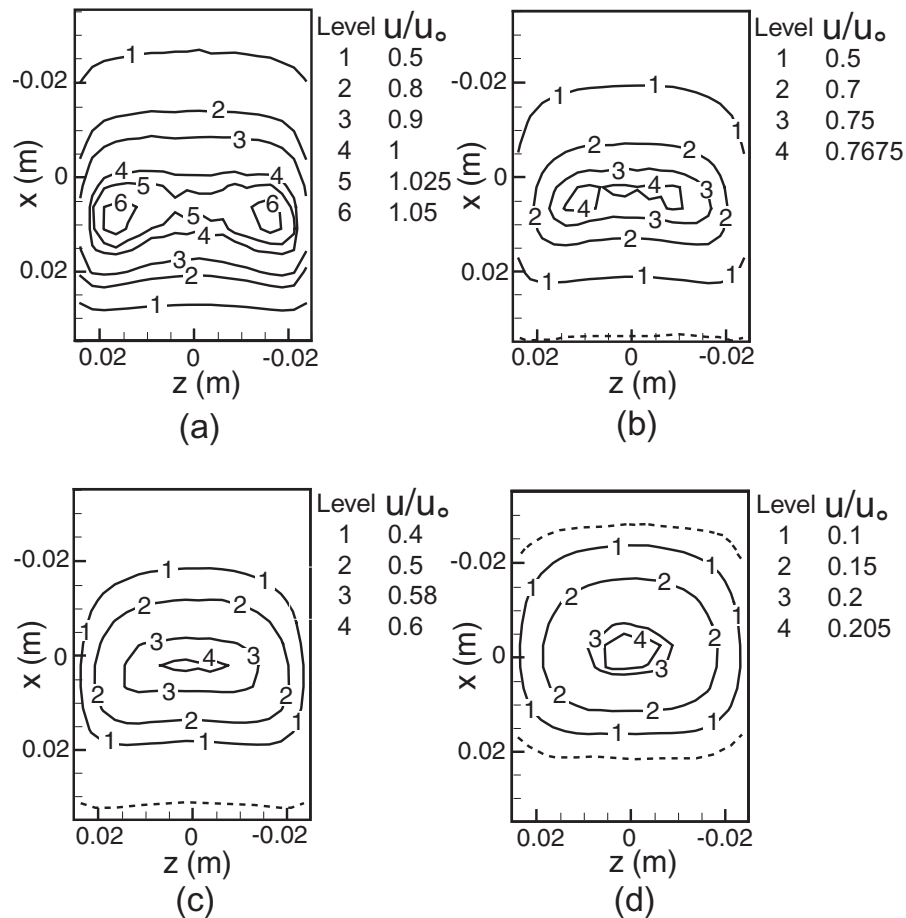


Figure 3.8. Contours of streamwise velocity at different depths in the short tumbler of  $L = 0.05m$  ( $L/D = 0.71$ ) for 1.5mm particles show how the high velocity regions shift upstream and merge from the surface (a) to deep in the layer (d): (a)  $y = 0m$ ; (b)  $y = -0.004m$ ; (c)  $y = -0.006m$ ; (d)  $y = -0.012m$ . The dashed contour indicates the edge of the flowing layer at the depth indicated. Flow is from top to bottom.

two representative planes. The two regions of high streamwise velocity still occur for the system with larger particles. Deep in the flowing layer, the streamwise positions of these two regions shift upstream and away from the endwalls, though not to the same extent

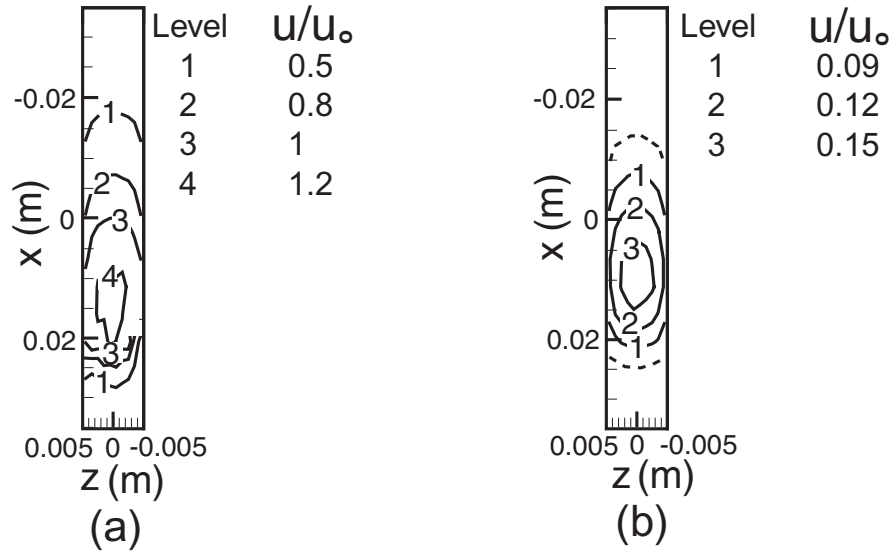


Figure 3.9. Contours of streamwise velocity at different depths in the quasi-2D tumbler of  $L = 0.01m$  ( $L/D = 0.14$ ) for 1.5mm particles have a single high velocity region: (a)  $y = 0m$ ; (b)  $y = -0.012m$ . The dashed contour indicates the edge of the flowing layer at the depth indicated. Flow is from top to bottom.

as with the smaller particles, perhaps due to the difference in the rheology of the flow for the different particle sizes.

To better show the nature of the velocity field, the streamwise velocity profiles in the axial direction and streamwise direction for different depths are shown in figure 3.11. Again, the velocities are normalized with the streamwise surface velocity at the center of the tumbler. From figure 3.11(a) it is evident that the two regions of higher streamwise velocity appear at all depths, even near the bottom of the flowing layer at  $y = -0.017m$ , though the magnitude is very small. In addition, the axial positions of the two high velocity regions move closer to the center of the tumbler deeper in the flowing layer. The

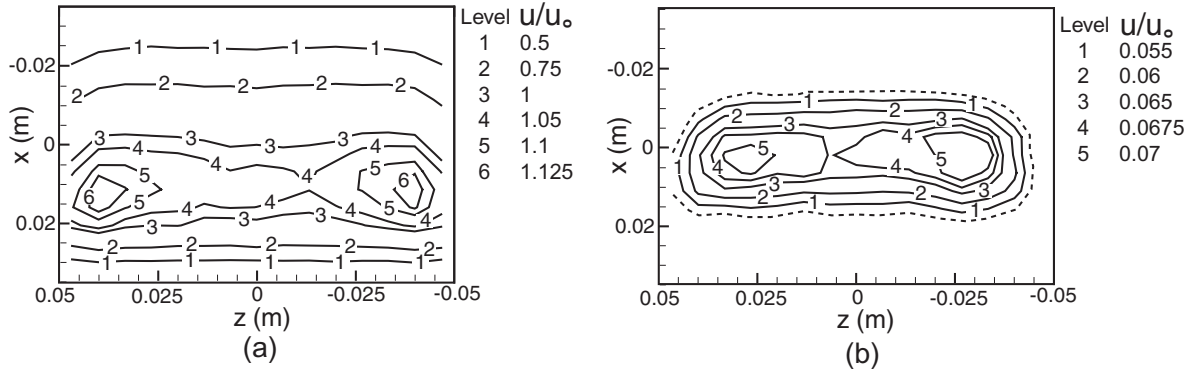


Figure 3.10. Contours of normalized streamwise velocity at different depths in the long tumbler of  $L = 0.10m$  ( $L/D = 1.43$ ) for larger 3mm particles: (a)  $y = 0m$ ; (b)  $y = -0.018m$ . The dashed contour indicates the edge of the flowing layer at the depth indicated. Flow is from top to bottom.

width of the two regions also increases with depth. From figure 3.11(b), it is clear that the maximum in the streamwise velocity shifts so that it occurs downstream of the mid-length of the tumbler in the upper part of the flowing layer and further upstream deeper in the layer.

### 3.5. Velocity Fluctuations Beneath the Visible Free Surface

The multiple interactions of particles in a flowing granular layer result in velocity fluctuations that characterize the diffusion and dissipation in the flow. “Granular temperature” has been used as a term for these fluctuations, due to the analogy with the motion of molecules in a gas. Thus, if the instantaneous velocity of granular particles is  $\mathbf{v} = (u, v, w)$  and angled brackets represent the time average, then the granular temperature is defined as  $T = \langle \mathbf{v}^2 \rangle - \langle \mathbf{v} \rangle^2 = u_{rms}^2 + v_{rms}^2 + w_{rms}^2$  (Jain *et al.*, 2002).

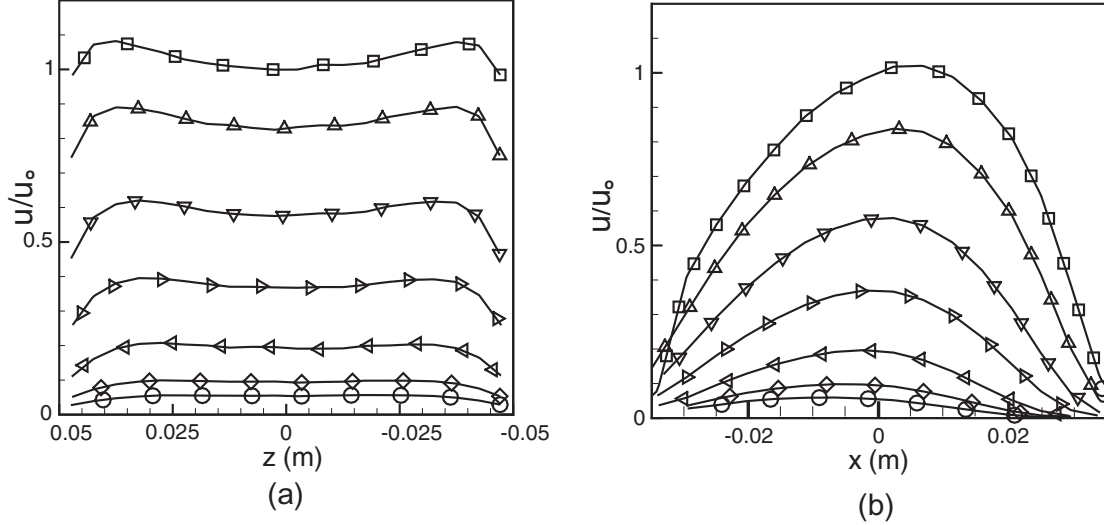


Figure 3.11. Normalized streamwise velocity  $u/u_o$  profiles at different depths in the long tumbler ( $L = 0.10m$ ,  $L/D = 1.43$ ) for 1.5mm particles: (a) at  $x = 0m$ ; (b) at  $z = 0m$ :  $y = 0m(\square)$ ;  $y = -0.003m(\Delta)$ ;  $y = -0.006m(\nabla)$ ;  $y = -0.009m(\triangleright)$ ;  $y = -0.012m(\triangleleft)$ ;  $y = -0.015m(\diamond)$ ;  $y = -0.017m(\circ)$ .

However, the concept of “temperature” is not as useful for a dissipative granular system as it is in a non-dissipative gas. We prefer to consider the random velocity fluctuations in terms of the root-mean-square (rms) values ( $u_{rms}$ ,  $v_{rms}$  and  $w_{rms}$ ), analogous to the turbulence intensity in fluid systems, which, like granular systems, are dissipative. This approach also provides a useful measure of the magnitude of the fluctuations in each of the three component directions. The total velocity fluctuations can be calculated as

$$V_{total,rms} = \sqrt{\langle \mathbf{v}^2 \rangle - \langle \mathbf{v} \rangle^2} = \sqrt{u_{rms}^2 + v_{rms}^2 + w_{rms}^2}.$$

In figure 3.12 the spanwise profiles of the total and individual components of velocity fluctuations at the free surface normalized by the streamwise surface velocity at the center

of the tumbler,  $u_o$ , are plotted for the three tumblers. The velocity fluctuations for all three components of velocity generally increase near the endwalls, while the fluctuations are smallest near the axial center of the tumbler. Moreover, the transverse and axial fluctuations are always similar in magnitude and both are smaller than the streamwise fluctuations. The lateral confinement of the endwalls reduces the axial velocity fluctuations,  $w_{rms}$ , immediately adjacent to the endwalls for the short tumbler and the long tumbler. (A denser mesh of bins near the endwalls to increase resolution in the long tumbler is necessary to adequately resolve the fluctuations.) For the quasi-2D tumbler, fluctuations in all three velocity components drop immediately adjacent to the endwalls so that the total velocity fluctuation,  $V_{total,rms}$ , decreases near endwalls rather than increasing as it does in the long and short tumblers.

The normalized fluctuations along the streamwise direction for the three tumblers are shown in figure 3.13. The tumbler length has little effect on the general nature of the velocity fluctuations in the streamwise direction. In all cases, except for very near the downstream end of the flowing layer, the surface velocity fluctuations grow monotonically along the length of the flowing layer, even after the mean streamwise velocity decreases after the mid-length of the flowing layer (figure 3.11(b)). This is consistent with MRI measurements (Caprihan & Seymour, 2000), although the diffusion coefficient was measured rather than the velocity fluctuations. Thus, near the downstream end of the flowing layer the velocity fluctuations may be larger than the local average velocity. For the long tumbler and the short tumbler the fluctuations grow rapidly at first at the upstream end of the flowing layer as the flow is initiated, then increase more slowly in the middle portion of the flowing layer followed by more rapid growth again in the downstream portion

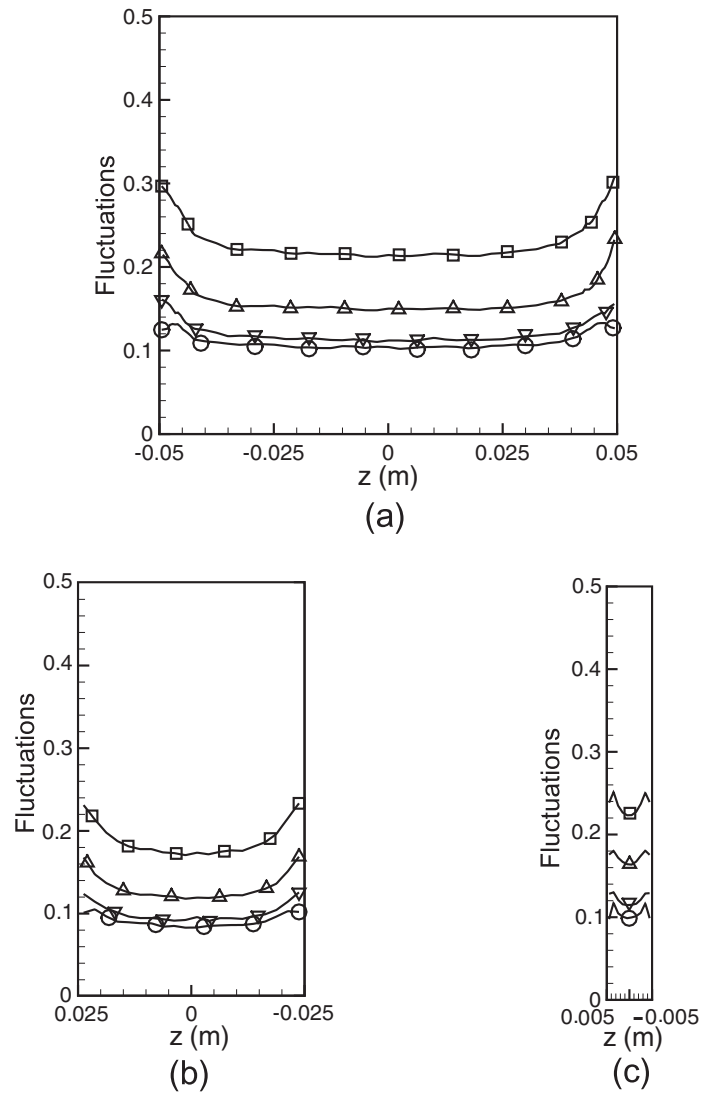


Figure 3.12. Normalized velocity fluctuations on the free surface ( $y = 0m$ ) at  $x = 0m$ , along the length of the three tumblers for 1.5mm particles: (a)  $L = 0.10m$  ( $L/D = 1.43$ ); (b)  $L = 0.05m$  ( $L/D = 0.71$ ); (c)  $L = 0.01m$  ( $L/D = 0.14$ ). Symbols:  $V_{total,rms}/u_o$  ( $\square$ );  $u_{rms}/u_o$  ( $\triangle$ );  $v_{rms}/u_o$  ( $\nabla$ );  $w_{rms}/u_o$  ( $\circ$ ).

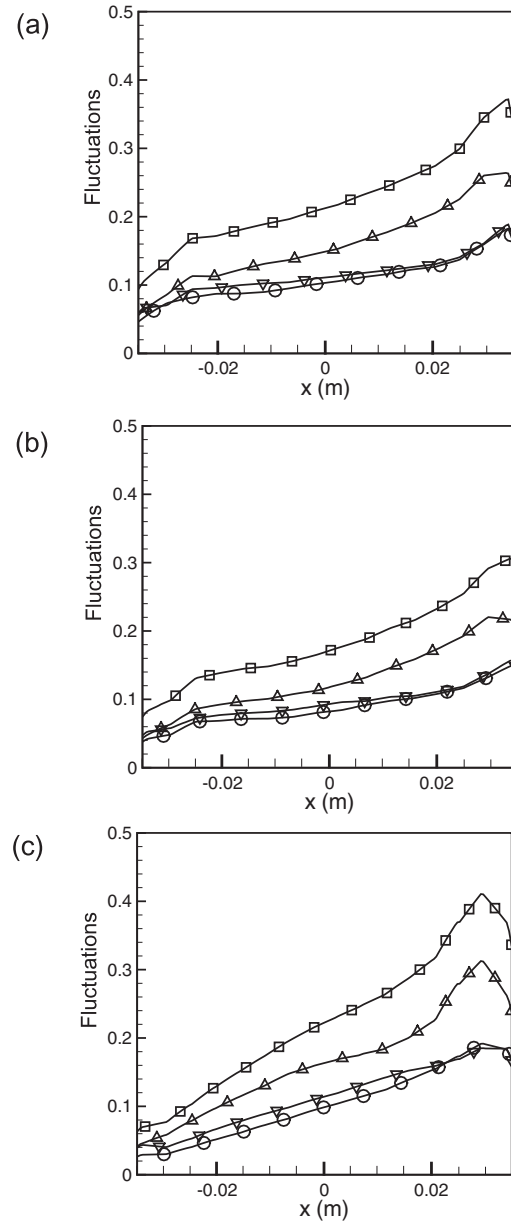


Figure 3.13. Normalized velocity fluctuations on the free surface at  $z = 0m$  along the streamwise direction of three tumblers for 1.5mm particles generally increase from the beginning to the end of the flowing layer: (a)  $L = 0.10m$  ( $L/D = 1.43$ ); (b)  $L = 0.05m$  ( $L/D = 0.71$ ); (c)  $L = 0.01m$  ( $L/D = 0.14$ ). Symbols:  $V_{total,rms}/u_o$ ( $\square$ );  $u_{rms}/u_o$ ( $\Delta$ );  $v_{rms}/u_o$ ( $\nabla$ );  $w_{rms}/u_o$ ( $\circ$ ). Flow is from left to right.

approaching a maximum near the end of the flowing layer. In the quasi-2D case, the velocity fluctuations grow somewhat more quickly along most of the length of the flowing layer than for the long and short tumblers, with an increased growth rate near the end of the flowing layer. Again, in all cases the streamwise velocity fluctuations are larger than the transverse and axial fluctuations, which are similar in magnitude.

To understand the variation of the velocity fluctuations with the depth as well as the endwall effects, the normalized components of the velocity fluctuations are plotted in figure 3.14 for the long tumbler at the mid-length of flowing layer,  $x = 0m$ , at two representative positions: the axial center of the tumbler,  $z = 0m$  and near the endwall at  $z = -0.0475m$ . The velocity fluctuations increase moving from deep in the layer toward the surface. In the upper portion of the flowing layer, the magnitudes of all fluctuations near the endwalls are larger than their counterparts at the center, probably because the particles are rebounding off the endwall and have substantial room for motion. At the free surface, the velocity fluctuations are reduced, since particle collisions occur less frequently as a result of the low number density of particles. Deeper in the flowing layer the fluctuations at the endwalls are less than those near the center due to the confinement from lateral endwalls and other particles deep in the layer. Surprisingly, detectable velocity fluctuations occur even in the “fixed bed,” although they are quite small (only about 3% of  $u_o$ ). These fluctuations arise from rearrangements of particles as the gravity vector changes orientation with respect to the fixed bed as the tumbler rotates.

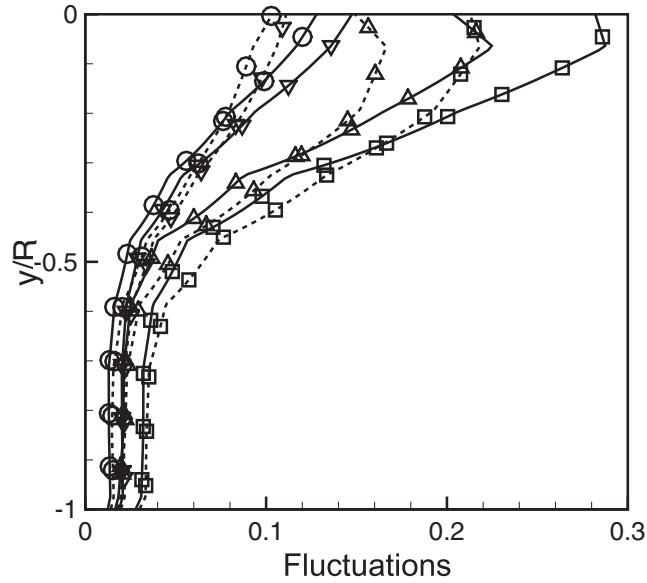


Figure 3.14. Comparison of profiles of the normalized velocity fluctuations along the depth at  $x = 0m$  in the long tumbler ( $L = 0.10m$ ,  $L/D = 1.43$ ) for 1.5mm particles: at the center of tumbler (dashed curves,  $z = 0m$ ) and near the endwall at a location of  $z = -0.0475m$  (solid curves). Symbols:  $V_{total,rms}/u_o(\square)$ ;  $u_{rms}/u_o(\Delta)$ ;  $v_{rms}/u_o(\nabla)$ ;  $w_{rms}/u_o(\circ)$ .

### 3.6. Axial Velocity in the Tumbler

Recent measurements of the velocity on the surface of the flowing layer by Pohlman *et al.* (2006b) have shown that boundary effects introduce axial flow near the endwalls in long tumblers, as indicated by the curved streamtraces at the surface of the flowing layer in figure 3.2. The axial velocity is relatively small – only about  $O(0.1)$  of the streamwise surface velocity at most (Pohlman *et al.*, 2006b) – but may be significant with respect to transport of material near the endwalls (Santomaso *et al.*, 2004).

As shown in the contour plots of axial velocity for the free surface in the long tumbler in figure 3.15(a), the simulation captures the general character of the axial flow that has been previously explored in experiments (Pohlman *et al.*, 2006*b*): the axial flow near the endwalls is toward the center of the tumbler in the upstream portion of the flowing layer and toward the endwalls in the downstream portion; the magnitude of axial velocity at downstream portion is larger than that of upstream portion; and the whole axial flow is roughly symmetric about the axial center of the tumbler, but not symmetric about the mid-length of the flowing layer. The axial velocity comes about from the combined effects of endwall friction and mass conservation (Pohlman *et al.*, 2006*a,b*). Mass conservation requires that all the particles in the fixed bed in any slice of the tumbler must flow through the flowing layer once every half revolution for a half-filled tumbler. Particles in the slices nearest the endwalls are slowed by endwall friction. Since the flowing layer is thinner near the endwalls (figure 3.4 and figure 3.5) and the streamwise velocity is slower (figure 3.11(a)), the only possibility to conserve mass is for the particles to flow axially away from the endwall in the upstream portion of the flowing layer to reach a faster streamwise flow (figure 3.6) and then move back toward the endwall in the downstream portion of the flowing layer resulting in the situation shown in figure 3.15(a).

However, unlike previous experiments, our numerical simulations allow probing the situation below the surface of the flowing layer as shown in figures 3.15(b), (c), and (d). It is quite clear that the axial flow persists deep into the flowing layer, though the magnitude of the axial velocity diminishes, as would be expected. The magnitude of the velocity in the upstream portion is less than in the downstream portion in the upper part of the flowing layer (figures 3.15(a) and (b)), but larger deep in the flowing layer

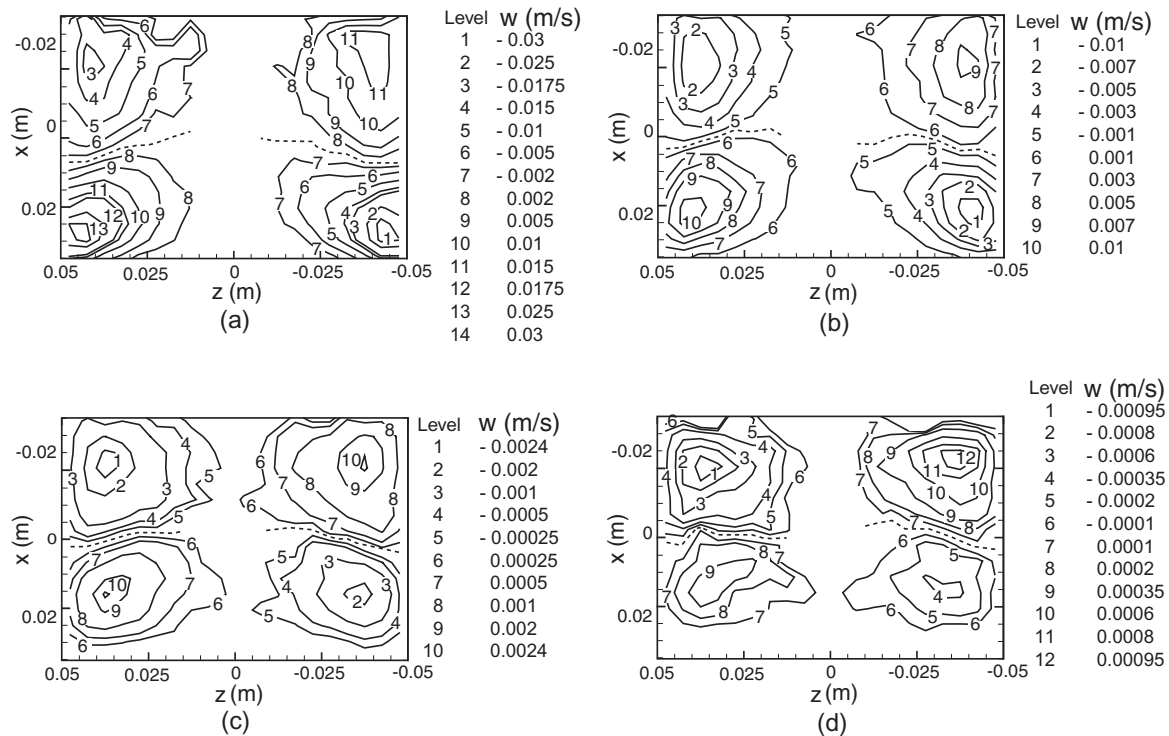


Figure 3.15. The axial flow fields at different depths in the long tumbler ( $L = 0.10m$ ,  $L/D = 1.43$ ) for 1.5mm particles show that the axial flow is retained at all depths: (a) at  $y = 0m$ ; (b) at  $y = -0.006m$ ; (c) at  $y = -0.0012m$ ; (d) at  $y = -0.0017m$ . Flow is from top to bottom.

(figure 3.15(d)). Moving from the free surface to deep in the layer, the region with axial flow does not vary much in size, but the location of the maximum axial velocity moves further from the endwall and slightly toward the axis of rotation, particularly for the downstream portion. At all depths, the interfaces between upstream and downstream portions (dashed curves) are skewed slightly upstream from the endwalls inward. These curves move upstream with increasing the depth in the flowing layer.

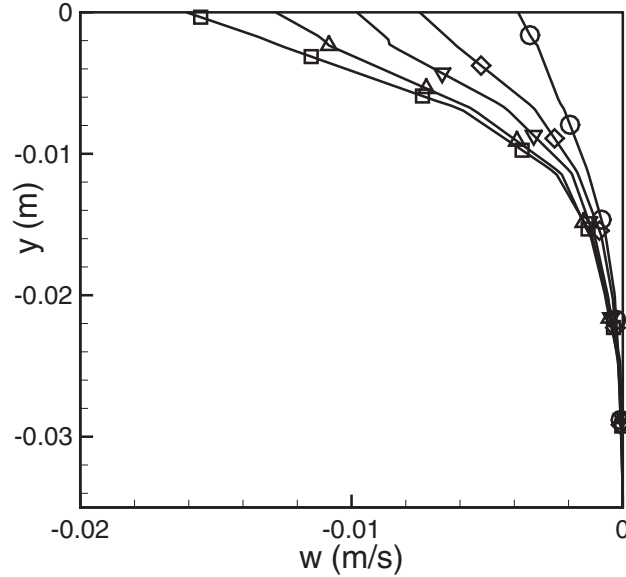


Figure 3.16. Profile of the axial velocity along the  $y$  direction at different axial positions at  $x = -0.02m$  in the long tumbler ( $L = 0.10m$ ,  $L/D = 1.43$ ) for 1.5mm particles. Symbols:  $z = 0.04m$ ( $\square$ );  $z = 0.035m$ ( $\Delta$ );  $z = 0.03m$ ( $\nabla$ );  $z = 0.025m$ ( $\diamond$ );  $z = 0.02m$ ( $\circ$ ).

It is helpful to consider the depth-wise profile of axial velocity. In figure 3.16, the axial velocity at  $x = -0.02m$ , near where maximum axial velocity occurs, is shown for different axial positions. Since this is the upstream portion of the flowing layer, the axial velocity is directed away from the left endwall ( $w < 0$ ) for portions in the left half of the tumbler ( $z > 0$ ). It is clear that the axial velocity extends deep into the flowing layer. The axial velocity has a nearly linear profile in the upper portion of the flowing layer with a smooth transition to the fixed bed.

The effect of the endwalls on the granular system has two components: the lateral confinement through collisions between endwalls and particles, and the tangential frictional

force between endwalls and particles from which the axial flow arises due to mass conservation. Therefore, the axial flow associated with the two endwalls should be independent of each other for a long enough tumbler. In fact, Pohlman *et al.* (2006b) indicated that for  $L/D > 1$ , the effects of the endwalls do not interact with one another. To confirm this, the axial flow of the long tumbler ( $L = 0.10m$ ,  $L/D = 1.43$ ) is compared with two other cases: the same tumbler but with one frictionless endwall at  $z = -0.05m$  (lateral confinement only) and a longer tumbler,  $L = 0.15m$  ( $L/D = 2.14$ ). The axial velocity profiles of these three cases are compared quantitatively along the axial ( $z$ ), streamwise ( $x$ ) and transverse ( $y$ ) direction in figure 3.17, figure 3.18, and figure 3.19. In figure 3.17, the patterns of axial velocity profiles on the free surface at the frictional end of three cases are comparable, though the pattern is necessarily shifted for the  $L = 0.15m$  case. The axial velocity at the frictionless endwall is negligible, confirming that the axial velocity arises solely due to friction at the endwall not lateral confinement.

Figure 3.18 illustrates that the axial velocity profiles along the streamwise direction at the free surface a short distance from the frictional endwall are not affected by the length of the tumbler or the frictionless endwall. Likewise, profiles of the axial velocity through the depth of the flowing layer (figure 3.19) collapse almost perfectly. These results indicate that the axial flow near the two endwall regions results solely from the friction interaction between the endwalls and the particles (not particle exclusion at the endwalls) and that the effect penetrates through the depth of the flowing layer. Furthermore, these results are consistent with experiments measuring the axial surface velocity (Pohlman *et al.*, 2006b) that indicate these endwall flows are independent of each other and independent on the tumbler length for long tumblers.

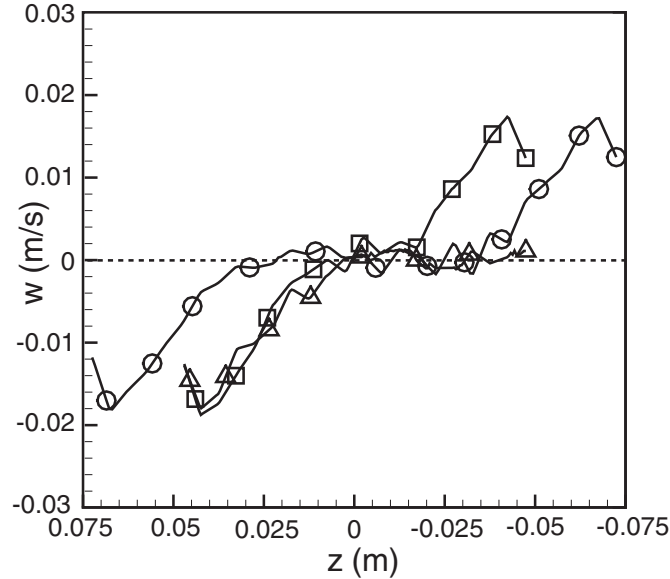


Figure 3.17. The free surface axial velocity at  $x = -0.02m$  along the axial direction for 1.5mm particles matches near the frictional endwalls regardless of the tumbler length:  $\square$ ,  $L = 0.10m$  ( $L/D = 1.43$ ), both endwalls are frictional;  $\circ$ ,  $L = 0.15m$  ( $L/D = 2.14$ ), both endwalls are frictional;  $\triangle$ ,  $L = 0.10m$  ( $L/D = 1.43$ ) with a frictionless endwall at  $z = -0.05m$ .

### 3.7. Conclusions

Endwalls play a major role in the structure and velocity field in the flowing layer of a cylindrical tumbler. When the endwalls are far enough apart, approximately one tumbler diameter ( $D$ ) or more from each other, independent regions of altered flow occur proximal to the endwalls throughout the depth of the flowing layer, consistent with the measurements at the surface (Pohlman *et al.*, 2006b). The friction at the endwalls slows the particles that are immediately adjacent so that 1) the flowing layer is not as deep as further from the endwalls, and 2) the streamwise velocity of the particles is slower

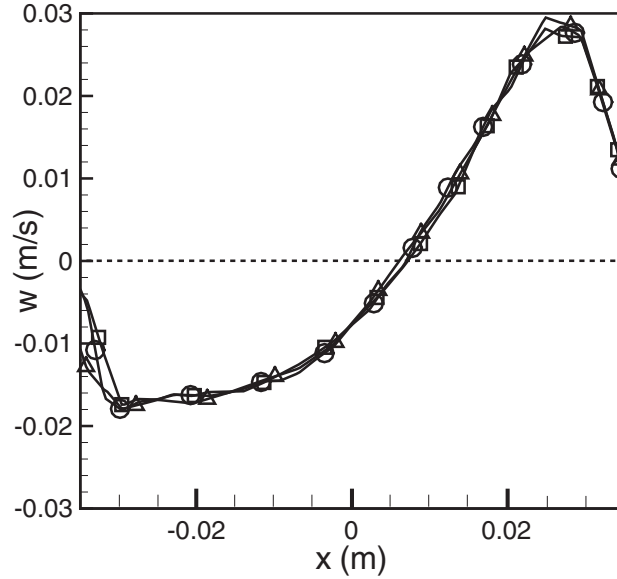


Figure 3.18. Free surface axial velocity  $0.01m$  from the frictional endwall ( $z = 0.04m$  for two  $L = 0.10m$  ( $L/D = 1.43$ ) tumblers and  $z = 0.065m$  for  $L = 0.15m$  ( $L/D = 2.14$ ) tumbler) along the streamwise direction for  $1.5mm$  particles match, regardless of the tumbler length:  $\square$ ,  $L = 0.10m$  ( $L/D = 1.43$ ), both endwalls are frictional;  $\circ$ ,  $L = 0.15m$  ( $L/D = 2.14$ ), both endwalls are frictional;  $\Delta$ ,  $L = 0.10m$  ( $L/D = 1.43$ ) with a frictionless endwall at  $z = -0.05m$ .

immediately adjacent to the endwalls than further from the endwalls. This sets up a situation in which a short distance from the endwalls, within one tumbler radius  $R$  from an endwall, the flow adjusts to accommodate mass conservation. Specifically, an axial velocity field is set up to carry particles to a faster flowing region a short distance from the endwall. Not only is the streamwise flow faster in this region than it is near the endwalls, it is faster than the flow far from the endwalls at the center of the tumbler. The

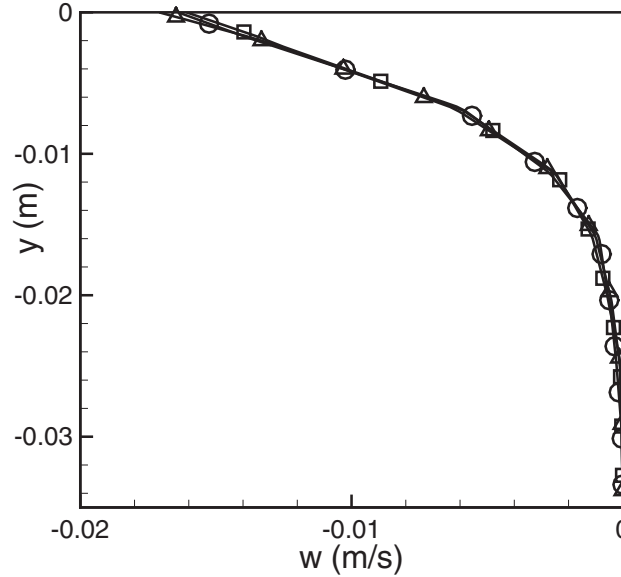


Figure 3.19. Axial velocity profile with depth at  $x = -0.02m$  and  $0.01m$  away from the frictional endwall for three cases with  $1.5mm$  particles match, regardless of the tumbler length:  $\square$ ,  $L = 0.10m$  ( $L/D = 1.43$ ), both endwalls are frictional;  $\circ$ ,  $L = 0.15m$  ( $L/D = 2.14$ ), both endwalls are frictional;  $\triangle$ ,  $L = 0.10m$  ( $L/D = 1.43$ ) with a frictionless endwall at  $z = -0.05m$ .

flowing layer deepens to further accommodate the particles moving into the region from next to the endwalls.

Simulations with longer tumblers or tumblers with one frictionless endwall clearly indicate that this phenomenon is a direct result of endwall friction and that it extends less than one tumbler radius from the endwall. When frictional endwalls are closer than  $2R$ , these regions of faster flow merge partially (for the short tumbler) or completely (for the quasi- $2D$  tumbler). Likewise, the regions in which the flowing layer is deeper merge as the endwalls get closer to one another. While recent experiments provide similar

results with regard to the extent of the region near the endwalls where the streamwise velocity is higher and speculate that this is a result of the impact of endwall friction on mass conservation (Pohlman *et al.*, 2006*a,b*; Santomaso *et al.*, 2004), these studies were limited to surface velocity measurements. These DEM simulations make it clear that the axial flow and accelerated streamwise flow in the region near the endwalls not only extend through the depth of the flowing layer, but also alter the depth of the flowing layer locally. Furthermore, these previous studies could only speculate on the cause of this phenomenon, though in one case it was shown that higher friction at an endwall (using sandpaper) accentuated the axial and streamwise flow measured at the surface (Pohlman *et al.*, 2006*b*). These DEM simulations with a frictionless endwall show that the axial flow, higher streamwise velocity, and deeper flowing layer typically associated with a frictional endwall are absent altogether when the endwall is frictionless.

In spite of this better understanding of the detailed flow of mono-disperse particles through the depth of the flowing layer, questions still abound. Specifically, how the frictional endwalls affect the mixing and segregation of bi-disperse particles, particularly in terms of radial segregation and pattern forming in quasi-2*D* bi-disperse systems and in terms of axial banding in long tumbler, remains an open question. Likewise, the impact of frictional interactions between particles and walls for curved walls is not clear. For instance, it is unclear if friction can cause an axial flow in spherical tumblers. Nevertheless, further experiments and simulations can shed light on these and other issues, particularly now that it is possible to simulate large numbers of particles using reasonably low cost computers.

## CHAPTER 4

## The Onset of Granular Axial Segregation in Rotating Cylindrical Tumblers

**Chapter Summary:** Axial segregation in a long rotating tumbler has attracted much attention in recent years, but the fundamental onset mechanism of axial segregation is still unclear. Several assumptions are used in models of axial segregation including axial flow between bands and negative diffusivity to drive axial segregation. In this chapter, the onset of axial segregation for binary mixtures having different size particles in rotating tumblers is quantitatively investigated using the discrete element method.

DEM simulations show the existence of a small axial flow between segregated bands of small and large particles even after the bands are fully developed. The direction and strength of the axial flow are correlated with the concentration gradient along the axial length as the bands develop. Axial segregation occurs when the axial flow rate of the two types of particles differs in the upstream and downstream portions of the flowing layer. This difference arises from the non-uniform distribution of axial velocity in the flow and the redistribution of the two types of particles within transverse planes due to radial segregation. The net result of this differential axial transport of the two particle species in transverse planes appears like a diffusion process with negative diffusivity, justifying previous models for axial segregation as a phase transition characterized by a governing equation with a negative diffusivity. Endwalls can initiate axial segregation, since the

endwalls drive an axial flow due to friction. The simultaneous radial segregation results in small particles being driven further from the endwalls, while large particles accumulate at the endwalls. Once this occurs, other bands form due to the gradient in particle concentration near the endwalls.

#### 4.1. Introduction

One of the most intriguing physical properties of granular media is the tendency of granular mixtures to segregate upon shearing or vibration. An initially homogenous binary mixture in long partially-filled, horizontal rotating cylindrical tumblers is often used as a canonical system to study granular mixing and segregation.

Though first reported by Oyama (Oyama, 1939) in 1939, axial segregation did not attract substantial attention until recent decades (Donald & Roseman, 1962; Nakagawa, 1994; Zik *et al.*, 1994; Hill & Kakalios, 1994, 1995; Jain *et al.*, 2001). And even though several interesting properties of axial segregation such as traveling waves and coarsening (Choo *et al.*, 1998; Fiedor & Ottino, 2003) have been studied, the fundamental drivers of the onset mechanisms for axial segregation are still unclear. Hill and Kakalios (Hill & Kakalios, 1994) found that the appearance of axial segregation strongly depends on the rotational speed,  $\omega$ , as well as the differences in the dynamic angles of repose between the mixed and segregated phases. They also found that for a mixture of small and large glass particles axial segregation is always initiated near endwall regions, and the bands at the endwalls are always rich in large particles. Alexander *et al.* (2004) found that the axial segregation only occurs when the size ratio of two species is large enough; Bielenberg *et al.* (2007) noted that the size of particles relative to the tumbler diameter

is also key to axial segregation; Zik *et al.* (1994) showed that the periodic modulation of tumbler diameter along the rotation axis can promote axial segregation; by studying the oscillatory dynamics for initially pre-segregated bands, Khan *et al.* (2004) found that the particle concentration along the rotation axis is closely associated with the angle of repose of segregation bands from the initial oscillatory transient to the fully segregated state.

Due to the complexity of the physics, theoretical progress has been limited. Savage (1993) and Hill & Kakalios (1994, 1995) used the concept of “negative diffusivity” to explain axial segregation. They assumed that different compositions of granular mixtures have different dynamic angles of repose, which introduces an axial drift flow between segregation bands. Zik *et al.* (1994) presented the first rigorous model to show the connection between axial drift flow and negative diffusivity. They postulated that the particles with small angle of repose have a large mobility down the axial slope, which reduces the one-dimensional mass conservation equation along the rotation axis to a diffusion equation with a negative diffusivity. To prevent particle accumulation, they assumed the existence of a counter axial flow. But as pointed out by Elperin & Vikhansky (1999), that model is problematic because it omits the size preference in the counter axial flow. Later, an improved theoretical model was developed by Aranson *et al.* (1999). They coupled two one-dimensional equations for the variation of the angle of repose and the concentration over the transverse cross sections along the rotation axis, assuming that the axial segregation is a phenomenon of phase transition similar to spinodal decomposition, which also has a negative diffusivity in its characteristic equation. Although their model successfully predicts the initial axial segregation as well as band oscillation and coarsening over long

times, there are still open questions for their model as indicated by Khan *et al.* (2004). Moreover, their model omitted the role of the radial segregation, which precedes axial segregation. In fact, segregation bands of small particles are actually the exposure of a radially segregated core of small particles reaching the visible free surface (Hill *et al.*, 1997b).

Computational simulation provides an alternative approach to study the onset of axial segregation. The Discrete Element Method (DEM) has been employed to study the granular axial segregation in rotating tumblers. The first simulation by DEM was reported by Shoichi (1998) for a rather small system with only about 1000 particles. Rapaport (Rapaport, 2002, 2007*a,b*) used DEM to study the effect of the particle size ratio, friction coefficient, and rotational speed. Taberlet *et al.* (2006) studied the dynamics of axial segregation bands including band oscillation and coarsening. But these computational studies only qualitatively reproduced the observed experimental phenomena; they did not investigate the fundamental onset mechanism for axial segregation or probe the flow deep in the bed of particles.

This work addresses the onset mechanism of axial segregation. Two interrelated issues are considered: the existence of axial flow between segregation bands and its nature below the surface, and the appearance of what may be imagined as a “negative diffusivity” during the development of axial segregation. Unlike most previous work (Hill & Kakalios, 1994, 1995; Choo *et al.*, 1998; Rapaport, 2002), in which size difference and friction coefficient difference are coupled (for example, small sand particles are rotated with large glass particles in the tumblers), here we consider the axial segregation of bi-disperse mixtures differing only in size. The outline of this chapter is as follows: first we explore the

segregation structure and axial flow field during the course of the axial segregation; next we examine the axial flow rate of individual species to clarify the onset mechanism of the axial segregation; then we consider the conditions that trigger axial segregation and the role of axial flow and radial segregation in the last section.

## 4.2. Numerical Parameters

The parameters of simulation are as follows: diameter of the tumbler is  $D = 2R = 0.08m$ ; the length of the tumbler is  $L = 2D = 0.16m$ ; equal volumes of small and large particles of radii  $0.001m$  and  $0.002m$  fill 20% of the tumbler volume; gravitational acceleration is  $g = 9.8m/s^2$ ; particle properties correspond to glass (density  $\rho = 2500kg/m^3$ , restitution coefficient  $e = 0.97$  (Ristow, 2000)). To provide a random mixture of particles, as introduced in Chapter 2, the two species are initially represented by mass points randomly distributed in the tumbler without gravitational force; then the radii of the particles grow until they reach the required size; next, the gravitational acceleration is applied allowing the particles to settle to the lower portion of the horizontal tumbler. Extra particles above a flat top surface are removed leaving about 13,800 particles in the simulation. To avoid a close-packed structure, the particles have a normal size distribution with a variance of  $(0.1d)^2$ , where  $d$  is the particle's diameter. The friction coefficients among particles and between particles and walls are set to  $\mu = 0.6$ ; in order to save computer time, the collision time is  $\Delta t = 1.0 \times 10^{-3}s$ , consistent with previous simulations (Taberlet *et al.*, 2006). The integration time step is  $\Delta t/40 = 2.5 \times 10^{-5}s$  to meet the requirement of numerical stability (Ristow, 2000); except where noted, the rotational speed is  $\omega = 3.14radians/s$  ( $0.5rot/s$ ). The curved cylindrical wall and two endwalls of

the tumbler are modeled using geometrically smooth surfaces, which are assumed to have infinite mass and radius for the calculation of the collision force between mobile granular particles and the walls. Using the coordinate system shown in figure 1.1, the surface of the flowing layer should theoretically be around  $y = -0.0195m$  for a 20% fill level if the surface is perfectly flat and no dilatancy is introduced during flow. For all simulations in this chapter, the tangential force model without a memory effect is used (Rapaport, 2002; Taberlet *et al.*, 2006). The memory-effect model, which uses the accumulated tangential displacement between two contacting particles (Ristow, 2000; Chen *et al.*, 2008b), was not used because it is more time consuming and provides similar results to the simpler force model.

To quantitatively study the flow, the computational domain is divided into 40 bins in the  $x$  and  $y$  dimensions, and 16 bins in the  $z$  dimension. Local flow properties are obtained by averaging values for all particles in each bin. Except where noted, to obtain statistically meaningful results, the averaging time is  $2s$  (one tumbler rotation).

### 4.3. Axial Segregation Structure

The evolution of the spatially averaged volume concentration profile is shown in figure 4.1 for small particles,  $\langle C_s \rangle$ , and large particles,  $\langle C_l \rangle$ , along the axis of rotation  $z$ , where  $\langle \rangle$  denotes the cross-sectionally averaged values. The concentrations deviate from the initially well-mixed state very quickly as large particles begins to accumulate near endwalls within 1 rotation (figure 4.1(a)). Here  $t = 0$  is the time at which the particles start to flow downward in the streamwise direction after the dynamic angle of repose is reached. After several rotations, as shown in figure 4.1(b), axial segregation is evident near

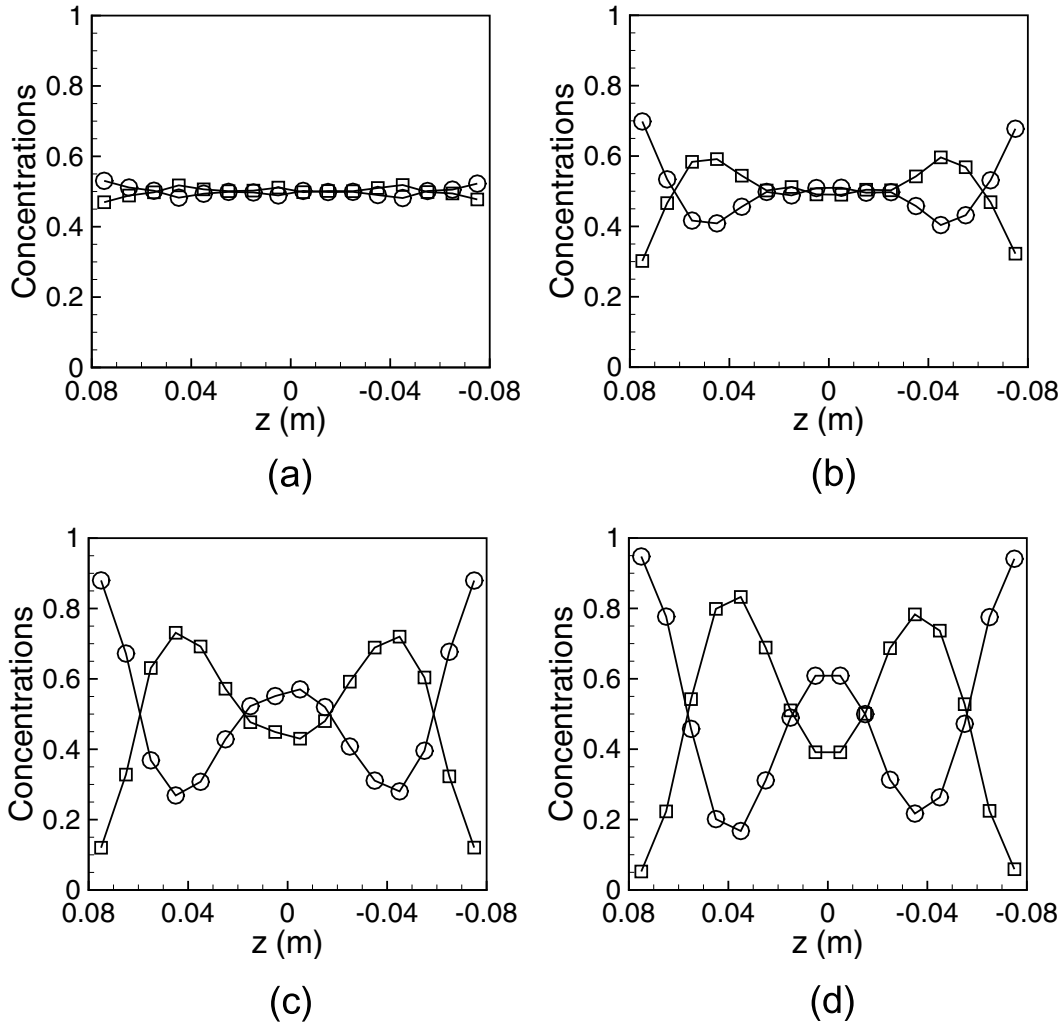


Figure 4.1. Evolution of the cross-sectionally averaged species concentrations along the axial length averaged over different time periods: (a) initial segregation (0-1 rotation); (b) intermediate segregation (4-5 rotations); (c) further segregation (20-21 rotations); (d) full segregation (49-50 rotations).  $\square$ : concentration of small particles,  $\langle C_s \rangle$ ;  $\circ$ : concentration of large particles,  $\langle C_l \rangle$ .

the endwalls ( $z = \pm 0.08m$ ) as the concentration of large particles increases significantly. This is consistent with the experimental observations (Hill & Kakalios, 1994; Fiedor & Ottino, 2003; Juarez *et al.*, 2008) that bands near endwalls appear first and that they are rich in large particles. At the same time, adjacent bands rich in small particles appear. After 20 rotations, figure 4.1(c), axial segregation is evident along the entire length of the tumbler with a third band of large particles appearing at the axial center of the tumbler ( $z = 0$ ). The segregation pattern reaches a steady segregated state (figure 4.1(d)) within 50 rotations, though the positions and concentrations of bands randomly fluctuate very slightly with time. No merging or oscillation of bands is evident up to 200 rotations.

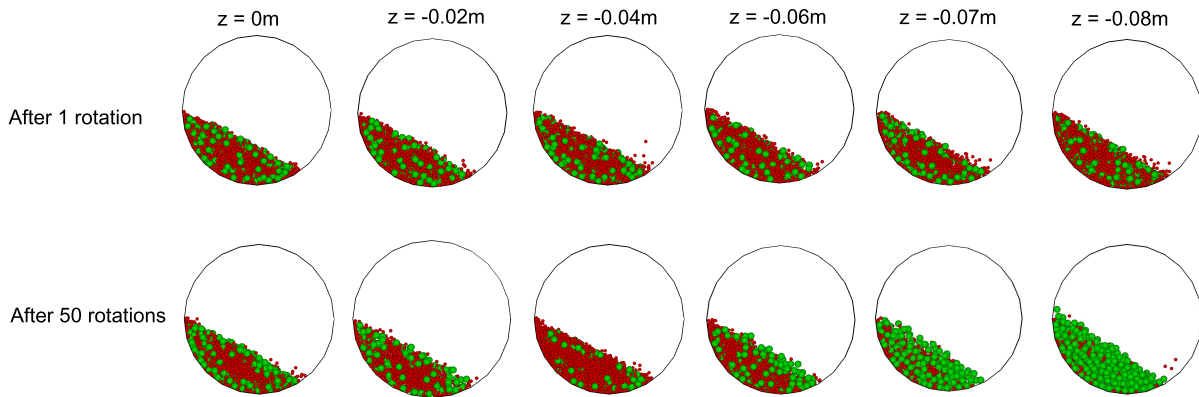


Figure 4.2. Snapshots of slices at different axial positions at two representative times: after 1 (initial axial segregation) and 50 rotations (full axial segregation).

Although MRI measurements from Hill *et al.* (1997b) have shown the outline of the radial segregation core of small particles during axial segregation, numerical simulations can provide more detailed information about the internal structure of the axial segregation

bands. Figure 4.2 shows slices at different axial positions at two representative times: initial axial segregation and full axial segregation. As observed in experiments (Hill *et al.*, 1997b; Jain *et al.*, 2001; Arndt *et al.*, 2005), radial segregation starts very early and continues for the entire course of axial segregation. The band of small particles at  $z = -0.04m$  is a consequence of the expansion of the radial core of small particles to the free surface. At steady-state, these bands of small particles are relatively pure, although there are still a few large particles present at the periphery. The band of large particles at  $z = 0m$  is much less pure at steady state. The large particles generally surround a core of small particles, but continually mix and re-segregate in the flowing layer. Between bands at  $z = -0.02$  and  $z = -0.06m$  the particles are not well segregated. Although both types of particles are initially present at the endwalls, the larger particles dominate near the endwalls at steady state ( $z = -0.07$  and  $z = -0.08m$ ).

The internal structure of the segregation can be represented in terms of iso-surfaces of small and large particle number densities, as shown in figure 4.3 for three representative times. It is clear that the core of relatively pure small particles extends along the entire axial length except right at the two endwalls after several rotations. The two lobes correspond to the two bands of small particles, and the narrow portion at the center of the tumbler is where the radial core is surrounded by a band of large particles (figure 4.3(a)). The large particles surround the narrowed core of small particles near the two endwalls and at the center (figure 4.3(b)).

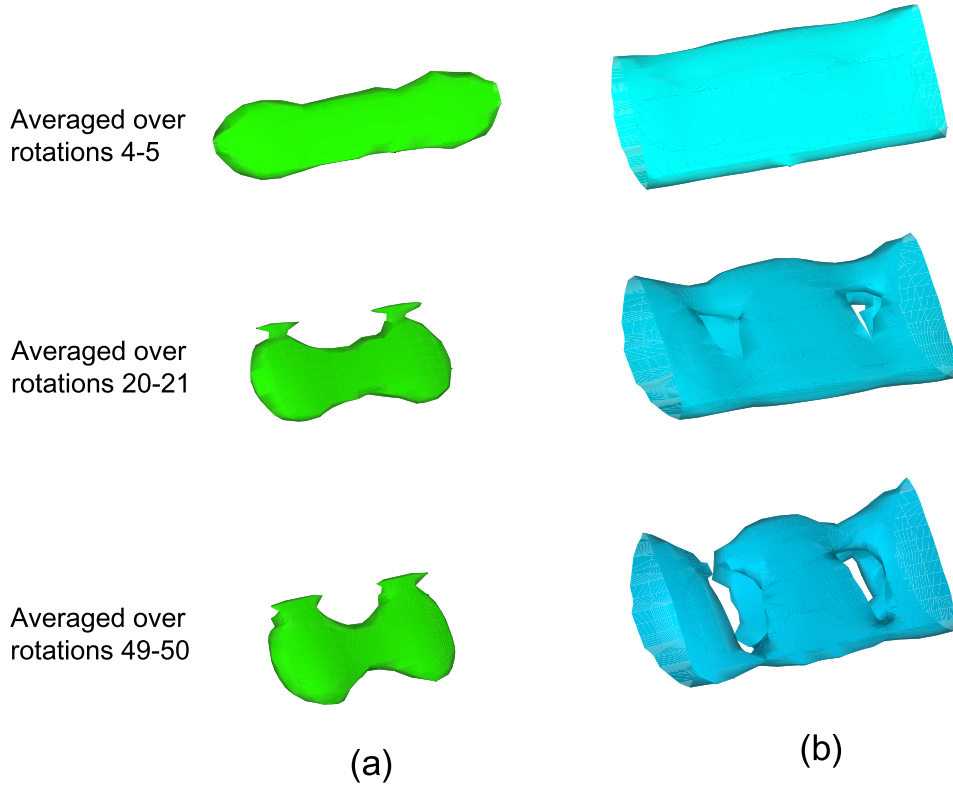


Figure 4.3. Structures of small and large particle volumes at different times as represented by the number density of particles: 4-5 rotations, 20-21 rotations, and 49-50 rotations. (a) Small particle volume,  $n_s \geq 8 \times 10^7 \text{ particles}/\text{m}^3$ ; (b) Large particle volume,  $n_l \geq 5 \times 10^6 \text{ particles}/\text{m}^3$ .

#### 4.4. Axial Drift Velocity Field during Axial Segregation

The free surface and subsurface flow fields for the mixture (both particles species) for four representative times are illustrated in figure 4.4. Each plot consists of the contours of axial velocity and streamtraces obtained from the integration of the streamwise ( $u$ ) and axial ( $w$ ) velocities. Due to the slightly variation in the dynamic angle of repose along the length of the tumbler, the free surface is represented by a plane at  $y = -0.02\text{m}$ , just below the top surface.

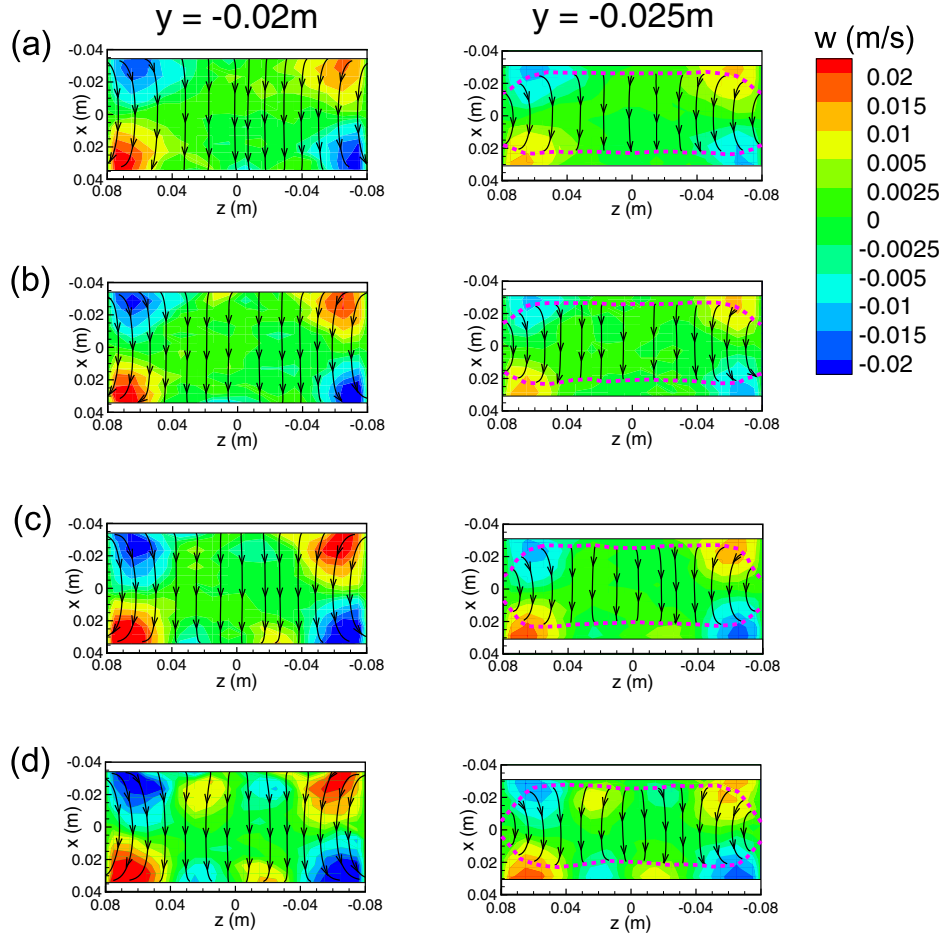


Figure 4.4. Evolution of the velocity field on the free surface at  $y = -0.02m$  and below the surface at  $y = -0.025m$ . Black curves are streamtraces from the integration of streamwise velocity ( $u$ ) and axial velocity ( $w$ ). Purple curves for  $y = -0.025m$  represent the boundary of the flowing layer, defined as the locus of points where the streamwise velocity changes from negative to positive. Color contours represent the levels of axial velocity ( $w$ ). (a) initial segregation (first 0-1 rotation); (b) intermediate segregation (4-5 rotations); (c) further segregation (20-21 rotations); (d) full segregation (49-50 rotations).

As conjectured by Savage (1993) and Hill & Kakalios (1994), convective axial flow indeed occurs during the development of axial segregation bands and this axial flow strongly depends on the evolution of species concentration distribution in the system. As axial segregation begins, shown in figure 4.4(a), the axial flow field of the bi-disperse system is similar to that for a mono-disperse system (Pohlman *et al.*, 2006b; Chen *et al.*, 2008b). Axial flows are associated with each endwall; particles near endwalls move away from the endwall in the upstream portion of the flowing layer and then move back in the downstream portion. The origin of this endwall-related axial flow has been explained in terms of mass conversion (Pohlman *et al.*, 2006b; Chen *et al.*, 2008b). Streamwise flow of particles in the transverse slices nearest endwalls is slowed by the frictional endwalls. Since all the particles in the solid body rotation part of any slice of the tumbler must pass through the flowing layer, the only possibility to accommodate the reduced streamwise velocity and the thinner flowing layer (Chen *et al.*, 2008b) near the endwalls is for these particles to flow axially away from the endwall in the upper portion of the flowing layer and then back toward the endwall in the downstream portion to conserve the mass.

As the segregation proceeds with the development of the two bands of small particles and the appearance of the band of large particles at the center of the tumbler (as shown in the concentration profile in figure 4.1(c)), another axial flows appear as shown in figure 4.4(c). Particles in the center band tend to flow toward the adjacent bands of small particles in the upstream portion of the flowing layer and flow back in the downstream portion. As axial segregation continues from figure 4.4(c) to figure 4.4(d), these axial flows grow stronger. At steady state particles in all three large particle bands (at  $z = 0, \pm 0.08m$ ) flow toward the adjacent bands of small particles in the upstream portion

of the flowing layer and back into the large particle bands in the downstream portion. Comparing the concentration profiles at this time (figure 4.1(d)) with the surface axial flow field (figure 4.4(d)), the magnitude of the axial velocity is approximately zero at the centers of the segregation bands (around  $z = \pm 0.04m$  and  $z = 0m$ ). The maximum axial flows always occur at the interface between bands (around  $z = \pm 0.065m$  and  $z = \pm 0.02m$ ). Furthermore, the magnitude of the endwall-related axial flow increases as the axial segregation bands near the endwalls develop.

The velocity field on a subsurface plane at  $y = -0.025m$  shows that the axial flow persists into the flowing layer, though the magnitude of the axial velocity diminishes with depth, similar to the mono-disperse case (Pohlman *et al.*, 2006b; Chen *et al.*, 2008b). The region with axial flow at  $y = -0.025m$  is similar to that at the free surface except that the region in which flow occurs is smaller. The interface between negative and positive axial flow regions in the upstream and downstream portions changes slightly with the depth as is the case for mono-disperse flow. Moreover, the extent of the flowing layer indicated by the dashed curves at  $y = -0.025m$  decreases, which is similar to the mono-disperse case (Chen *et al.*, 2008b). The streamwise length of the flowing layer for the bands of large particles near the endwalls and at the center (around  $z = 0m$ ) decreases with the development of axial segregation from figures 4.4(a) to (d) while the streamwise length of the flowing layer at the bands of small particles (around  $z = \pm 0.04m$ ) increases.

To better understand the cause of the axial flows between segregation bands, snapshots of the dynamic angles of repose based on the outline of the particles on the top surface of the flow at different axial positions are shown in figure 4.5. From figure 4.5(a), which is the snapshot after 1 rotation (close to the initially well mixed state), it is evident that near

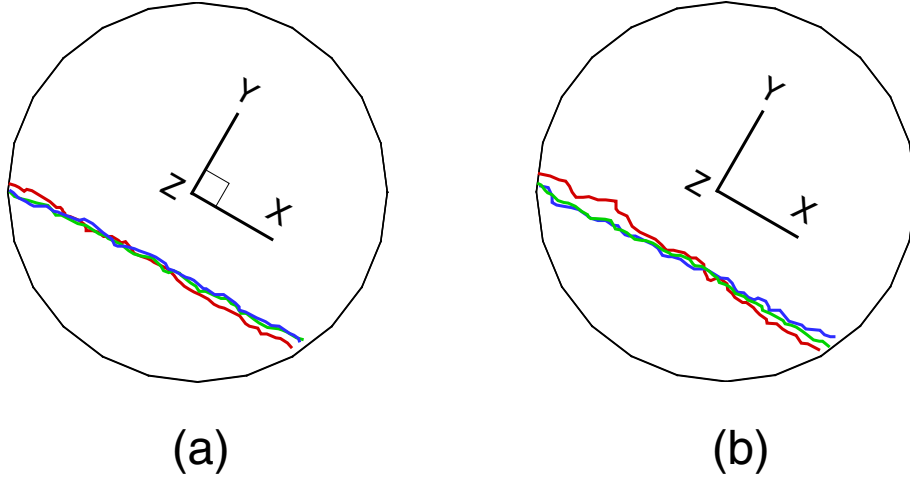


Figure 4.5. Difference of dynamic angles of repose of three representative cross sections at two times during the development of the axial segregation: (a) snapshot after 1 rotation; (b) snapshot after 50 rotations. Red curve: outline of the particle surface near the endwall ( $z = -0.08m$ ); blue curve: outline of the particle surface around the center of the band of small particles ( $z = -0.04m$ ); green curve: outline of the particle surface at the center of the center band of large particles ( $z = 0m$ ).

the endwalls ( $z = -0.08m$ ) there is a higher dynamic angle of repose than at  $z = -0.04m$  and  $z = 0$ . The higher dynamic angle of repose near endwalls is related to friction at the endwalls (Dury & Ristow, 1998). With the development of segregation bands, the dynamic angle of repose at the center band of large particles ( $z = 0m$ ) becomes larger than that at the adjacent band of small particles ( $z = -0.04m$ ), as shown in figure 4.5(b). This suggests that the angle of repose is related to the axial drift flow between segregation bands. Particles in the bands of mostly large particles fall into the band of small particles in the upstream portion of the flowing layer and go back into the large particle bands in the downstream portion due to the different dynamic angles of repose. The particle concentration and the local surface slope are in phase with each other during the whole

course of axial segregation. This is consistent with the experimental observation by Khan *et al.* (2004) that these two parameters are not independent during the process of axial segregation. Thus, the surface slope should not serve as an independent parameter in addition to species concentration, as has been done in the case of one continuum model (Aranson & Tsimring, 1999; Aranson *et al.*, 1999).

The axial drift of individual particle species during the course of axial segregation at 4-5 rotations when the two bands of small particles are developing is shown in figure 4.6. During the development of the two bands of small particles there is very little difference between the axial velocity profiles of the small and large particles at a position where the magnitude of axial flow is relative large (figures 4.6(a) and (b)). The linearly decreasing axial velocity from the surface at  $y = -0.02m$  through the depth of the flowing layer at  $y \approx -0.03m$  in figure 4.6(b) is similar to that in a mono-disperse system (Chen *et al.*, 2008b). The small axial velocity well below the surface is due to slippage between the particles and the wall. Experiments with a similar fill level of  $1mm$  and  $2mm$  glass particles in a smooth acrylic tumbler indicate that a small degree of slippage regularly occurs at the tumbler walls. The axial flow at this time only occurs near endwalls with no axial flow in the center portion of the tumbler, as shown in figure 4.6(c).

The axial flow associated with formation of the center band of large particles at 20 – 21 rotations is shown in figure 4.7. Again the axial velocity profiles of two particle species are similar, though subtle differences exist. From figures 4.6 and 4.7 it appears that the axial velocity of two species are similar during the entire course of axial segregation, so it is difficult to probe the onset mechanism of axial segregation by considering only the axial velocity field. In fact, the difference between the axial velocities of small and large

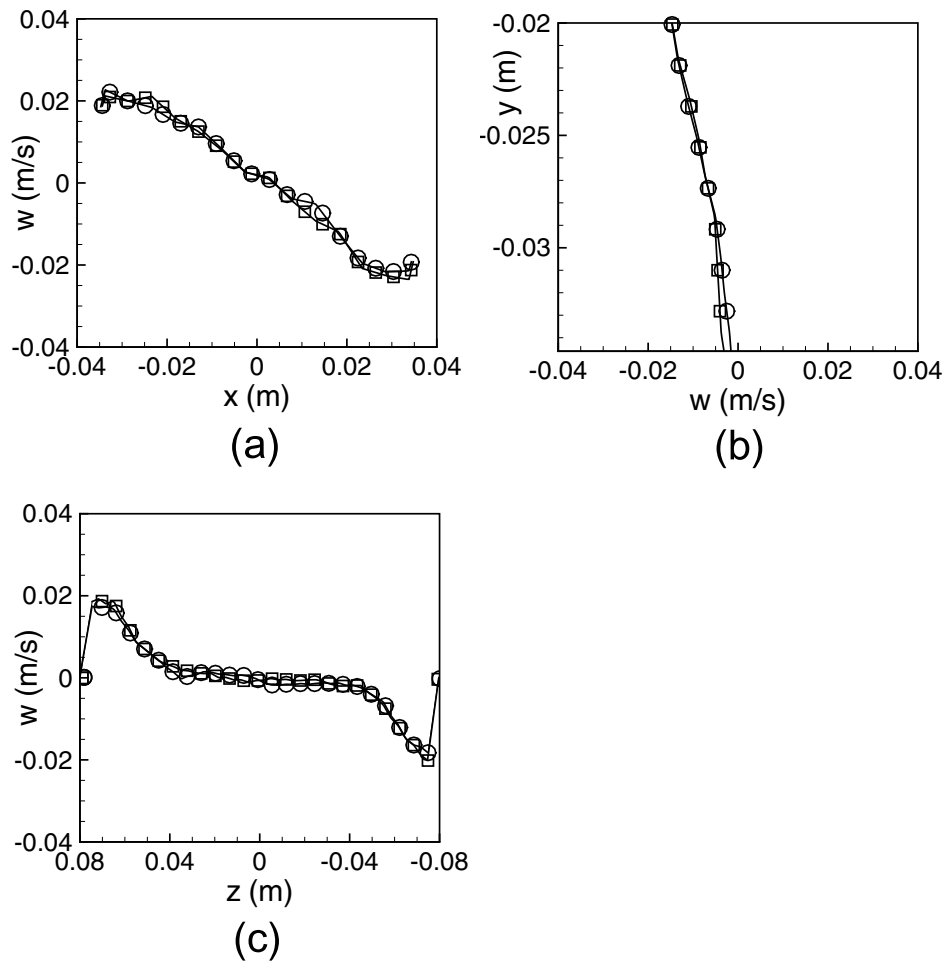


Figure 4.6. Comparison of axial velocities of two species at three representative positions during the development of the axial segregation (averaged over 4-5 rotations): (a) axial velocity along the streamwise direction on the free surface at  $y = -0.02\text{m}$  and  $z = -0.065\text{m}$ ; (b) axial velocity along the depth at  $z = -0.065\text{m}$  and  $x = 0.02\text{m}$ ; (c) axial velocity along the axial length at  $x = 0.02\text{m}$  and  $y = -0.02\text{m}$ .  $\square$ : axial velocity of small particles;  $\circ$ : axial velocity of large particles.

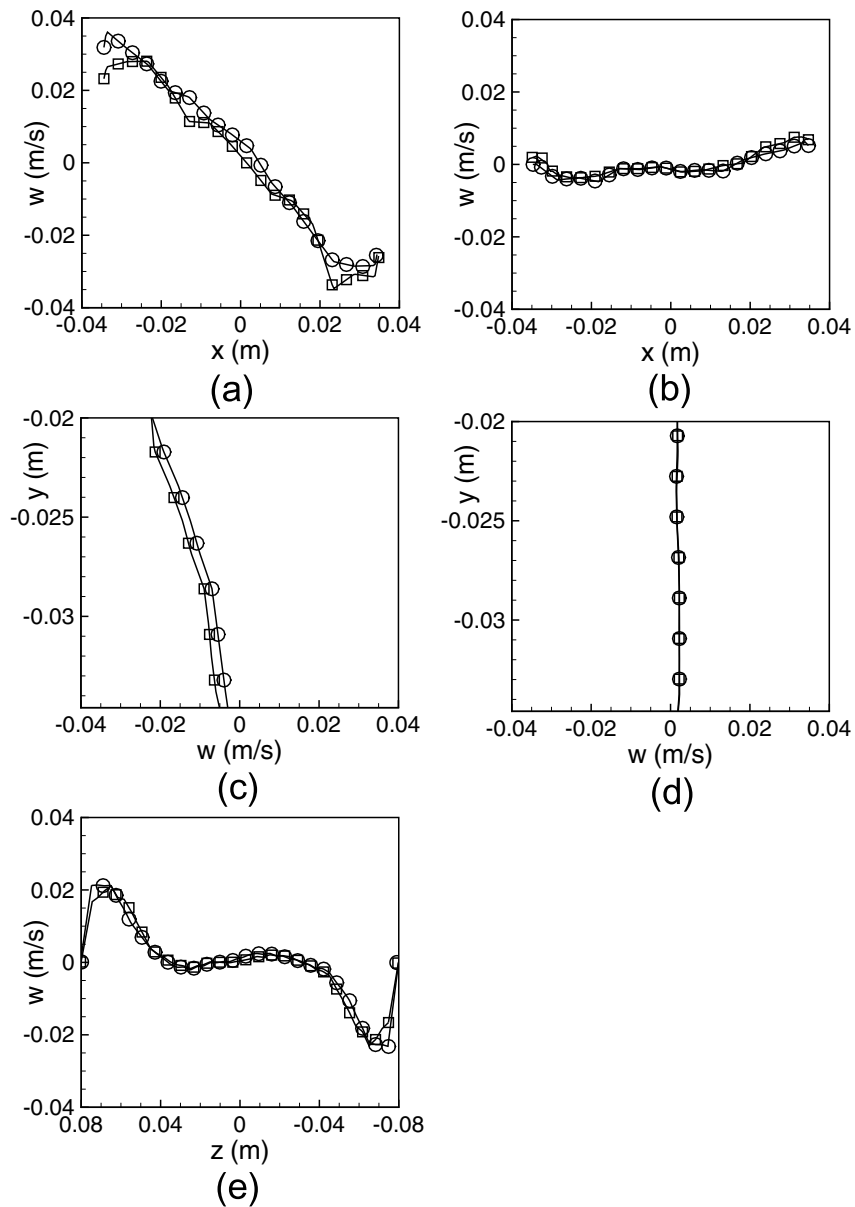


Figure 4.7. Comparison of axial velocities of two species at five representative positions during the further development of the axial segregation (averaged over 20-21 rotations): (a) along the streamwise direction on the free surface at  $y = -0.02m$  and  $z = -0.065m$ ; (b) along the streamwise direction at  $y = -0.02m$  and  $z = -0.02m$ ; (c) along the depth at  $z = -0.065m$  and  $x = 0.02m$ ; (d) along the depth at  $z = -0.02m$  and  $x = 0.02m$ ; (e) along the axial length at  $x = 0.02m$  and  $y = -0.02m$ .  $\square$ : axial velocity of small particles;  $\circ$ : axial velocity of large particles.

particles is less than 0.003 m/s (about 10% of the maximum axial velocity) in 70% of the tumbler.

#### 4.5. Axial Flow Rate during Axial Segregation

The axial flow rate on every transverse slice can be divided into the upstream portion and the downstream portion denoted as  $Q_{up,s}$ ,  $Q_{up,l}$ ,  $Q_{down,s}$ , and  $Q_{down,l}$  ( $m^3/s$ ) with the subscripts  $s$  and  $l$  indicating small and large particles. For example,  $Q_{up,s} = \sum_{i=1}^k w_{i,s} S_i n_{i,s} V_s / 0.64$ . Here the index  $i$  represents the summation over individual bins in the upstream portion.  $w_{i,s}$  and  $n_{i,s}$  are the locally averaged axial velocity ( $m/s$ ) and number density (number of particles/ $m^3$ ) of small particles in bin  $i$ , and  $S_i$  is the section area on the  $xy$  plane of bin  $i$ , which is a constant for the structured averaging mesh used here.  $V_s$  is the volume of one small particle and 0.64 is a factor accounting for the void fraction for dense sphere packing to provide an accurate numerical value for the volume flow rate. (Although this factor is borrowed from random mono-disperse packing (Jaeger & Nagel, 1992), we have verified that it is valid for the mixtures of small and large particles in our bi-disperse system, since the size ratio of the two species is not so large that the small particles can occupy voids between large particles.) Here we distinguish the “upstream” and “downstream” portions of every cross section as the streamwise position where the sign of the axial velocity changes rather than using the center of the flowing layer ( $x = 0m$ ), since the interface between negative and positive axial flow regions varies with the depth. This method to distinguish upstream and downstream portions works well for the regions with relatively strong axial flow (near endwalls in figure 4.4 (a) and (b), and the whole axial length in figures 4.4 (c) and (d)), but is more difficult to apply

in the central region of figures 4.4 (a) and (b) where the magnitude of the axial velocity is small.

Figure 4.8 shows the magnitude of the axial flow as axial segregation develops. Here the magnitude of the axial flow of the entire mixture in the upstream and downstream portions is represented by the absolute values of  $Q_{up,mix}=Q_{up,s} + Q_{up,l}$ , the total flow rate of two species in the upstream portion, and  $Q_{down,mix}=Q_{down,s} + Q_{down,l}$ , the counterpart in the downstream portion. Since the bands of large particles near the endwalls develop more quickly than the two bands of small particles and the center band of large particles, the averaging time used to calculate the axial flow rate is  $2s$  (1 rotation) early in the segregation process and  $6s$  (3 rotations) later in the process. The endwall-related axial flow starts immediately with the initial rotation (figure 4.8(a)) and its magnitude increases until fully developed segregation is achieved (figure 4.8(d)). The axial flow is initially quite small at the center portion of the tumbler before the two bands of small particles and the center band of large particles appear. Since it is quite difficult to identify the upstream and downstream portions for the small, random axial velocity, these data are indicated by dashed lines in figures 4.8(a) and (b). At later stages of axial segregation local maxima in the axial flow occur at the interface between two adjacent bands (around  $z = \pm 0.065m$  and  $z = \pm 0.02m$  in figure 4.8(d)) and minima in the axial flow occur at the centers of each band (two endwalls, around  $z = \pm 0.04m$ , and  $z = 0m$  in figure 4.8(d)). Of course, the axial flow rates in the upstream and downstream portions at all axial positions balance each other, having nearly identical magnitudes but opposite directions. Thus, the volume of particles in every slice is conserved during the development of axial segregation.

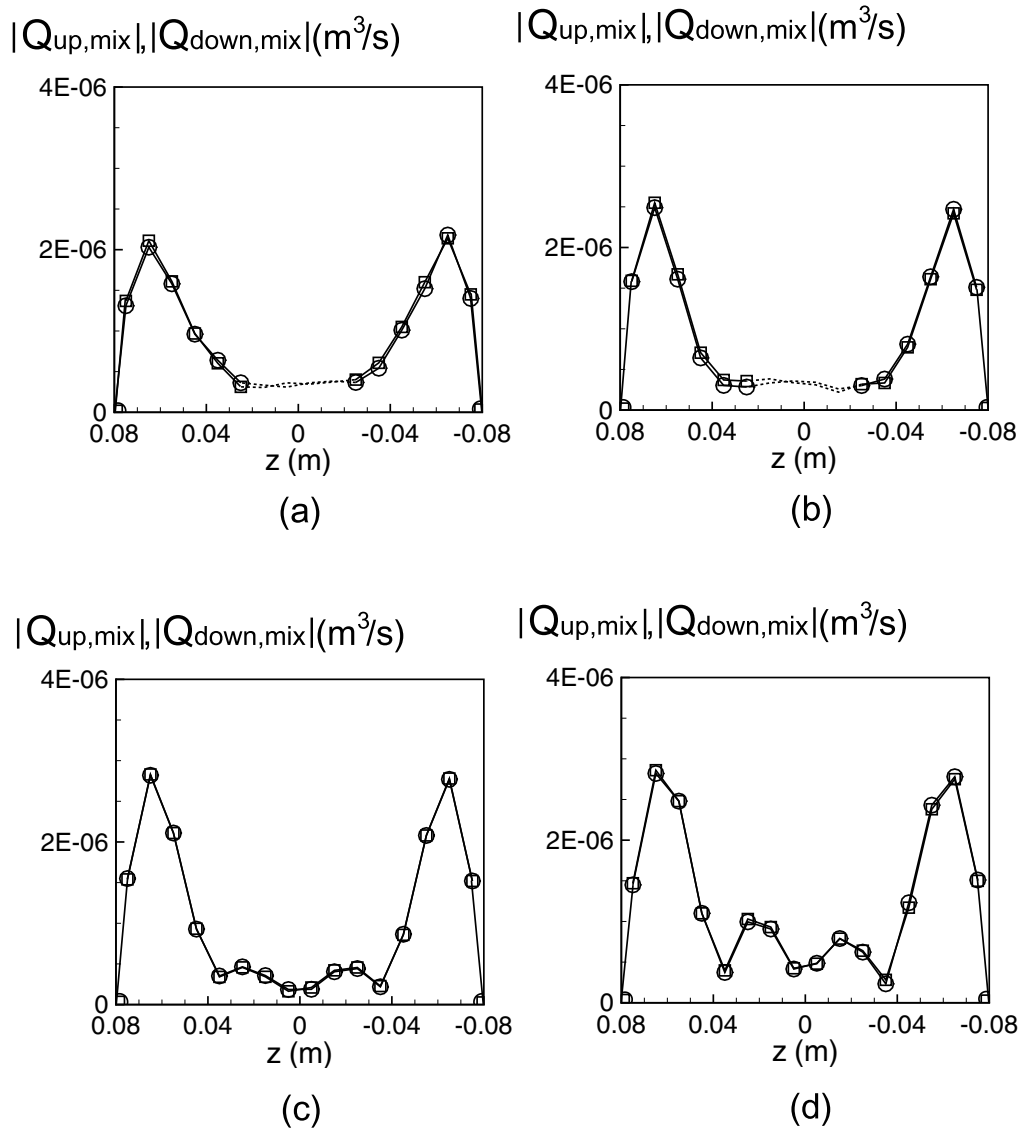


Figure 4.8. Magnitude of the axial flow rate of the mixture in the upstream and downstream portions along the axial length averaged over four different time periods: (a) initial segregation (0-1 rotation); (b) intermediate segregation (4-5 rotation); (c) further segregation (19-22 rotations); (d) full segregation (47-50 rotations).  $\square$ : magnitude of the total axial flow rate in the upstream portion,  $|Q_{up,mix}|$ ;  $\circ$ : magnitude of the total flow rate in the downstream portion,  $|Q_{down,mix}|$ .

Comparing figure 4.8 and figure 4.1 it is evident that strong axial flows correspond to steep concentration gradients. The axial flow rate and the axial gradient of small particle concentration,  $\partial \langle C_s \rangle / \partial z$ , during the development of the axial segregation, are compared in figure 4.9. The gradient is calculated as a central finite difference except near the endwall. Considering only the axial flow rate related to axial segregation (not the frictional endwalls), which occurs during the development of the center band of large particles (19-22 rotations and 47-50 rotations), the axial flow rate and the concentration gradient overlay one another for the central portion of the tumbler when scaled with an appropriate factor. In fact, the overall shapes of two profiles along the entire length of the tumbler are similar. The axial flow in the upstream portion always has the same sign as the concentration gradient at all axial positions, and the axial positions where zeros or extrema appear coincide. Therefore, it is safe to conclude that, as assumed by Savage (1993), the strength of the axial flow between segregation bands is proportional to the concentration gradient, that is  $Q_{up,mix} \propto \partial \langle C_s \rangle / \partial z$ . Of course, similar proportionalities could be written for  $Q_{down,mix}$  and  $\partial \langle C_s \rangle / \partial z$  or  $\partial \langle C_l \rangle / \partial z$ , which is essentially a mirror image of  $\partial \langle C_s \rangle / \partial z$ .

Several models of axial segregation utilize a negative diffusivity (Zik *et al.*, 1994; Hill & Kakalios, 1994, 1995; Savage, 1993; Aranson & Tsimring, 1999; Aranson *et al.*, 1999). To justify the use of a negative diffusivity model during axial segregation, we calculate the axial diffusivity of the small particles,  $K$ , with respect to the mixture at every axial position using Fick's first law of diffusion:  $\langle C_s \rangle (\langle w_s \rangle - \langle w \rangle) = -K \partial \langle C_s \rangle / \partial z$ , where  $w_s$  is the local axial velocity of small particles, and  $\langle w_s \rangle = \langle C_s w_s \rangle / \langle C_s \rangle$  is the cross-sectionally averaged axial velocity. The

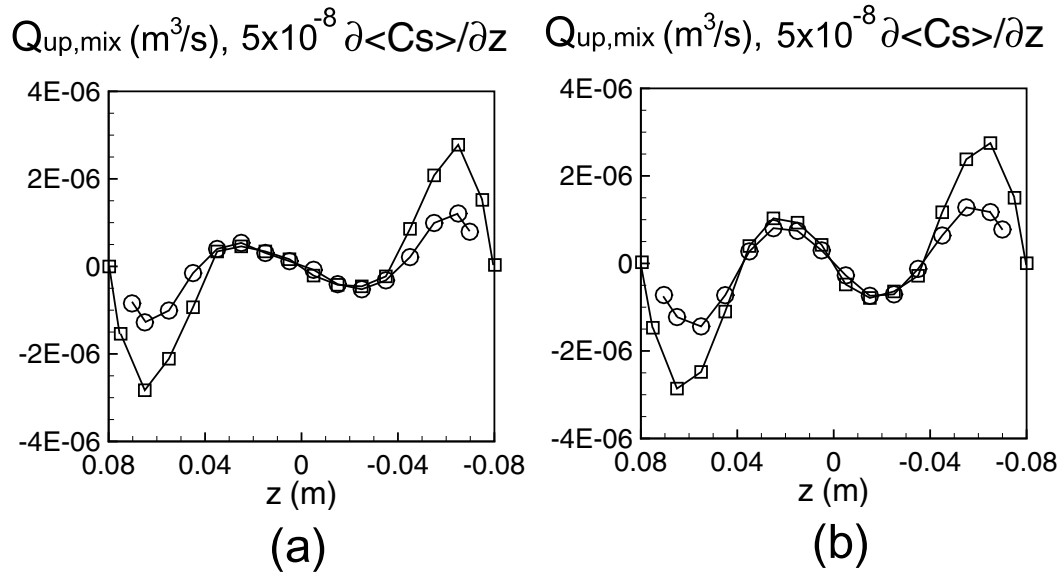


Figure 4.9. Comparison of the axial flow rate of the mixture in the upstream portion ( $\square$ ) and concentration gradient of small particles ( $\circ$ ) averaged over two time periods: (a) 19-22 rotations; (b) 47-50 rotations.

diffusivity is plotted using different scales in figure 4.10. Clearly, a net negative diffusivity exists in regions where there is axial segregation: near the endwalls in figures 4.10(a) and (b) when bands near endwalls develop, and in the center portion in figures 4.10(b) and (c) when the center bands develop. When there is no axial segregation in the center portion, as shown in figure 4.10(a), the diffusivity is positive at almost all axial positions of this portion, reflecting the tendency of the particles to mix in this region. The magnitude of the negative axial diffusivity for the bands near the endwalls is larger than that of the center bands. As expected, the magnitude of this generalized diffusivity decreases with the time and approaches zero at the fully developed segregated state in figure 4.10(d), which is discussed in detail in Appendix A. Positive or zero diffusivity tends to occur at the

centers of the segregation bands, around  $z = \pm 0.04m$  in figure 4.10(b) and  $z = 0, \pm 0.035m$  in figure 4.10(c). For a few positions (for example  $z = 0.015m$  in figure 4.10(b) where the denominator used to calculate the diffusivity,  $\partial \langle C_s \rangle / \partial z$ , is very close to zero), anomalies occur due to the randomness in the data and the problems associated with taking the derivative of noisy data.

To understand the source for the diffusivity, we consider  $| Q_{up,s} | - | Q_{down,s} |$ , the difference in the axial flow rate of small particles from the upstream portion to the downstream portion, which is shown in figure 4.11. The figure shows that the axial flow rate attributed to small particles in the upstream portion is always larger than that in the downstream portion at the axial positions where axial segregation occurs (excluding the central portion in figures 4.11 (a) and (b) due to the difficulty to tell the upstream and downstream portions as mentioned previously.) This imbalance can be used to qualitatively explain the source for the effective diffusivity and the onset of axial segregation, as shown in figure 4.12: for an initially well-mixed granular mixture, the endwall friction introduces an axial flow near endwalls, which leaves the endwalls in the upstream portion of the flowing layer and moves back in the downstream portion; due to the difference in the axial flow of small particles in the upstream portion compared to the downstream portion, small particles are conveyed from the region close to the endwalls (1) to the adjacent region (2) leaving a band rich in large particles in region 1 and a band rich in small particles in region 2. As the concentration of small particles increases in region 2, new axial flow is generated, from region 3 to region 2 in the upstream portion and back to region 3 in the downstream portion; again, from the imbalance of the axial flow rate for small particles in the up and downstream portions, this new axial flow conveys small

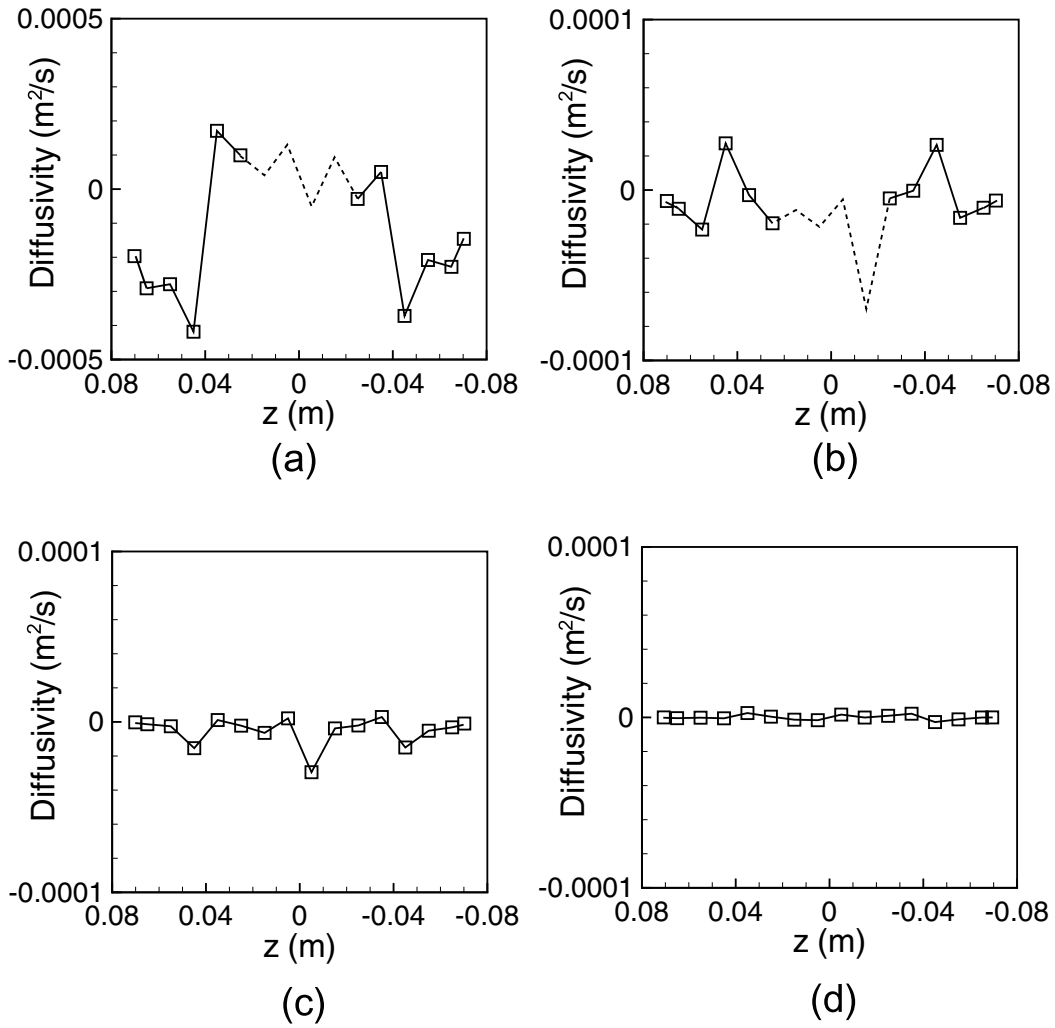


Figure 4.10. The variance of generalized axial diffusivity with the development of axial segregation along the axial length over four different time periods: (a) initial segregation (0-1 rotation); (b) intermediate segregation (4-5 rotation); (c) intermediate segregation (19-22 rotations); (d) full segregation (47-50 rotations).

particles from region 3 to region 2 leaving a band rich in large particles in region 3. The process continues forming more bands in the system and eventually achieving alternating segregation bands in the entire tumbler.

It is helpful to consider how the axial flow and particle number densities combine to bring about the axial banding. Figure 4.13 shows the axial velocity of the mixture, number density field of small particles and large particles, and the axial particle flux (*particles/m<sup>2</sup>s*) of both small and large particles on the same cross section at  $z = -0.065m$ , which is averaged over 0 – 1 rotation. The axial velocity of the mixture shown in figure 4.13(a) approximately represents the axial velocity of both small and large particles since they have nearly identical velocities. The axial velocity field shown in figure 4.13(a) is almost symmetric about the midpoint of the flowing layer ( $x = 0m$ ). However, the distribution of small and large particles at this cross section differs due to radial segregation as indicated in figures 4.13(b) and (c). As a result, the axial flow rate of small particles away from the endwall in the upstream portion ( $q_s > 0$ ) is larger than the flow rate toward the endwall in the downstream portion ( $q_s < 0$ ), as shown in figure 4.13(d). Thus, small particles are conveyed away from the endwall. The opposite is true for large particles as shown in figure 4.13(e), so large particles accumulate near the endwall. This non-uniform distribution with high axial velocity and high concentration of large particles near the bottom end of the flowing layer results in the higher ratio of the axial flow rate of small particles in the upstream portion, as indicated in figure 4.11. Thus, in the upstream portion of the flowing layer where the particles are mixed, both small and large particles move away from the endwall as shown in figure 4.4. Because of radial segregation the smaller particles percolate to the lower part of the flowing layer

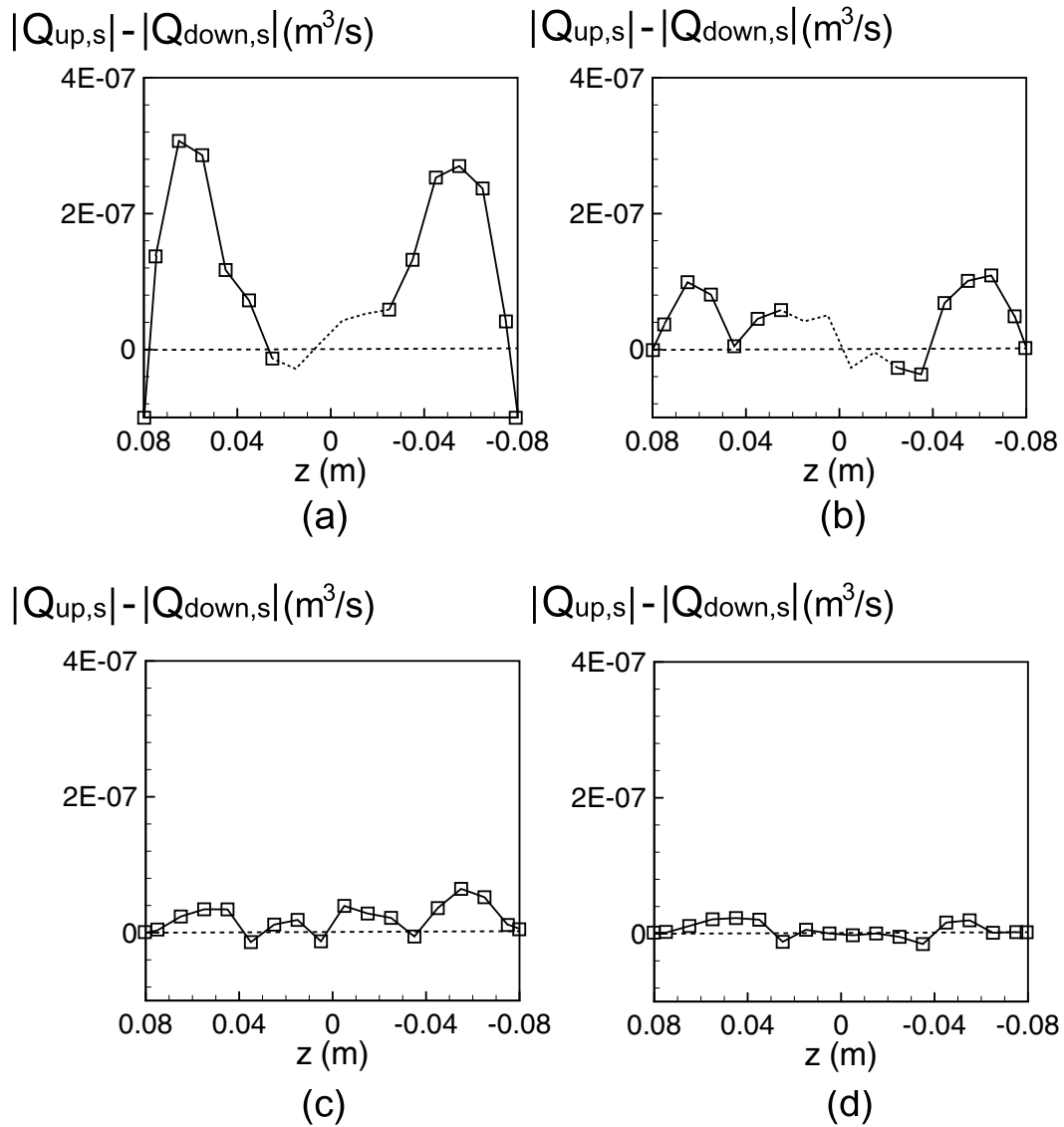


Figure 4.11. The magnitude difference of the axial flow rate of small particles in the upstream and downstream portions,  $|Q_{up,s}| - |Q_{down,s}|$ , along the axial length over four different time periods: (a) initial segregation (0-1 rotation); (b) intermediate segregation (4-5 rotation); (c) intermediate segregation (19-22 rotations); (d) full segregation (47-50 rotations). The dashed lines with 0 magnitude is used for reference.

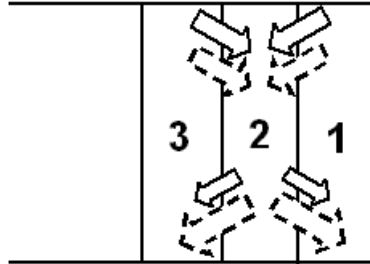


Figure 4.12. Illustration of onset of axial segregation in the system. Solid arrows: axial flow of small particles; dashed arrows: axial flow of large particles.

where the axial velocity back toward the endwall is less, while the large particles in the top of the layer are in a region of higher axial velocity back toward the endwall. The net result is that small particles carried from band 1 into band 2 in figure 4.12 are less likely to return to band 1, whereas large particles are more likely to return resulting in steadily progressing segregation.

From the above analysis, the non-uniformity of the axial velocity field and the particle concentration distribution are two key aspects related to the appearance of axial segregation, which is also discussed in Appendix A. It is not difficult to explain why the axial segregation only occurs when the size ratio of two species is large enough (Bielenberg *et al.*, 2007): radial segregation is a necessary precursor to axial segregation. Weak radial segregation does not carry small and large particles into different axial flow regions, so axial segregation occurs very slowly, if at all.

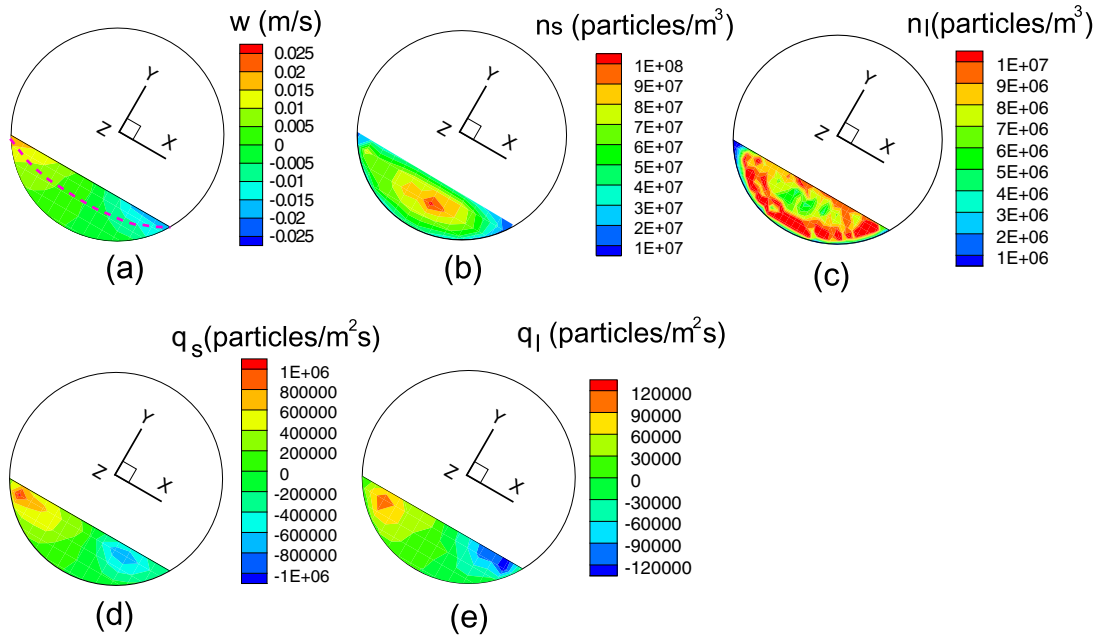


Figure 4.13. Illustration of imbalance distribution of the axial flow rate of small and large particles in upstream and downstream portions in the cross section at  $z = -0.065\text{m}$  averaged in  $0 - 1$  rotation: (a) axial velocity field of the mixture (purple curve indicates the boundary of the flowing layer at this cross section); (b) number density of small particles ( $\text{particles}/\text{m}^3$ ); (c) number density of large particles ( $\text{particles}/\text{m}^3$ ); (d) axial flux field of small particles; (e) axial flux field of large particles.

#### 4.6. Axial Segregation without Endwalls

The role of the endwalls is clear if we simulate the same system with periodic boundary conditions instead of two endwalls, thus eliminating the axial flow from the frictional endwalls. The result over 200 rotations is shown in figure 4.14. Compared to the frictional endwall case (figure 4.1), the magnitude of the concentration fluctuations remain very small and no pronounced segregation bands appear in the system even after 200 rotations.

The positions where local extreme concentrations occur come and go over time. None of them grow into segregation bands.

When the rotational speed is increased from  $\omega = 3.14 \text{ radians/s}$  to  $\omega = 6.28 \text{ radians/s}$ , some local extremes of concentration gradually evolve into segregation bands within 50 rotations, as shown in figure 4.15. However, not all concentration fluctuations develop into segregation bands, and the final segregation bands only originate from a subset of the early concentration fluctuations (those around  $z = -0.065m$  and  $z = 0$  in figure 4.15(b)). Comparing figures 4.14 and 4.15, it appears that for the same magnitude of the concentration fluctuations, a large rotational speed promotes band formation while a small rotational speed does not. This is consistent with experimental observations (Hill & Kakalios, 1994) that axial segregation only occurs at higher rotational speeds and segregated bands tend to resolve to well-mixed state at lower rotational speeds.

Slices at different axial positions at two representative times (after 10 and 50 rotations) are shown in figure 4.16. The radial segregation exists for the entire course of axial segregation with a core of small particles extending through large and small particle bands at  $z = -0.065m$  and  $z = 0.015m$ , respectively. Like the case with endwalls, the small particle bands are relatively pure, whereas large particle bands retain a core of small particles. Between bands, the particles are somewhat mixed, though the small particle core is evident. Snapshots of dynamic angles of repose of bands of small ( $z = 0.015m$ ) and large ( $z = -0.065m$ ) particles after 50 rotations are compared in figure 4.17. Again, the band of large particles has a higher dynamic angle of repose than the band of small particles.

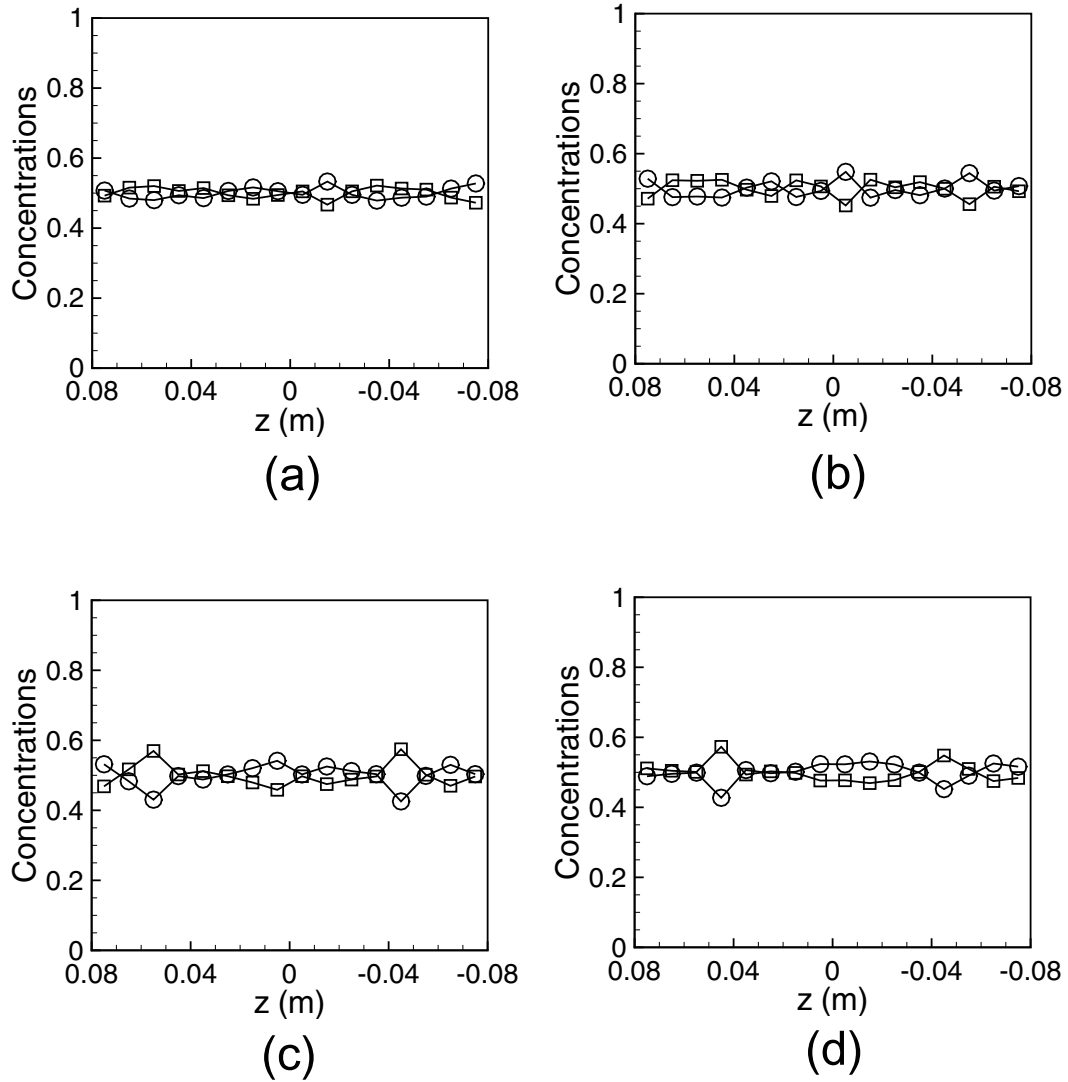


Figure 4.14. Evolution of the cross-sectionally averaged species concentration along the axial length at different times for the periodic boundary conditions with  $\omega = 3.14 \text{ radians/s}$ : (a) after 5 rotations; (b) after 10 rotations; (c) after 50 rotations; (d) after 200 rotations.  $\square$ , concentration of small particles;  $\circ$ , concentration of large particles.

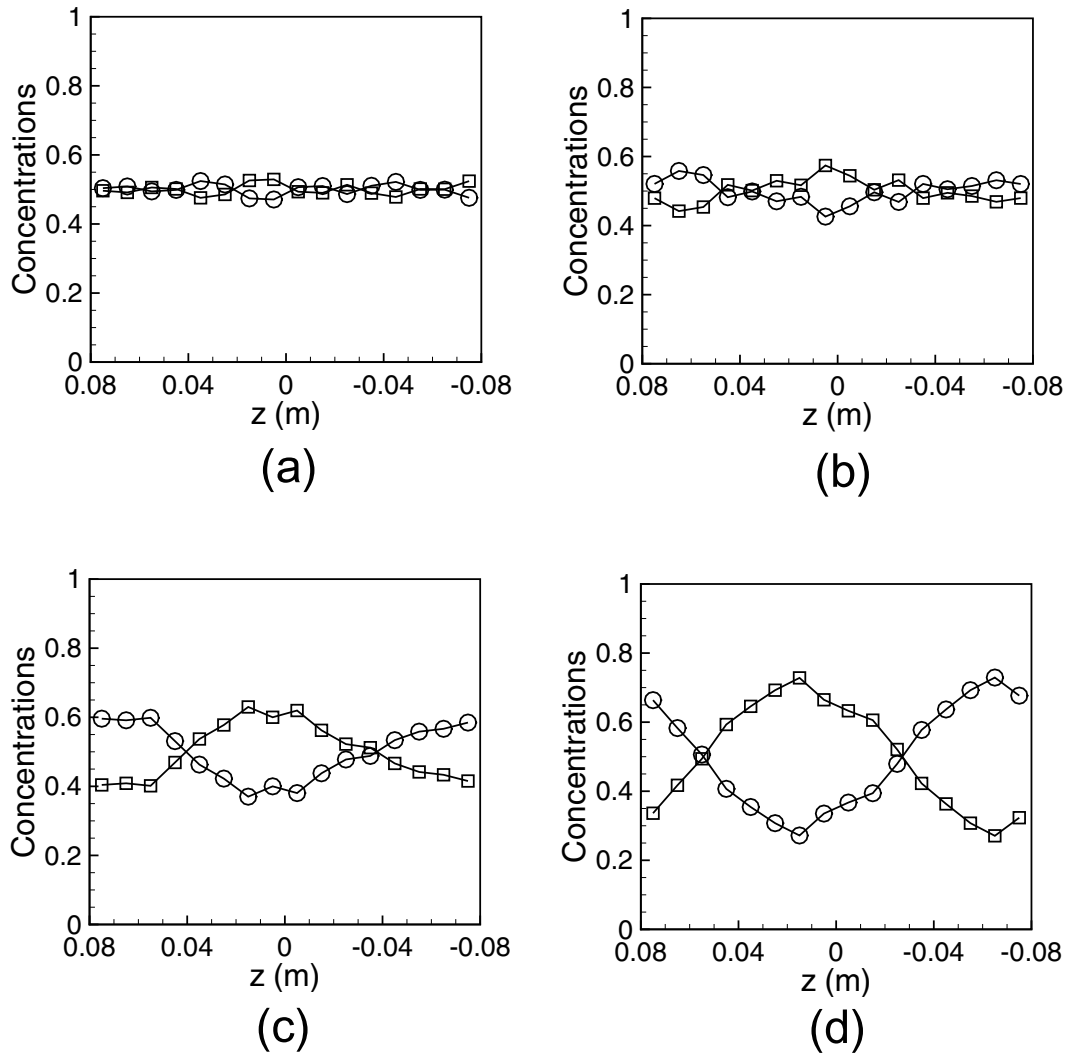
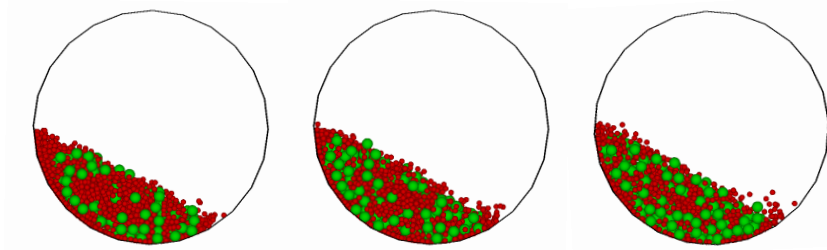


Figure 4.15. Evolution of the cross-sectionally averaged species concentrations along the axial length at different times for the periodic boundary condition with  $\omega = 6.28 \text{ radians/s}$ : (a) after 1 rotations; (b) after 5 rotations; (c) after 10 rotations; (d) after 50 rotations.  $\square$ , concentration of small particles;  $\circ$ , concentration of large particles.

After 10 rotations



After 50 rotations

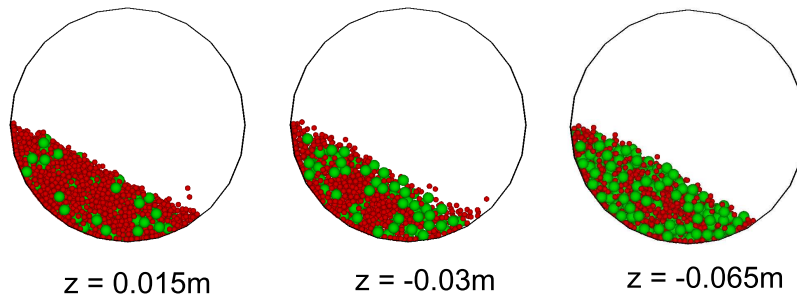


Figure 4.16. Snapshots of slices at different axial positions at two times: after 10 and 50 rotations (full axial segregation) for the periodic boundary conditions with  $\omega = 6.28 \text{ radians/s}$ .

The averaged axial velocity fields over 49 – 50 rotations on the free surface ( $y = -0.02m$ ) and a subsurface at  $y = -0.025m$  are shown in figure 4.18. It is evident that consistent with the results for the case with endwalls in figure 4.4, axial flow exists between segregation bands for the case of periodic boundary condition. Again, the axial flow is from the band of large particles to the adjacent band of small particles in the upstream portion of the flowing layer and back to the band of large particles in the downstream portion. Considering the concentration profiles at this time (figure 4.15(d)), the straight streamtraces always occur at the centers of the segregation bands (around  $z = -0.065m$  and  $z = 0.015m$ ) and the largest axial flows occur at the interface between bands (around  $z = -0.03m$  and  $z = 0.06m$ ). The boundary of the flowing layer at the band of small

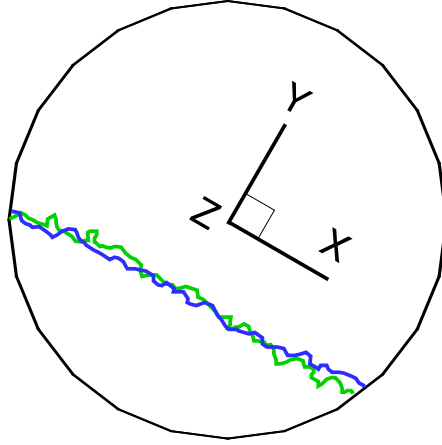


Figure 4.17. Difference of dynamic angles of repose of two cross sections after 50 rotations for the periodic boundary conditions with  $\omega = 6.28 \text{ radians/s}$ : blue curve, outline of the particle surface around the center of the band of small particles ( $z = 0.015m$ ) and green, outline of the particle surface around the center of the band of large particles ( $z = -0.065m$ ).

particles (around  $z = 0.015m$ ) is also wider than that of the band of large particles (around  $z = -0.065m$ ), indicating that the flowing layer is deeper here. This is not surprising given that particles are flowing into this band from adjacent bands at the upstream portion, and mass conservation requires that all particles pass through the flowing layer.

#### 4.7. Conclusions

Through a detailed computational study of the segregation of a mixture of particles having different sizes, we have examined the details of axial segregation in a long tumbler. Although different angles of repose between segregated bands are observed, it is the axial flow that drives the axial segregation. Friction at the endwalls generates axial flow due to mass conservation. The two particle species move in the same direction with almost

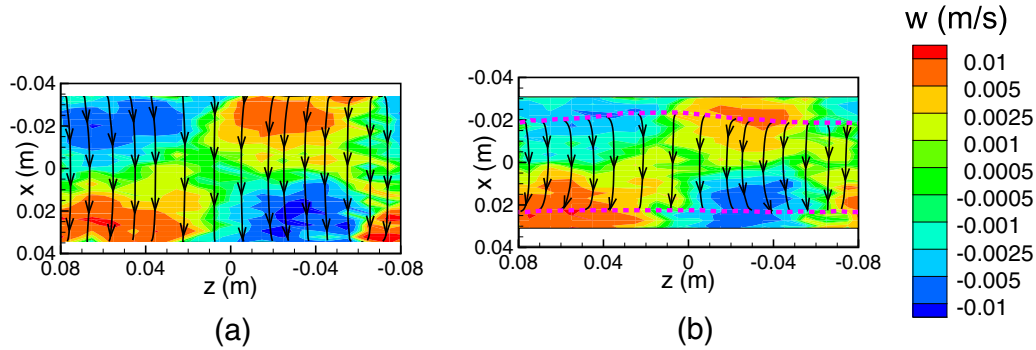


Figure 4.18. The velocity field over 49-50 rotations for the periodic boundary conditions with  $\omega = 6.28 \text{ radians/s}$  on: (a) free surface at  $y = -0.02m$ ; (b) below the surface at  $y = -0.025m$ . Black curves are streamtraces from the integration of streamwise velocity ( $u$ ) and axial velocity ( $w$ ). Color contours represent the levels of axial velocity ( $w$ ); purple curve at  $y = -0.025m$  represents the boundary of the flowing layer.

identical magnitude everywhere in the system: all particles flow from the bands of large particles into the bands of small particles in the upstream portion of the flowing layer and then flow back in the downstream portion.

The axial flow rates of the mixture in the upstream and downstream portions are balanced on every cross section. But the non-uniform distribution of axial velocity and species concentration on the cross section introduces unbalanced distribution of axial flow rate of individual species in the upstream and downstream portion: small and large particles flow away from the endwall in the upstream portion, but large particles tend to flow back toward the endwall more than small particles in the downstream portion because radial segregation has carried small particles deeper into the flowing layer where the axial velocity is smaller. As bands develop, these results are consistent with the experimental observations that the species concentration is in phase with the dynamic angle of repose.

This axial flow is approximately proportional to the concentration gradient. The differential transport of small and large particles in a cross-sectional slice appears like a negative diffusivity, justifying models for axial segregation as a phase transition characterized by a governing equation with a negative diffusivity (Hill & Kakalios, 1994, 1995; Savage, 1993; Zik *et al.*, 1994; Aranson & Tsimring, 1999; Aranson *et al.*, 1999).

Many open questions remain, including: (1) a better understanding of the axial velocity field from the frictional endwalls and the different angles of repose between adjacent bands, and the resulting concentration gradient; (2) the connection between radial segregation and axial segregation; (3) the nature of band coarsening and traveling waves (Choo *et al.*, 1998; Fiedor & Ottino, 2003); (4) the influence of axial flow from other shapes of endwalls or sidewalls on the axial segregation, for example, axial segregation in spherical tumblers (Gilchrist & Ottino, 2003*a*; Chen *et al.*, 2008*a*).

## CHAPTER 5

**Inversion of Band Patterns in Spherical Tumblers**

**Chapter Summary:** Just as axial bands form in long cylindrical tumblers for bi-disperse granular mixtures, similar bands occur in spherical tumblers: one at each pole and one at the equator. For low fill levels, large particles are at the equator with small particles at the poles; for high fill levels, the opposite occurs. Segregation is robust, occurring for many experimental conditions, though the fill level at which the transition occurs depends on particle size and rotational speed. Discrete element method simulations produce surface patterns that are identical to the experiments and reveal the internal segregation structures. Particle trajectories indicates that small particles flow further toward the poles than large particles in the upstream portion of the flowing layer for low fill levels leading to a band of small particles at each pole. The opposite occurs for high fill levels, though the deviation between the paths for the small and large particles is smaller, resulting in slower segregation. [This work in a slightly different form has been submitted to Physical Review Letters.]

**5.1. Introduction**

From the discussion in the last chapter and previous research it is evident that the axial flow near the endwalls is important in initializing the axial segregation in long rotating cylindrical tumblers (Hill & Kakalios, 1994; Fiedor & Ottino, 2003; Juarez *et al.*, 2008). The axial flow in cylindrical tumblers is generated at the flat, frictional endwalls, leading

us to consider the axial segregation in tumblers with other boundary shapes, for example spherical tumblers, which are discussed in this chapter. Axial segregation in spherical tumblers, though only considered in one other study (Gilchrist & Ottino, 2003*b*), offers an alternative approach to study the onset mechanism of granular axial segregation with different endwall conditions.

## 5.2. Experimental Results

We consider bi-disperse spherical glass particles in a clear acrylic spherical container with diameter  $D = 14\text{cm}$ . Three parameters were varied: 1) Particle sizes:  $1\text{mm} + 2\text{mm}$ ,  $1\text{mm} + 3\text{mm}$ ,  $1\text{mm} + 4\text{mm}$ , and  $2\text{mm} + 4\text{mm}$  (for all cases small particles are black and large particles are clear); 2) Rotation rates: 2, 5, 10, 20, and 30 *rpm*; and 3) Fill levels: 20 to 60% by volume. In all cases, small and large particles make up equal volumes. Before loading the particles, the spherical tumbler was sprayed with an anti-static aerosol (McMaster-Carr, Chicago, IL 60680). Because bi-disperse particle mixtures pack more densely than mono-disperse particles, several iterations of adding equal amounts of large and small particles were necessary to reach the desired fill level. All experiments were started from a well mixed initial condition. The axial segregation always begins within the first several revolutions, but it approaches a stable surface segregation pattern at varying rates. Images were obtained at 102 revolutions, which is large enough to assure a steady surface segregation pattern. In all cases where axial segregation was observed, the segregation pattern formation was consistent from the beginning of the experiment until steady segregated state was reached; no pattern changes were observed during the development of the axial segregation.

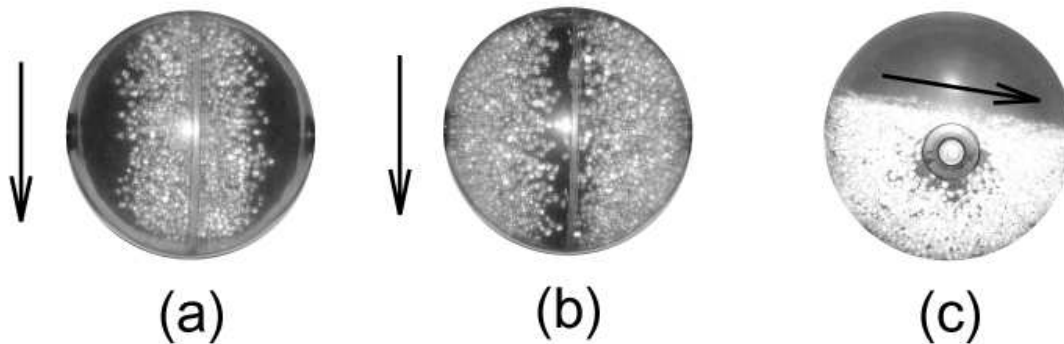


Figure 5.1. Two representative surface segregation patterns occur for  $1\text{mm}$  black and  $4\text{mm}$  clear glass beads rotated at  $20\text{ rpm}$  about a horizontal axis. The narrow vertical stripe on the surface of the clear tumbler is the seam between the two halves of the spherical tumbler. (a) top view: *SLS*, 30% full; (b) top view: *LSL*, 60% full; (c) side view: 60% full. Flow direction is indicated by arrows. The small circle at the pole region is the transparent suction cup bonded to the tumbler surface for connection to a shaft for rotation.

In contrast to previous work (Gilchrist & Ottino, 2003*b*), two distinct segregation patterns appear at the top free surface depending on the fill level, as shown in figure 5.1. The Small-Large-Small (“*SLS*”) pattern in figure 5.1(a), which is characterized by a center band of large particles bounded by outer bands of small particles, occurs at low fill levels. The reverse pattern, Large-Small-Large (“*LSL*”) in figure 5.1(b) and the work of Gilchrist & Ottino (2003*b*), occurs at high fill levels. The *SLS* pattern develops within 5 – 10 rotations whereas the *LSL* pattern often requires 20 or more rotations to become clearly evident. In all cases, the two species of particles also segregate radially with the small particles at the radial core. In fact, the axial segregation pattern shown in figure 5.1(b) has an extended radial core of small particles that appears at the pole regions below large particles, as shown in figure 5.1(c).

The axial segregation patterns and the transition between them depends on the fill level, the particle size ratio, and the absolute size of particles, as shown in figure 5.2 for rotation at 20 *rpm*. Patterns above the bold line are *SLS*, and patterns below the bold line are *LSL*. The transition between the two segregation patterns is gradual as the fill level is changed. For fill levels just below the transition, a weak *SLS* pattern is observed; just above the transition a weak *LSL* pattern occurs. The transition fill level increases with the size of the large particles when the size of the small particles is fixed, comparing the left three columns of figure 5.2. For the same size ratio, the 2*mm*+4*mm* mixture has a much higher transition fill level (between 50% and 60%) than the 1*mm*+2*mm* mixture (between 20% and 30%), indicating that both the ratio of particle sizes and the particle sizes themselves affect the transition fill level.

For every particle mixture and fill level, the rotation rate was varied from 2 *rpm* to 30 *rpm*. For most cases increasing the rotation rate brings on axial segregation more quickly and enhances the degree of segregation, but does not affect the surface segregation pattern, as shown in figure 5.3(a). But for high fill levels above 50% for 1*mm*+4*mm* and 2*mm*+4*mm* mixtures, the surface segregation pattern changes from *LSL* to *SLS* with increasing rotation rate. In figure 5.3(b), for rotation rates of 2 *rpm* and 5 *rpm*, segregation is not readily apparent, although through closer inspection indicates a weak *LSL* pattern away from the poles with both the large and small bands exhibiting substantial contamination by the particles of the other size. As the rotation rate increases from 5 to 10 *rpm* the center band of small particles becomes clearer and less contaminated by large particles. This is consistent with results for axial segregation in cylindrical tumblers: the segregation is weak at low rotation rates and strong at high rotation rates (Hill &

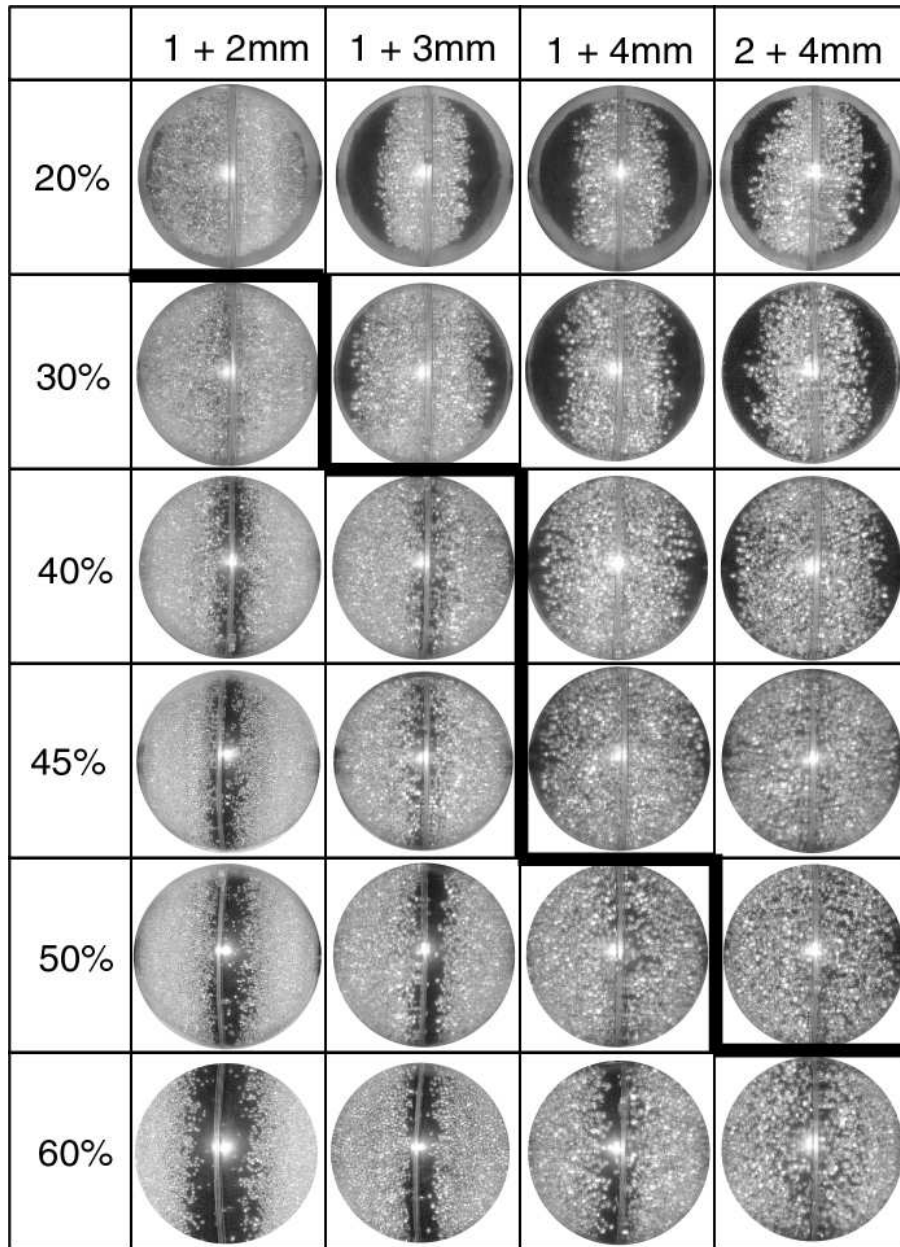


Figure 5.2. Two axial segregation patterns, as viewed looking down on the free surface, depend on the fill level, the particle size ratio, and the absolute particle sizes. The rotation rate is 20 *rpm* about a horizontal axis in the figure. Flow is from top to bottom. Bold lines mark the transition from *SLS* to *LSL*.

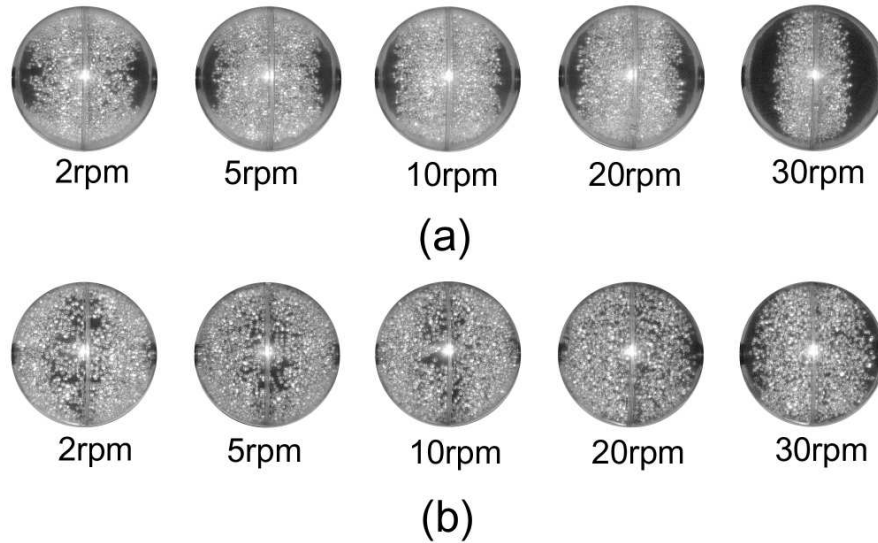


Figure 5.3. (a) The degree of axial segregation depends on the rotation rate for the  $1mm+3mm$  mixture at 30% full, but is always *SLS*. (b) The segregation pattern changes from *LSL* to *SLS* for the  $2mm+4mm$  mixture at 50% full as the rotation rate increases from 10 *rpm* to 20 *rpm*.

Kakalios, 1994, 1995). However, the *LSL* segregation pattern changes to a *SLS* pattern as the rotation rate increases from 10 *rpm* to 20 *rpm* in this case. At 30 *rpm* the *SLS* segregation pattern always results for all particle mixtures and fill levels, although the segregation is very weak in some cases. This may occur because the free surface is no longer flat at 30 *rpm*. For all cases tested, only the transition from *LSL* to *SLS* occurred with increasing rotation rate; no reverse transition from *SLS* to *LSL* was observed.

### 5.3. Numerical Simulation Results

To investigate details of the flow leading to the two segregation patterns, we simulated the flow of the  $2mm+4mm$  mixture in a  $D = 14cm$  sphere using the discrete element

method (Cundall & Stack, 1979). The liner-spring dashpot force model was used here to calculate the normal force between two contacting particles (see Ristow (2000); Chen *et al.* (2008b) for details.) To save computational time, a tangential force model without a memory effect (Rapaport, 2002; Taberlet *et al.*, 2006), which was also introduced in chapter 2, was used in the simulation. Simulation with this tangential force model produces almost the same macroscopic segregation pattern as the memory-effect model (Chen *et al.*, 2008b). Material properties of glass were used in the simulation ( $2500\text{kg}/\text{m}^3$ ; 0.97 restitution coefficient), and particles were randomly mixed initially. The coordinate system still sets the origin at the center of the tumbler with the  $x$  axis along the stream-wise direction, the  $y$  axis normal to the free surface, and the  $z$  axis along the tumbler rotational axis, as shown in figure.1.1.

The DEM successfully reproduces the two experimental segregation patterns at appropriate fill levels, as shown in figure 5.4 after 100 rotations for rotation at 20 *rpm*, when the pattern is fully developed. The *SLS* pattern in figure 5.4(a) segregates much faster and is more distinct than the *LSL* pattern in figure 5.4(b), just as the case in the experiments for  $2\text{mm}+4\text{mm}$  particles in figure 5.2. Figure 5.4(c) shows the radial core extending at the pole regions, which was also evident experimentally (figure 5.1(c)). The internal structure of the fully developed segregation is shown by several representative slices at different axial positions in figure 5.5. It is clear that similar to the axial segregation in cylindrical tumblers (Hill *et al.*, 1997b; Jain *et al.*, 2001; Arndt *et al.*, 2005), bands of small particles in spherical tumblers result from the expansion of the radial core of small particles to the free surface. For the *SLS* system, the radial core of small particles extends the length of the tumbler parallel to the axis of the rotation, and it is relatively

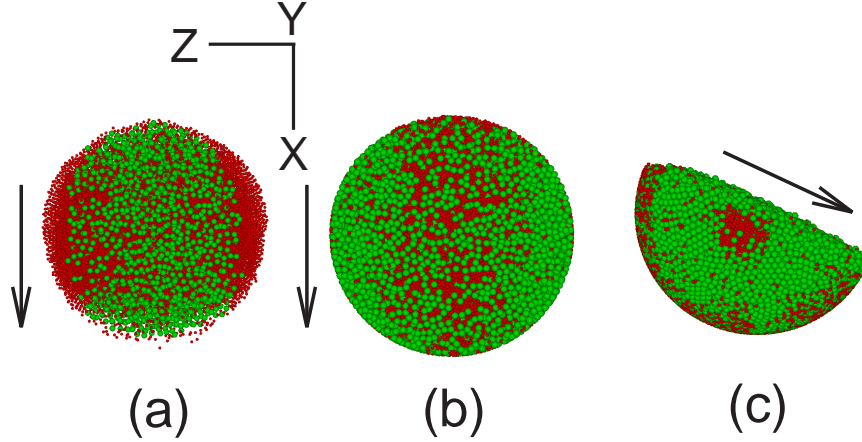


Figure 5.4. Segregation patterns for the simulation after 100 rotations at 20 *rpm* for 2*mm* and 4*mm* particles in a 14cm diameter tumbler: (a) *SLS* pattern for 20% full; (b) *LSL* pattern for 60% full; (c) pole region of small particles in *LSL*.

pure. In the *LSL* system, the core of small particles also extends parallel to the axis of rotation, but it is contaminated by large particles. The core of small particles dominates at the axial center of the tumbler ( $z = 0$ ) reaching the free surface, though percolation results in some large particles also appearing at the flowing layer surface.

To show the internal structure of the fully developed segregation more clearly, the local concentration of small particles,  $C_s(x, y, z)$ , was calculated over the computational domain (using 20 bins in each dimension) over  $2/3$  tumbler rotation. From this, the core of small particles can be displayed in terms of iso-surfaces of small particles concentration above a specified level. Likewise, the portion occupied mostly by large particles can be displayed as the iso-surface with  $C_s(x, y, z)$  less than a specified level. As shown in figure 5.6(a) for the *SLS* pattern, the core of small particles extends along the axis of

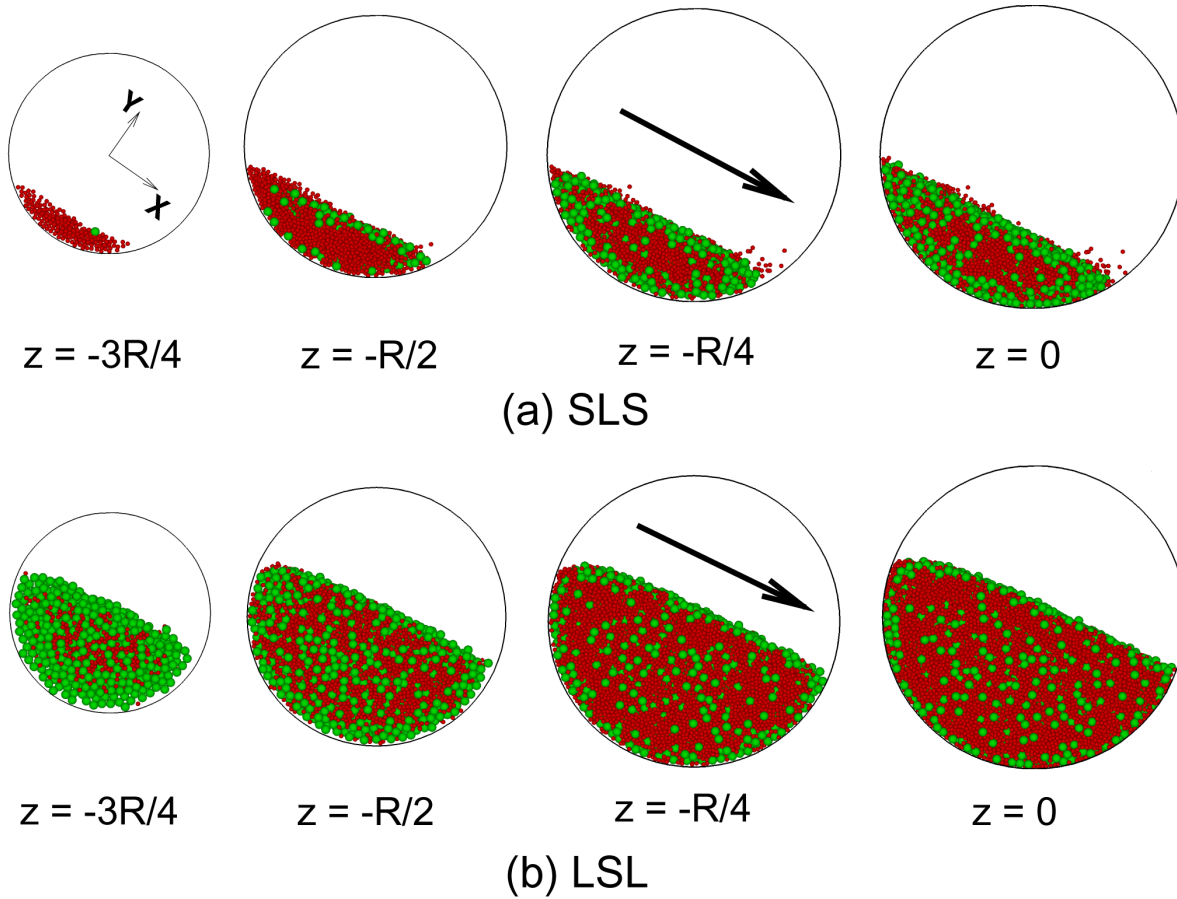


Figure 5.5. Snapshots of slices at different axial positions after the segregation has reached steady state: (a) *SLS*; (b) *LSL*. Flow is indicated by arrows.

rotation, but is quite narrow near the center of the tumbler and fills the volume near the poles. The volume of large particles surrounds the narrowed core of small particles at the equator (figure 5.6(b)). For the *LSL* pattern the core of small particles is much larger at the center of the tumbler (figure 5.6(c)). The core narrows near the poles where it is

buried beneath the large particles. The volume of larger particles surrounds the smaller particles except at the equator and poles (figure 5.6(d)).

The evolution of the segregation is most readily considered in terms of the concentration of particles averaged spatially over the transverse cross-sections,  $C_s(z)$ , along the axis of rotation (using 20 bins along the axis). The concentration of small particles averaged over  $2/3$  of a tumbler revolution is shown in figure 5.7 for several times during the simulation: initial segregation (the first  $2/3$  rotation of the tumbler after the flow is initialized), developing segregation ( $8/3 - 10/3$  rotations and  $20/3 - 22/3$  rotations), and the fully segregated state (after 100 rotations). For the *SLS* case, figure 5.7(a), the motion of small particles toward the poles quickly changes the axial distribution of particles near poles from the initial uniform concentration of 0.5 to 1.0 within the first  $2/3$  rotations. Within 8 rotations of the tumbler, the concentration distribution is nearly at the steady-state distribution, and the bands of small particles near the poles are quite pure. At the equator, the small particle concentration of 0.4 at steady-state represents the core of small particles surrounded by large particles. The situation is quite different for the *LSL* case, shown in figure 5.7(b). In this case, the time evolution of the segregation is much slower, not approaching steady-state until approximately 30 tumbler rotations (not shown). The high small particle concentration at the poles is due to the core of small particles extending along the entire length of the bed of particles at the axis of rotation right to the poles, as shown in figure 5.1(c) and figure 5.4(c). A short distance from the poles, the large particles dominate so the small particle concentration is quite small, corresponding to the neck in the small particle concentration in figure 5.6(c). Like the *SLS* pattern, the concentration near the equator is far from pure due to imperfect segregation

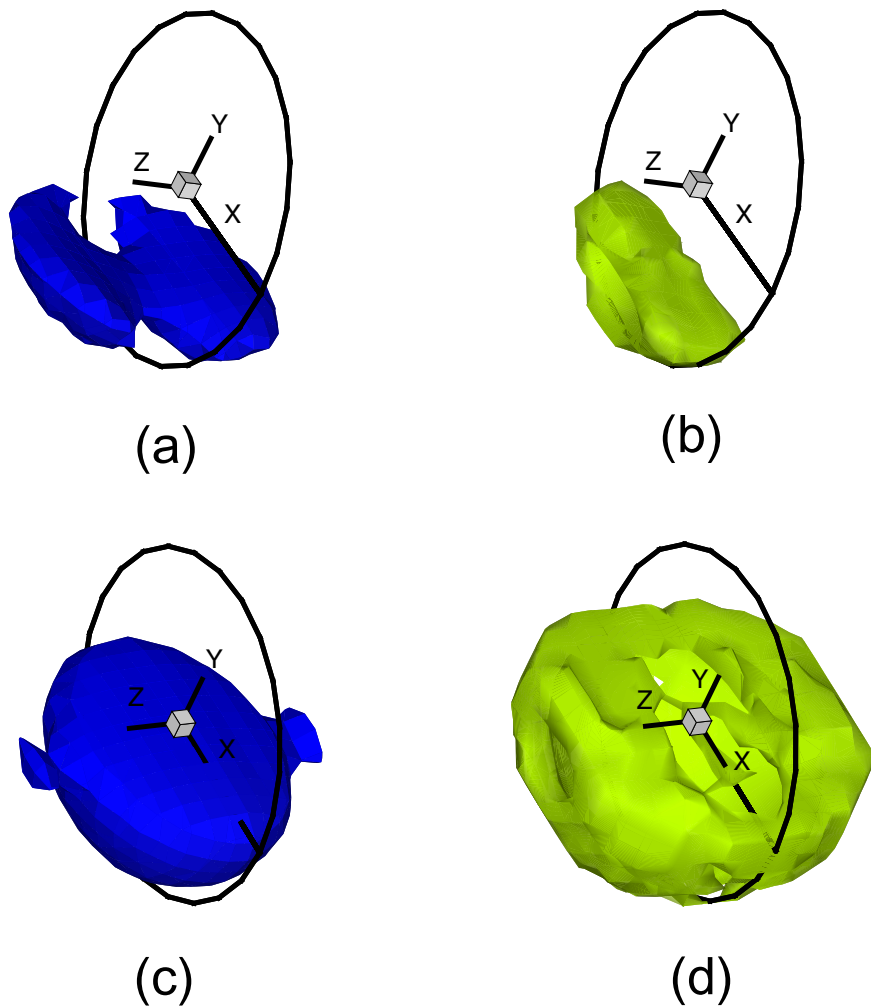


Figure 5.6. Structures of small and large particle volumes averaged over  $2/3$  rotations represented by the iso-surface where the concentration of small particles,  $C_s(x, y, z)$ , is above or below a specified level after the segregation has reached steady state: (a) Small particle volume for *SLS*,  $C_s(x, y, z) \geq 0.75$ ; (b) Large particle volume for *SLS*,  $C_s(x, y, z) \leq 0.3$ ; (c) Small particle volume for *LSL*,  $C_s(x, y, z) \geq 0.5$ ; (d) Large particle volume for *LSL*,  $C_s(x, y, z) \leq 0.3$ . The black circles mark the inner circumference of the spherical tumbler.

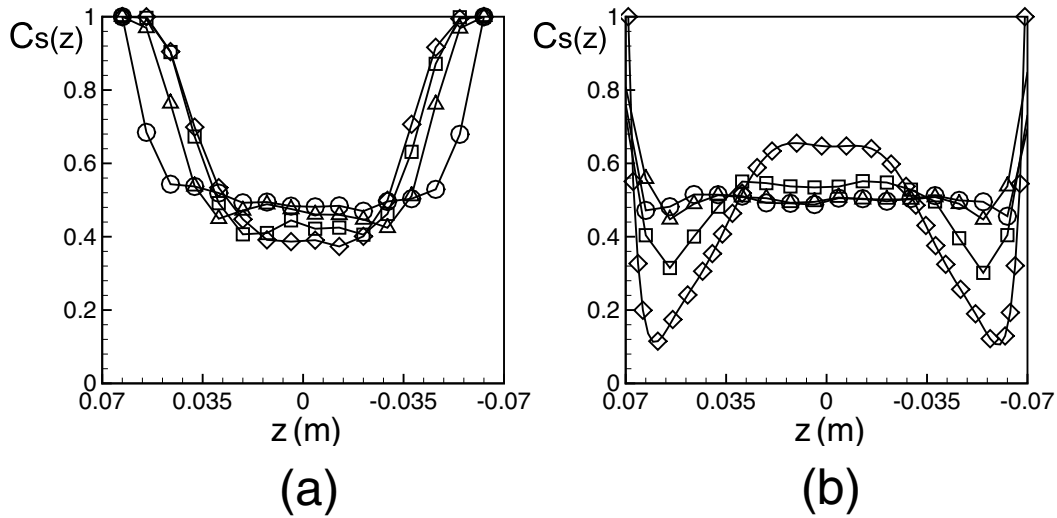


Figure 5.7. Evolution of the concentration of small particles in a transverse cross-section,  $C_s(z)$ , along the axial length for (a) *SLS* and (b) *LSL* patterns at different times:  $\circ$ , initial segregation (first  $2/3$  rotation);  $\triangle$ , ( $8/3$ - $10/3$  rotations);  $\square$ , ( $20/3$ - $22/3$  rotations);  $\diamond$ , full segregation (after 100 rotations).

(figure 5.5(b)). For both patterns, the axial segregation is initiated at the pole regions and propagates toward the equator.

Further insight into the evolution of the segregation can be obtained from streamtraces of the mixtures on the free surface and the axial velocity of individual species along the depth. The streamtraces are obtained from the integration of axial and streamwise velocity of all particles on the top free surface. It is clear that for *SLS* pattern (figure 5.8), the free surface flow pattern remains almost unchanged through the entire course of axial segregation: apparently due to the tumbler boundary geometry, the particles follow

the curved tumbler edge (“geometric effect”). This is because the surface particles flowing down the slope collide with the downstream tumbler boundary obliquely and are rebounded toward the center of the tumbler,  $z = 0$ , so the streamtraces curve toward the center in the downstream portion and toward the poles in the upstream portion to maintain mass conservation. The streamtraces near the center of tumbler are nearly straight due to symmetry. The axial velocity of the two individual species along the depth at two representative positions,  $z = -0.035m$ ,  $x = -0.035m$  (upstream) and  $z = -0.035m$ ,  $x = 0.035m$  (downstream) shows that during the entire course of axial segregation, small and large particles flow in the same direction but with slightly different magnitudes, which is consistent with the axial flow of particles of two species in cylindrical tumblers discussed in the last chapter. It is also clear that the direction of the internal axial flow is consistent with that on the free surface and the magnitude of axial flow decreases with the depth in the flowing layer.

The flow pattern of *LSL* is more complicated (figure 5.9). For the first  $2/3$  revolution, particles on the surface tend to follow the curved tumbler edge, although the curvature of the paths is less than in the *SLS* case, particularly at the downstream end of the streamtraces. But with the development of the segregation bands, the magnitude of axial flow of the surface particles decreases. This influence from the segregation bands may be associated with the larger dynamic angle of repose for the bands rich in large particles, as discussed in the last chapter. As illustrated in the last plot in figure 5.9, the sign of the axial flow changes with the depth. Again, for *LSL* pattern, small and large particles flow in the same direction and with nearly the same magnitude during the entire course of segregation.

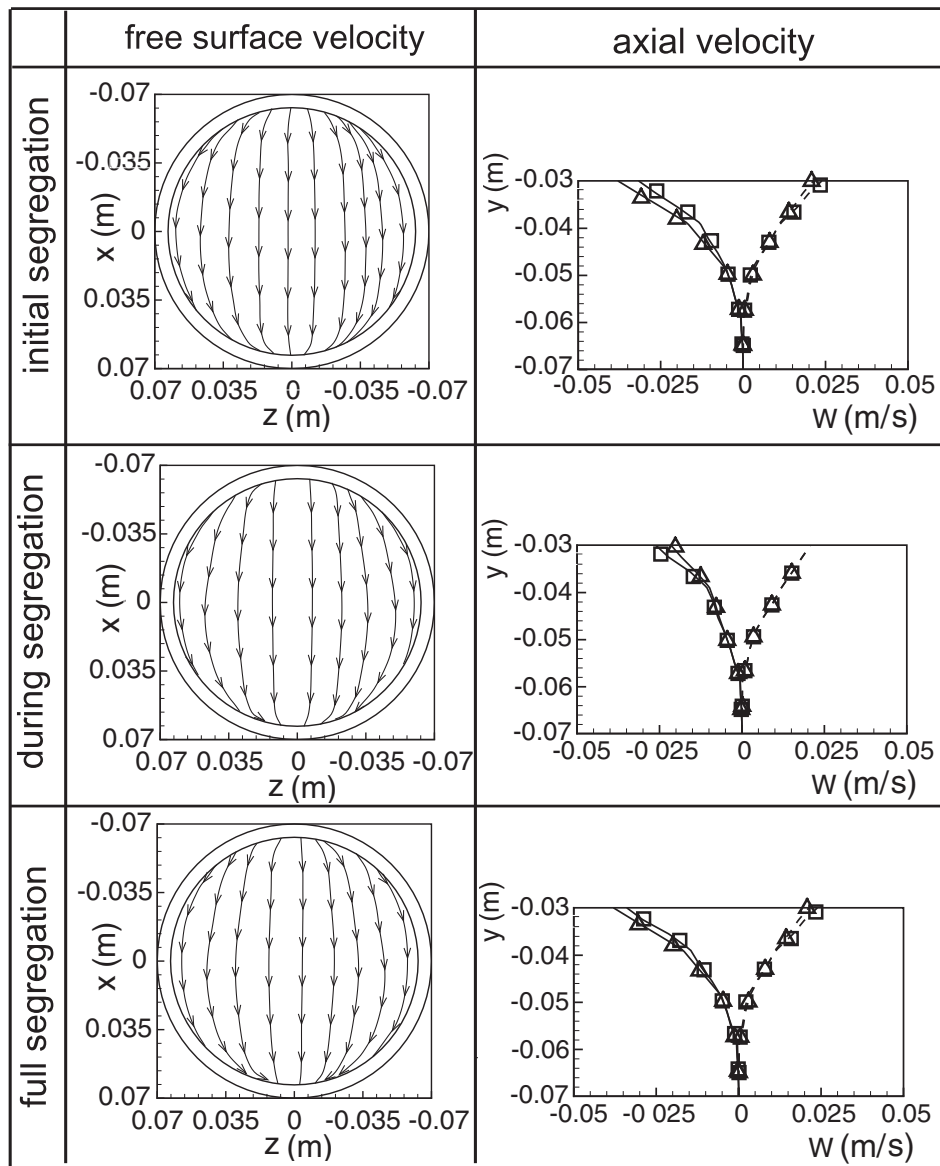


Figure 5.8. Evolution of the velocity field averaged from the flow of all particles on the free surface (inner circles show the edge of the top surface) for *SLS* (20% full) pattern and the axial velocity along the depth of individual species (small,  $\square$  and large,  $\Delta$ ) at  $z = -0.035m$ ,  $x = -0.035$  (solid line) and  $z = -0.035m$ ,  $x = 0.035m$  (dashed line) at different states: initial segregation (first 2/3 rotation); during segregation (8/3-10/3 rotation for *SLS* and 20/3-22/3 rotation for *LSL*); full segregation (after 100 rotations).

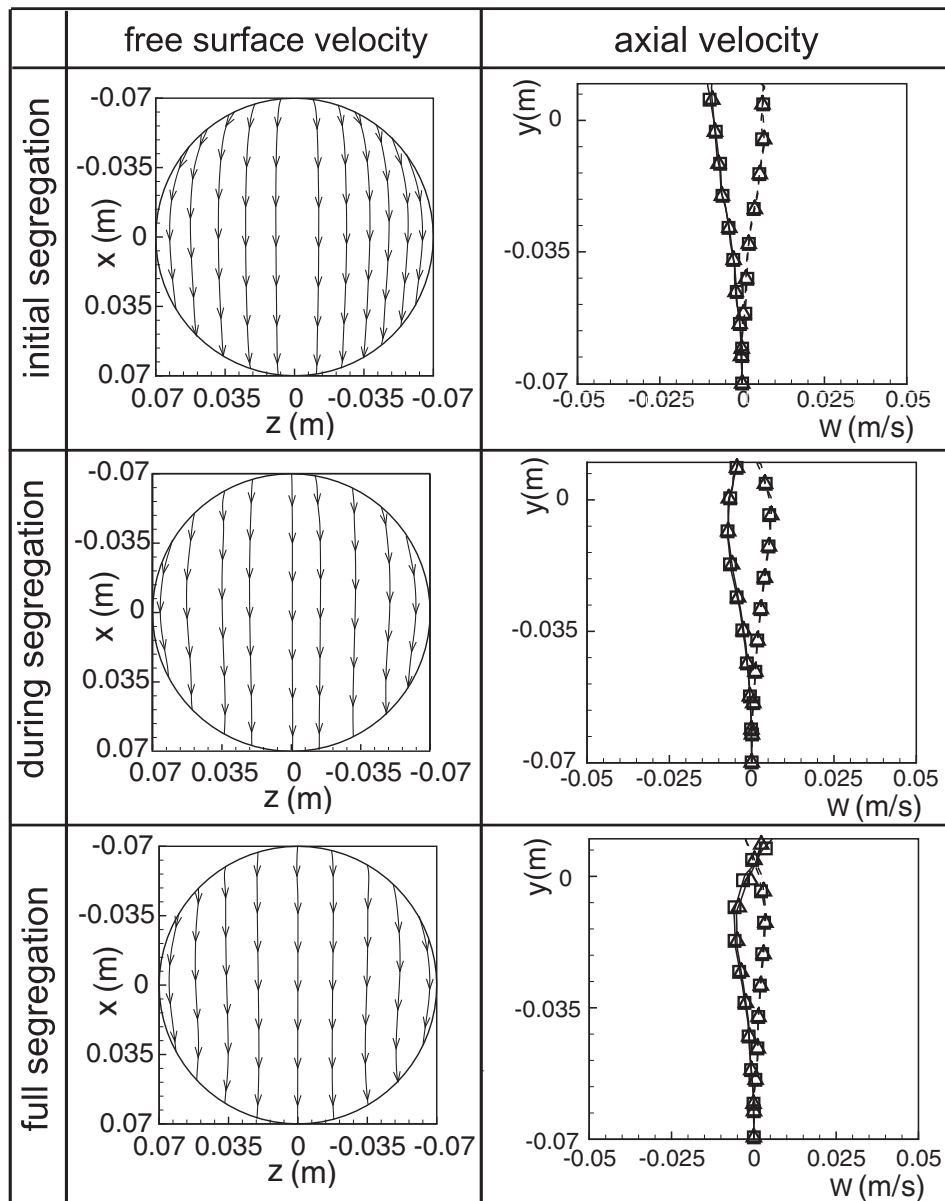


Figure 5.9. Evolution of the velocity field averaged from the flow of all particles on the free surface for *LSL* (60% full) pattern and the axial velocity along the depth of individual species (small,  $\square$  and large,  $\Delta$ ) at  $z = -0.035m$ ,  $x = -0.035$  (solid line) and  $z = -0.035m$ ,  $x = 0.035m$  (dashed line) at different states: initial segregation (first  $2/3$  rotation); during segregation ( $8/3$ - $10/3$  rotation for *SLS* and  $20/3$ - $22/3$  rotation for *LSL*); full segregation (after 100 rotations).

It is instructive to consider the paths of the small and large particles to better understand how the axial segregation pattern comes about. To do this, we tracked particles starting in two small regions near the upstream end of the flowing layer: region  $A$ , located on the surface of the flowing layer near where the boundary between bands of small and large particles eventually comes about in steady state; region  $B$ , which is half way between point  $A$  and the equator ( $z = 0$ ). The ensemble average particle paths for 20 – 150 particles are shown in figure 5.10.

During the initial rotations for the *SLS* pattern, both types of particles tend to drift toward the poles in the upstream portion of the particle path and back toward the equator in the downstream portion, but small particles travel further toward the poles, and do not return back as far toward the equator as large particles. The particle paths end where the particles stop flowing (on average) and are trapped in solid body rotation. The net result is that smaller particles are trapped further from the equator than where they start, and large particles are trapped closer to the equator, which produces bands of small particles closer to the poles, producing the *SLS* pattern. The trajectories of the small particles are shorter and those of the large particles are longer in *SLS*. This comes about because the small particles percolate through the larger ones in the bi-disperse case, thus falling out of the flowing layer sooner, while the large particles remain on the top surface and fall out later. The deviation of particle paths for two species persists through the entire course of axial segregation, but disappears in the final fully segregated state. At that point particles simply flow down the slope and return to their original axial position.

The situation is quite different for the *LSL* pattern. Initially, the paths for both particle types overlay each other with only a small degree of curvature toward the poles

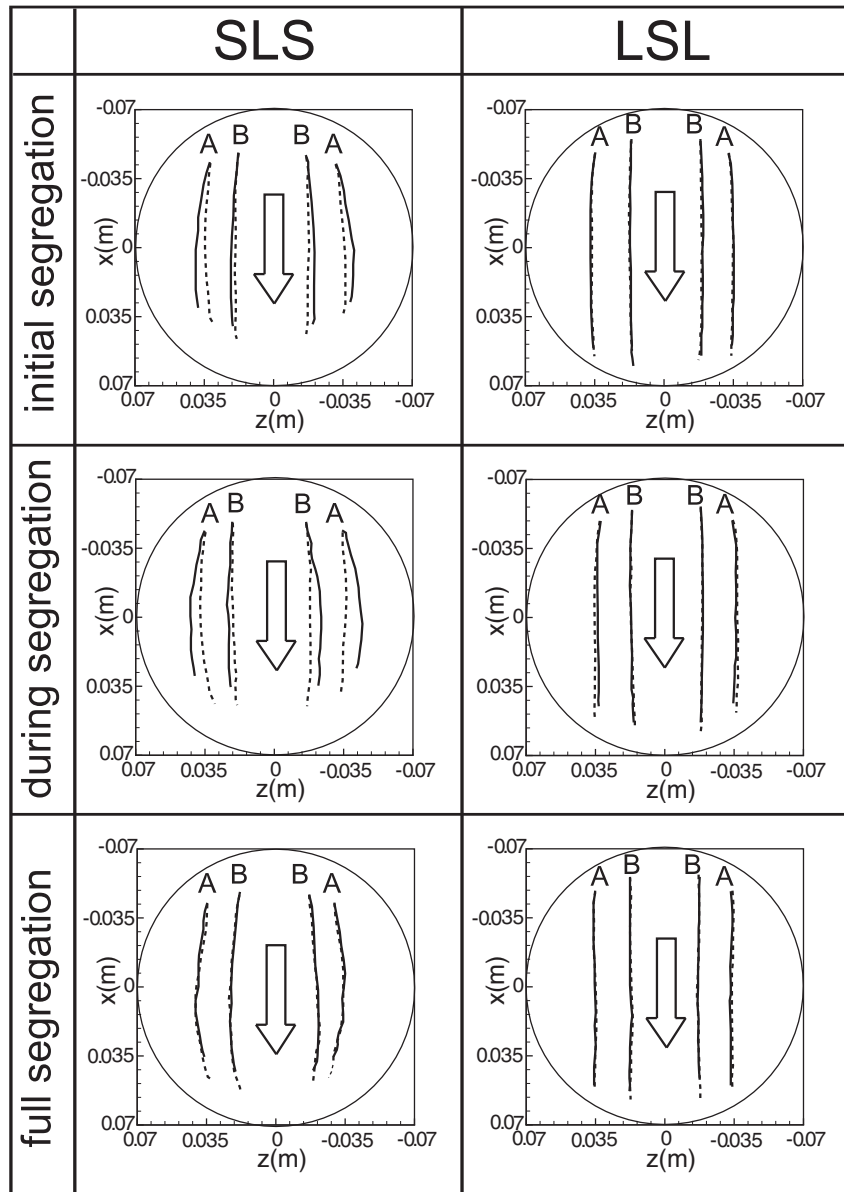


Figure 5.10. Trajectories of the 2mm (—) and 4mm (---) particles on the free surface for each pattern at three times in simulation: initial segregation (first 2/3 rotation); during segregation (8/3-10/3 rotations); and full segregation (after 100 rotations). *A* is a region at the steady-state boundary between the bands; *B* is halfway between point *A* and the equator. Flow is from top to bottom.

at the upstream end of the path. However, during the axial segregation, the large particles drift slightly toward the poles compared to the small particles, which is the reverse of the situation for the *SLS* pattern. Again, after the segregation reaches steady state the deviation between the paths of two species disappears. The deviations between the paths in the *LSL* case are small compared to those for *SLS*, so the rate at which segregation occurs for the *LSL* system is slower than that for the *SLS* system. For comparison,

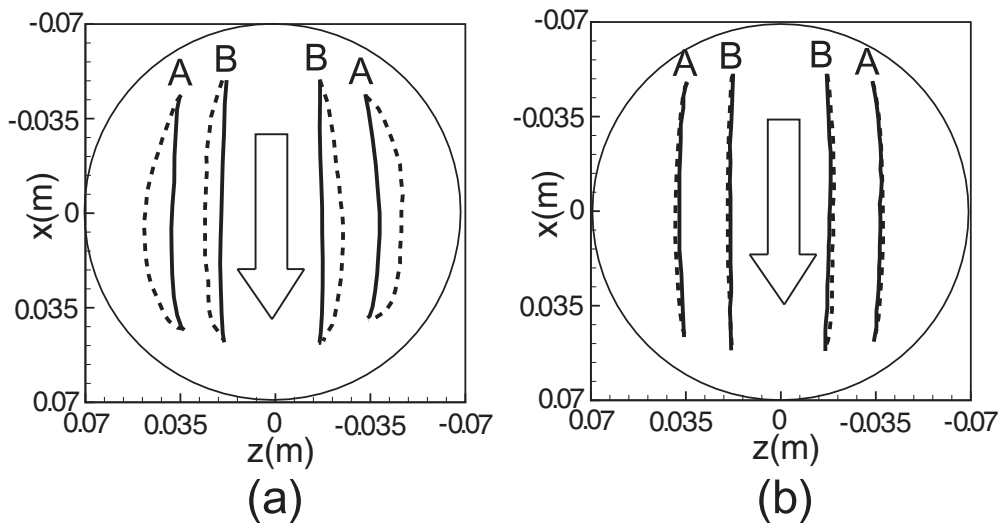


Figure 5.11. Trajectories of the 2mm (—) and 4mm (---) particles on the free surface for mono-disperse systems of small and large particles at (a) 20% full and (b) 60% full. Flow is from top to bottom.

figure 5.11 shows the flow of pure mono-disperse systems of small or large particles rotated under the same conditions as in figure 5.10. For the high fill level, the trajectories are similar for the mono-disperse case (figure 5.11(b)) and the bi-disperse case (figure 5.10), though for the mono-disperse case the particle trajectories return to their original axial

position at the end of their flight. However, for the low fill level, the trajectories of large particles always curve more toward the poles than those of small particles (figure 5.11(a)), which is the opposite of what occurs for the bi-disperse case. Simulations of mono-disperse particles in a smaller  $7\text{cm}$  diameter tumbler indicate that the curvature of the path is inversely related to the ratio of tumbler diameter to particle diameter. As this ratio decreases, the particle trajectories become more curved. Thus, larger particles have more curved paths than small particles for the same tumbler diameter for a mono-disperse system.

#### 5.4. Conclusions

What is not clear is how the presence of two particle species changes the trajectories of both species at low fill levels, but does not alter the trajectories much at high fill levels. Part of the answer lies in the observation that strongly curved particle paths are associated with low fill levels for both mono-disperse and bi-disperse cases. In particular, the angle between the surface of particles and the tumbler wall is always greater than  $90^\circ$  for fill levels below 50% and less than  $90^\circ$  for fill levels above 50%. At low fill levels particles stack up in a monolayer on the tumbler wall at the upstream end of the flowing layer due to the obtuse angle between the tumbler wall and flowing layer. For mono-disperse systems, the particles tend to fall out of the monolayer along the tumbler wall (toward the poles) resulting in a curved trajectory. Furthermore, due to the relative radii of curvature of the particles and the tumbler wall, larger particles arc further toward the poles than smaller particles leading to the situation in figure 5.11(a). For bi-disperse systems, both particle sizes tend to fall out of the monolayer toward the poles, but the small particles

percolate through the larger ones to collect near the poles first, thus directing larger particles toward the equator leading to the situation for *SLS* in figure 5.10. When the tumbler with bi-disperse particles is more than 50% full the monolayer does not occur due to the acute angle between the tumbler wall and the flowing layer, so the particle trajectories are nearly straight with a slightly greater tendency for larger particles to flow toward the poles (as in the mono-disperse case) leading to the situation for *LSL* in figure 5.10.

The axial segregation patterns in spherical tumblers are simpler and more stable than those in cylindrical tumblers, which allows the use of spherical tumblers as an alternative to study the onset mechanisms for granular axial segregation. While this work has isolated some aspects of the two forms of axial segregation in a spherical tumbler, many details are not understood, including the impact of tumbler size and particle size on the transition from *SLS* to *LSL* with changing fill levels and rotational speeds. Likewise the details of the driving force for axial segregation deserves further investigation, particularly the nature of the mono-layer on the tumbler wall at the upstream end of the flowing layer, which seems to initiate and drive the segregation.

## CHAPTER 6

**Outlook**

The general focus of this thesis is the use of numerical simulation techniques, coupled with experiments, to study the fundamental physics of flow, mixing, and segregation of granular materials, particularly the onset mechanism of axial segregation in cylindrical and spherical rotating tumblers. Discrete element method (DEM) is the main technique used in this work. DEM simulations give information for individual particles, including their positions and velocities at each time step. More importantly, it yields the continuum flow field in the system by averaging the flow of particles located in individual bins of the average mesh and makes it possible to study granular phenomena quantitatively rather than qualitatively. While many aspects of granular flow, mixing, and segregation have been investigated numerically using Discrete Element Method in this thesis, there are still many open questions. Here we give some recommendations for future work:

A natural extension of our work on axial segregation is the quantitative investigation of long-term behavior of band dynamics using the discrete element method. This, however, needs a much longer simulation time. Intriguing questions may include: how the flow field (surface and subsurface) of individual species changes during the course of band oscillation and merging; how adjacent bands interplay locally to make the number of bands in the system decreases with time during the course of bands merging; how the radial segregation core interplays with axial segregation bands during the band oscillation and merging. We investigated axial segregation due to particle size difference in this work

and there is a need to study segregation arising from size difference coupled with other factors, such as particle density and friction coefficients (for example, glass particles are rotated with small sand particles).

Since the axial velocity field and radial segregation are keys to axial segregation, a further study of these issues is needed. The axial flow is related to granular rheology, which is poorly understood currently due to the discrete nature of granular materials even for a simple case: shearing motion of the mono-disperse chute flow (Jop *et al.*, 2006). The study of radial segregation sometimes is also very complicated (Jain *et al.*, 2005*b*; Meier *et al.*, 2008) since many parameters influence the radial segregation pattern: particle size, density, frictional coefficient, tumbler diameter, tumbler rotational speed, fill level, particle fill fraction, *etc.* The regular radial core of small particles can evolve to complicated streak patterns under certain fill levels and rotational speeds of the tumbler (Hill *et al.*, 2005), and the streaks coarsening may occur in long runs (Meier *et al.*, 2008). The capability of discrete element method to explicitly capture the information of individual species makes it possible to investigate the driving force for transient streak coarsening.

The granular mixing and segregation in noncircular tumblers has attracted much attention in recent years due to the possibility of chaotic advection, for example, in the case of radial segregation in quasi-2D square tumblers (Jain *et al.*, 2005*a*; Cisar *et al.*, 2006, 2007). However, there is no report about the simulation of mixing and segregation in noncircular tumblers using discrete element method. DEM may yield clues about the effect of the tumbler geometry on the mixing efficiency of mono-disperse granular system and the segregation patterns (both radial and axial) for bi-disperse systems.

In this thesis, we only investigated the physics of dry granular systems. Another extension beyond the current work is the study of solid-fluid multiphase flows, which are likely to be encountered in nature and industrial applications. The conventional way to model multiphase flows is from the Eulerian-Eulerian viewpoint: both solid and fluid phases are treated as continuum media and the interaction between the two phases is incorporated by drag force correlations, which depend on the local relative velocity of the phases and the local solid's volume fraction. The drawback of this method is that it does not adequately model the details of particle-particle and particle-fluid interactions. The coupling of the discrete element method and continuum Computational Fluid Dynamics (CFD) (van der Hoef *et al.*, 2008) was first introduced by Tsuji *et al.* (1993), which is often termed the Lagrangian-Eulerian model. In this model, the motion of discrete solids or particles phase is obtained by discrete element method which applies Newton's laws of motion to every particle and the flow of continuum fluid is described by the local averaged Navier-Stokes equations that can be solved by traditional Computational Fluid Dynamics. The interactions between the fluid phase and solids phase is modeled by use of Newton's third law. So the direct incorporation of CFD into DEM provides a promising way to study the physics of liquid granular systems (LGS), such as mixing and segregation in slurries.

Because the large number of particles is needed to reproduce the physics of a real granular system and very small time steps are needed to model the particle collisions, it is desirable to take advantage of parallel computation for DEM simulations. For instance, to model axial segregation in long tumblers, we could divide the flow field in the axial

direction of the tumbler into several subdomains and assign the computation work to separate processors.

## References

- ALEXANDER, A., MUZZIO, F. J. & SHINBROT, T. 2004 Effects of scale and inertia on granular banding segregation. *Granular Matter* **5**, 171–175.
- ALLEN, M. P. & TILDESLEY, D. J. 2000 *Computer Simulation of Liquids*. Oxford University Press.
- ARANSON, I. S. & TSIMRING, L. S. 1999 Dynamics of axial separation in long rotating drums. *Phys. Rev. Lett.* **82**, 4643–4646.
- ARANSON, I. S., TSIMRING, L. S. & VINOKUR, V. M. 1999 Continuum theory of axial segregation in a long rotating drum. *Phys. Rev. E* **60**, 1975–1987.
- ARNDT, T., SIEGMANN-HEGERFELD, T., FIEDOR, S. J., OTTINO, J. M. & LUEPTOW, R. M. 2005 Dynamics of granular band formation: long-term behavior in slurries, parameter space, and tilted cylinders. *Phys. Rev. E* **71**, 011306.
- BAK, P., TANG, C. & WIESENFELD, K. 1987 Self-organized criticality: An explanation of  $1/f$  noise. *Phys. Rev. Lett.* **59**, 381–384.
- BAXTER, G. W. & BEHRINGER, R. P. 1990 Cellular Automata models of granular flow. *Phys. Rev. A* **42**, 1017–1020.
- BAXTER, G. W. & BEHRINGER, R. P. 1991 Cellular Automata models for the flow of granular materials. *Physica D* **51**, 465–471.
- BIELLENBERG, J. R., GLADYSZ, G. M. & GRAHAM, A. L. 2007 A parametric study of axial segregation in granular systems. *Chem. Eng. Sci.* **62**, 4177–4181.

- BOATENG, A. A. & BARR, P. V. 1997 Granular flow behaviour in the transverse plane of a partially filled rotating cylinder. *J. Fluid Mech.* **330**, 223–249.
- BRIDGWATER, J., SHARPE, N. W. & STOCKER, D. C. 1969 Particle mixing by percolation. *Trans. Inst. Chem. Eng.* **47**, T114.
- BUCHHOLTZ, V. & PÖSCHEL, T. 1994 Numerical investigations of the evolution of sand-piles. *Physica A* **202**, 390.
- CANTELAUBE, F. & BIDEAU, D. 1995 Radial segregation in a 2d drum: an experimental analysis. *Europhys. Lett.* **30**, 133–138.
- CANTELAUBE, F., BIDEAU, D. & ROUX, S. 1997 Kinetics of segregation of granular media in a two-dimensional rotating drum. *Powder Technology* **93**, 1–11.
- CAPRIHAN, A. & SEYMOUR, J. D. 2000 Correlation time and diffusion coefficient imaging: application to a granular flow system. *J. Magn. Reson.* **144**, 96–107.
- CHAPMAN, S. J. 2003 *Fortran 90/95 for Scientists and Engineers*. McGraw-Hill.
- CHEN, P., OTTINO, J. M. & LUEPTOW, R. M. 2008a Inversion of band patterns in spherical tumblers. *submitted to Phy. Rev. Lett.* .
- CHEN, P., OTTINO, J. M. & LUEPTOW, R. M. 2008b Subsurface granular flow in rotating tumblers: A detailed computational study. *Phy. Rev. E* **78**, 021303.
- CHOO, K., BAKER, M. W., MOLTENO, T. C. A. & MORRIS, S. W. 1998 Dynamics of granular segregation patterns in a long drum mixer. *Phys. Rev. E.* **58**, 6115–6123.
- CHOO, K., MOLTENO, T. C. A. & MORRIS, S. W. 1997 Traveling granular segregation patterns in a long drum mixer. *Phys. Rev. Lett.* **79**, 2975–2978.
- CISAR, S. E., LUEPTOW, R. M. & OTTINO, J.M. 2007 Geometric effects of mixing in 2D granular tumblers using discrete models. *AIChE J.* **53**, 1151–1158.

- CISAR, S. E., UMBANHOWAR, P. B. & OTTINO, J.M. 2006 Radial granular segregation under chaotic flow in two-dimensional tumblers. *Phys. Rev. E* **74**, 051305.
- CLEARY, P. W. 2000 DEM simulation of industrial particle flows: case studies of dragline excavators, mixing in tumblers and centrifugal mills. *Powder technology* **109**, 83–104.
- CLEMENT, E., RAJCHENBACH, J. & DURAN, J. 1995 Mixing of a granular material in a bidimensional rotating drum. *Europhys. Lett.* **30**, 7–12.
- CUNDALL, P. A. & STACK, D. L. 1979 A discrete numerical model for granular assemblies. *Geotechnique* **29**, 47–65.
- DONALD, M. B. & ROSEMAN, B. 1962 Mechanics in horizontal drum mixer. *Br. Chem. Eng.* **4**, 749.
- DRAKE, T. G. & WALTON, O. R. 1995 Comparison of experimental and simulated grain flows. *J. Appl. Mech.* **62**, 131–135.
- DUKE, T. A. J., BARKER, G. C. & MEHTA, A. 1990 A Monte Carlo study of granular relaxation. *Europhys. Lett.* **13**, 19.
- DURAN, J. 2000 *Sands, Powders, and Grains*. New York: Springer.
- DURY, C. M. & RISTOW, G. H. 1997 Radial segregation in a two-dimensional rotating drum. *J. Phys. I France* **7**, 737–745.
- DURY, C. M. & RISTOW, G. H. 1998 Boundary effects on the angle of repose in rotating cylinders. *Phys. Rev. E* **57**, 4491–4497.
- DURY, C. M. & RISTOW, G. H. 1999a Competition of mixing and segregation in rotating cylinders. *Phys. Fluids* **11**, 1387–1394.
- DURY, C. M. & RISTOW, G. H. 1999b Radial segregation through axial migration. *Europhys. Lett.* **48**, 60–65.

- ELPERIN, T. & VIKHANSKY, A. 1999 Mechanism of the onset of axial segregation in a rotating cylindrical drum filled with binary granular mixtures. *Phys. Rev. E* **60**, 1946–1950.
- FIEDOR, S. J. 2006 Dynamics of segregation of dry and liquid granular systems in quasi-two-dimensional (2d) and long (2d+1) tumblers. PhD thesis, Northwestern University.
- FIEDOR, S. J. & OTTINO, J. M. 2003 Dynamics of axial segregation and coarsening of dry granular materials and slurries in circular and square tubes. *Phys. Rev. Lett.* **91**, 244301.
- FITT, A. D. & WILMOTT, P. 1992 Cellular-automaton model for segregation of a two-species granular flow. *Phys. Rev. A* **45**, 2383–2388.
- FRETTE, V. & STAVANS, J. 1997 Avalanche-mediated transport in a rotated granular mixture. *Phys. Rev. E* **56**, 6981–6990.
- FUKUSHIMA, E. 1999 Nuclear magnetic resonance as a tool to study flow. *Annu. Rev. Fluid Mech.* **31**, 95–123.
- GALLAS, J. A. C., HERRMANN, H. J., & SOKOLOWSKI, S. 1992 Convection cells in vibrating granular media. *Phys. Rev. Lett.* **69**, 1371–1374.
- GILCHRIST, J. F. & OTTINO, J. M. 2003a Competition between chaos and order: Mixing and segregation in a spherical tumbler. *Phys. Rev. E* **68**, 061303.
- GILCHRIST, J. F. & OTTINO, J. M. 2003b Competition between chaos and order: Mixing and segregation in a spherical tumbler. *Phys. Rev. E* **68**, 061303.
- GOLDSMITH, W. 2001 *Impact: The Theory and Physical Behaviour of Colliding Solids*. Courier Dover Publications.
- HAFF, P. K. 1983 Grain flow as a fluid-mechanical phenomenon. *J. Fluid Mech.* **134**,

401–430.

- HAFF, P. K. & WERNER, B. T. 1986 Computer simulation of the mechanical sorting of grains. *Powder technology* **48**, 239–245.
- HENEIN, H., BRIMACOMBE, J. K. & WATKINSON, A. P. 1983 Experimental study of transverse bed motion in rotary kilns. *Metallurgical Transactions B* **14**, 191–205.
- HERTZ, H. 1882 Ueber die berührung fester elastischer körper. *J. für die reine und angew. Math.* **92**, 1–15.
- HERTZSCH, J. M., SPAHN, F. & BRILLIANTOV, N. V. 1995 On low-density collisions of viscoelastic particles. *J. Phys. II France* **925**, 1725.
- HILL, K. M., CAPRIHAN, A. & KAKALIOS, J. 1997*a* Axial segregation of granular media rotated in a drum mixer: Pattern evolution. *Phys. Rev. E* **56**, 4386–4393.
- HILL, K. M., CAPRIHAN, A. & KAKALIOS, J. 1997*b* Bulk segregation in rotated granular material measured by magnetic resonance imaging. *Phys. Rev. Lett.* **78**, 50–53.
- HILL, K. M., GIOIA, G., AMARAVADI, D. & WINTER, C. 2005 Moon patterns, sun patterns, and wave breaking in rotating granular mixtures. *Complexity* **10**, 79–86.
- HILL, K. M. & KAKALIOS, J. 1994 Reversible axial segregation of binary mixtures of granular materials. *Phys. Rev. E* **49**, R3610.
- HILL, K. M. & KAKALIOS, J. 1995 Reversible axial segregation of rotating granular media. *Phys. Rev. E* **52**, 4393–4400.
- HILL, K. M., KHAKHAR, D. V., GILCHRIST, J. F., MCCARTHY, J. J. & OTTINO, J. M. 1999 Segregation-driven organization in chaotic granular flows. *Proc. Natl. Acad. Sci. U.S.A.* **96**, 11701–11706.
- VAN DER HOEF, M. A., VAN SINT ANNALAND, M., DEEN, N. G. & KUIPERS, J. A. M.

- 2008 Numerical simulation of dense gas-solid fluidized beds: A multiscale modeling strategy. *Annu. Rev. Fluid Mech.* **40**, 47–70.
- JAEGER, H. M. & NAGEL, S. R. 1992 Physics of the granular state. *Science* **255**, 1523–1531.
- JAIN, N., KHAKHAR, D. V., LUEPTOW, R. M. & OTTINO, J. M. 2001 Self-organization in slurries. *Phys. Rev. Lett.* **86**, 3771–3774.
- JAIN, N., OTTINO, J. M. & LUEPTOW, R. M. 2002 An experimental study of the flowing granular layer in a rotating tumbler. *Phys. Fluids* **14**, 572–582.
- JAIN, N., OTTINO, J. M. & LUEPTOW, R. M. 2005*a* Combined size and density segregation and mixing in noncircular tumblers. *Phys. Rev. E* **71**, 051301.
- JAIN, N., OTTINO, J. M. & LUEPTOW, R. M. 2005*b* Regimes of segregation and mixing in combined size and density granular systems: an experimental study. *Granular Matter* **7**, 69–81.
- JENKINS, J. T. & SAVAGE, S. B. 1983 A theory for the rapid flow of identical, smooth, nearly elastic, spherical particles. *J. Fluid Mech.* **130**, 187–202.
- JOHNSON, K. L. 1989 *Contact Mechanics*. Univ. Press, Cambridge.
- JOHNSON, P. C. & JACKSON, R. 1987 Frictional-collisional constitutive relations for granular materials, with application to plane shearing. *J. Fluid Mech.* **176**, 67–93.
- JOP, P., FORTERRE<sup>1</sup>, Y. & POULIQUEN<sup>1</sup>, O. 2006 A constitutive law for dense granular flows. *Nature* **441**, 727–730.
- JUAREZ, G., OTTINO, J. M. & LUEPTOW, R. M. 2008 Dynamics of granular segregation patterns in a long drum mixer. *Phys. Rev. E* **78**, 031306.
- KHAKHAR, D. V., MCCARTHY, J. J. & OTTINO, J. M. 1997 Radial segregation of

- granular mixtures in rotating cylinders. *Phys. Fluids* **9**, 3600–3614.
- KHAKHAR, D. V., ORPE, A. V. & OTTINO, J. M. 2001 Continuum model of mixing and size segregation in a rotating cylinder: concentration-flow coupling and streak formation. *Powder technology* **116**, 232–245.
- KHAN, Z. S., TOKARUK, W. A. & MORRIS, S. W. 2004 Oscillatory granular segregation in a long drum mixer. *Europhys. Lett.* **66**, 212–218.
- KOMATSU, T. S., INAGAKI, S., NAKAGAWA, N. & NASUNO, S. 2001 Creep motion in a granular pile exhibiting steady surface flow. *Phys. Rev. Lett.* **86**, 1757–1760.
- LI, H. M. & MCCARTHY, J. J. 2005 Phase diagrams for cohesive particle mixing and segregation. *Phys. Rev. E* **71**, 021305.
- LUN, C. K. K., SAVAGE, S. B. & JEFFREY, D. J. 1984 Kinetic theories for granular flow: inelastic particles in couette flow and slightly inelastic particles in a general flowfield. *J.Fluid Mech.* **140**, 223–256.
- MAKSE, H. A., HAVLIN, S., KING, R. K. & STANLEY, H. E. 1997 Spontaneous stratification in granular mixtures. *Nature* **386**, 379–381.
- MANEVAL, J. E., HILL, K. M., SMITH, B. E., CAPRIHAN, A. & FUKUSHIMA, E. 2005 Effects of end wall friction in rotating cylinder granular flow experiments. *Granular Matter* **7**, 199–202.
- MCCARTHY, J. J. & OTTINO, J. M. 1998 Particle dynamics simulation: a hybrid technique applied to granular mixing. *Powder Technology* **97** (2), 91–99.
- MEIER, S. W. 2008 Mixing and segregation of granular materials: A dynamical systems approach. PhD thesis, Northwestern University.
- MEIER, S. W., BARREIRO, D. A. MELANI, OTTINO, J. M. & LUEPTOW, R. M. 2008

- Coarsening of granular segregation patterns in quasi-two-dimensional tumblers. *Nature Physics* **4**, 244–248.
- MEIER, S. W., LUEPTOW, R. M. & OTTINO, J. M. 2007 A dynamical systems approach to mixing and segregation of granular materials in tumblers. *Advances in Physics* **56**, 757–827.
- MIDI, G. D. R. 2004 On dense granular flows. *Eur. Phys. J. E* **14** (4), 341–365.
- MINDLIN, R. D. 1949 Compliance of elastic bodies in contact. *J. Appl. Mech.* **16**, 256–270.
- MOAKHER, M., SHINBROT, T. & MUZZIO, F. J. 2000 Experimentally validated computations of flow, mixing and segregation of non-cohesive grains in 3d tumbling blenders. *Powder technology* **109**, 58–71.
- MULLIER, M., TÜZÜN, U. & WALTON, O. R. 1991 A single-particle friction cell for measuring contact frictional properties of granular materials. *Powder technology* **65**, 61.
- NAKAGAWA, M. 1994 Axial segregation of granular flows in a horizontal rotating cylinder. *Chem. Eng. Sci.* **49**, 2540–2544.
- NAKAGAWA, M., ALTOBELLI, S. A., CAPRIHAN, A., FUKUSHIMA, E. & JEONG, E. K 1993 Non-invasive measurements of granular flows by magnetic resonance imaging. *Experiments in Fluids* **16**, 54–60.
- ORPE, A. V. & KHAKHAR, D. V. 2004 Solid-fluid transition in a granular shear flow. *Phys. Rev. Lett.* **93**, 068001–1–068001–4.
- ORPE, A. V. & KHAKHAR, D. V. 2007 Rheology of surface granular flows. *J. Fluid. Mech.* **571**, 1–32.

- OTTINO, J. M. 1989 *The Kinematics of Mixing: Stretching, Chaos, and Transport*. Cambridge University Press.
- OTTINO, J. M. & KHAKHAR, D. V. 2000 Mixing and segregation of granular materials. *Annu. Rev. Fluid Mech.* **32**, 55–91.
- OYAMA, Y. 1939 *Bull. Inst. Phys. Chem. Res. (Tokyo)* **18**, 600.
- PARKER, D. J., DIJKSTRA, A. E., MARTIN, T. W. & SEVILLE, J. P. K. 1997 Positron emission particle tracking studies of spherical particle motion in rotating drums. *Chem. Eng. Sci.* **52**, 2011–2022.
- POHLMAN, N. A., MEIER, S. W., LUEPTOW, R. M. & OTTINO, J. M. 2006*a* Surface velocity in three-dimensional granular tumblers. *J. Fluid. Mech.* **560**, 355–368.
- POHLMAN, N. A., OTTINO, J. M. & LUEPTOW, R. M. 2006*b* End-wall effects in granular tumblers: from quasi-2d flow to three-dimensional flow. *Phys. Rev. E* **74**, 031305.
- PÖSCHEL, T. 1993 Granular material flowing down an inclined chute: A molecular dynamics simulation. *J. Phys. II France* **3**, 27.
- RAPAPORT, D. C. 2002 Simulational studies of axial granular segregation in a rotating cylinder. *Phys. Rev. E* **65**, 061306.
- RAPAPORT, D. C. 2004 *The Art of Molecular Dynamics Simulation*. Cambridge University Press.
- RAPAPORT, D. C. 2007*a* Radial and axial segregation of granular matter in a rotating cylinder: A simulation study. *Phys. Rev. E* **75**, 031301.
- RAPAPORT, D. C. 2007*b* Simulated three-component granular segregation in a rotating drum. *Phys. Rev. E* **76**, 041302.

- RISTOW, G. H. 1994 Particle mass segregation in a two-dimensional rotating drum. *Europhys. Lett.* **28**, 97–101.
- RISTOW, G. H. 1996 Dynamics of granular materials in a rotating drum. *Europhys. Lett.* **34**, 263–268.
- RISTOW, G. H. 2000 *Pattern Formation in Granular Materials*. Berlin: Springer-Verlag.
- RISTOW, G. H. & HERRMANN, H. J. 1994 Density patterns in two-dimensional hoppers. *Phys. Rev. E* **50**, R5–R8.
- RISTOW, G. H., RIGUIDEL, F. X. & BIDEAU, D. 1994 Different characteristics of the motion of a single particle on a bumpy inclined line. *J. Phys. I France* **4**, 1161.
- ROSATO, A. D., PRINZ, F., STRANDBURG, K. J. & SWENDSEN, R. H. 1986 Monte Carlo simulation of particulate matter segregation. *Powder Technology* **49**, 59.
- ROSATO, A. D., STRANDBURG, K. J., PRINZ, F. & SWENDSEN, R. H. 1987 Why the Brazil nuts are on top: Size segregation of particulate matter by shaking. *Phys. Rev. Lett.* **58**, 1038.
- SANTOMASO, A., OLIVI, M. & CANU, P. 2004 Mechanics of mixing of granular materials in drum mixers under rolling regime. *Chem. Eng. Sci.* **59**, 3269–3280.
- SAVAGE, S. B. 1982 Granular flows at high shear rates. In *Theory of Dispersed Multiphase Flow* (ed. R. Meyer), pp. 339–358. Academic Press, New York.
- SAVAGE, S. B. 1993 Disorder, diffusion and structure formation in granular flow. In *Disorder and Granular Media* (ed. D. Bideau & A. Hansen), pp. 255–285. Elsevier Science.
- SAVAGE, S. B. & LUN, C. K. K. 1988 Particle size segregation in inclined chute flow of dry cohesionless granular solids. *J. Fluid Mech.* **189**, 311–335.

- SCHAFFER, J., DIPPEL, S. & WOLF, D. E. 1996 Force schemes in simulations of granular materials. *J. Phys. I France* **6**, 5–20.
- SEVERSON, B. L., SNURR, R. Q. & OTTINO, J. M. 2007 Granular mixtures: Analogy with chemical solution thermodynamics. *J. Chem. Phys.* **127**, 174902–20.
- SHOICHI, S. 1998 Molecular-dynamics simulations of granular axial segregation in a rotating cylinder. *Mod. Phys. Lett. B* **12**, 115.
- SOCIE, B. A., UMBANHOWAR, P., LUEPTOW, R. M., JAIN, N. & OTTINO, J. M. 2005 Creeping motion in granular flow. *Phys. Rev. E* **71**, 031304.
- TABERLET, N., NEWEY, M., RICHARD, P. & LOSERT, W. 2006 On axial segregation in a tumbler: an experimental and numerical study. *J. Stat. Mech.-Theory E*. p. ARTN P07013.
- THOMAS, N. 2000 Reverse and intermediate segregation of large beads in dry granular media. *Phys. Rev. E*. **62**, 961–974.
- TSUJI, Y., KAWAGUCHI, T. & ISHIDA, T. 1992 Lagrangian numerical simulation of plug flow of cohesionless particles in a horizontal pipe. *Powder Technology* **71**, 239–250.
- TSUJI, Y., KAWAGUCHI, T. & ISHIDA, T. 1993 Discrete particle simulation of 2-dimensional fluidized-bed. *Powder Technology* **77**, 79–87.
- WOLFRAM, S. 1983 Statistical mechanics of cellular automata. *Rev. Mod. Phys.* **55**, 601.
- YANAGITA, T. 1999 Three-dimensional cellular automaton model of segregation of granular materials in a rotating cylinder. *Phys. Rev. Lett.* **82**, 3488–3491.
- YEN, K. Z. Y. & CHAKI, T. K. 1992 A dynamic simulation of particle rearrangement in powder packings with realistic interactions. *J. Appl. Phys.* **71**, 3164–3173.
- ZIK, O., LEVINE, D., LIPSON, S. G., SHTRIKMAN, S. & STAVANS, J. 1994 Rotational

induced segregation of granular materials. *Phys. Rev. Lett.* **73**, 644–647.

## APPENDIX A

**Discussion of Negative Diffusivity in Axial Segregation**

As shown in figure A.1, the rate of change of cross-sectionally averaged concentration of small particles in the slice between  $z$  and  $z + dz$ ,  $\langle C_s \rangle$ , is controlled by the net axial flow rate of small particles entering ( $Q_{s/z} = Q_{up,s/z} + Q_{down,s/z}$ ) and leaving ( $Q_{s/z+dz} = Q_{up,s/z+dz} + Q_{down,s/z+dz}$ ) this slice. That is

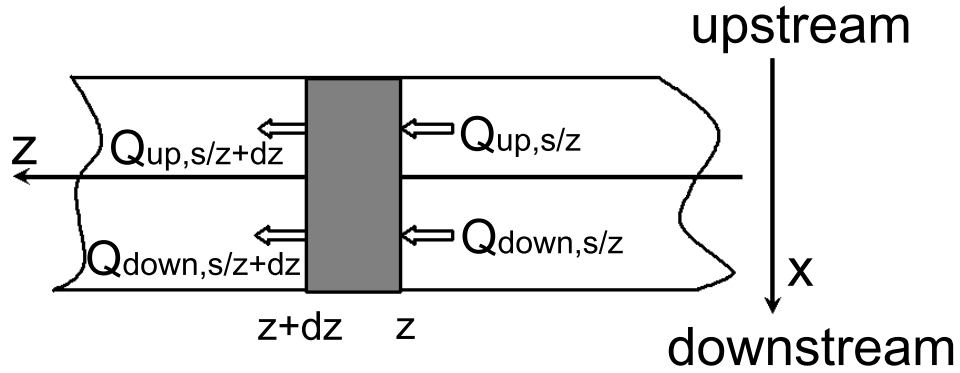


Figure A.1. Illustration of axial transport during axial segregation in cylindrical tumblers.

$$(A.1) \quad \frac{\partial \langle C_s \rangle}{\partial t} = -\frac{\partial Q_s}{A \partial z} = -\frac{\partial (\langle C_s w_s \rangle)}{\partial z} = -\frac{\partial (\langle C_s \rangle \langle w_s \rangle)}{\partial z},$$

where  $A$  is the area of cross sections (constant for cylindrical tumblers).  $C_s$  and  $w_s$  are the local concentration and axial velocity of small particles.  $\langle w_s \rangle = \langle C_s w_s \rangle / \langle C_s \rangle$

is the cross-sectionally averaged axial velocity weighted according to local volume fraction of small particles.

We can rewrite  $\langle C_s \rangle \langle w_s \rangle = \langle C_s \rangle \langle w \rangle + \langle C_s \rangle (\langle w_s \rangle - \langle w \rangle)$ , where  $w$  is the local average velocity of the mixture and  $\langle w \rangle$  is its cross-sectionally averaged value.  $\langle C_s \rangle \langle w \rangle$  represents the cross-sectionally averaged, convective axial flow of small particles moving with the mass center of the mixture ( $\langle w \rangle$ );  $\langle C_s \rangle (\langle w_s \rangle - \langle w \rangle)$  is similar to the molecular diffusion flux in a diffusion process, representing the axial flow of small particles with respect to  $\langle w \rangle$ . So, analogous to the diffusion process, we may write  $\langle C_s \rangle (\langle w_s \rangle - \langle w \rangle) = -K \partial \langle C_s \rangle / \partial z$  using Fick's first law of diffusion, where  $K$  is an effective diffusivity over the entire cross section to characterize this diffusion flux. Then equation A.1 can be written as

$$(A.2) \quad \frac{\partial \langle C_s \rangle}{\partial t} + \frac{\partial (\langle w \rangle \langle C_s \rangle)}{\partial z} = \frac{\partial}{\partial z} \left( K \frac{\partial \langle C_s \rangle}{\partial z} \right).$$

From figure 4.8 we know the axial flow of the mixture in the upstream and downstream portions nearly balance each other, so the cross-sectionally convective flow of the mixture,  $\langle w \rangle$ , is nearly zero. Therefore, the second term in the left side of equation A.2 can be neglected and we reach equation A.3 to describe the species transport in axial segregation.

$$(A.3) \quad \frac{\partial \langle C_s \rangle}{\partial t} = \frac{\partial}{\partial z} \left( K \frac{\partial \langle C_s \rangle}{\partial z} \right).$$

From equation A.3 we expect axial segregation to be a generalized diffusion process with a negative diffusivity, which is confirmed in figure 4.10 in Chapter 4.

On the other hand, we can also study the species transport of axial segregation from the local differential transport equation of small particles

$$(A.4) \quad \frac{\partial C_s}{\partial t} + \nabla \cdot (\mathbf{v} C_s) = \nabla \cdot (\mathbf{D} \frac{\partial C_s}{\partial z}).$$

Here,  $\mathbf{v} = (u, v, w)$  is local average velocity of the mixture and  $C_s$  is the local concentration of small particles. It should be noted that  $D$  is the conventional, positive normal diffusivity reflecting the random particle collisions, which tends to mix two species.

Here we decompose  $\mathbf{v}$  and  $C_s$  into cross-sectionally averaged values denoted by  $\langle \rangle$  and their deviations denoted by a prime, e.g.  $\mathbf{v} = \langle \mathbf{v} \rangle + \mathbf{v}'$  and  $C_s = \langle C_s \rangle + C'_s$ . Next we put the decomposed variables into equation A.4, and take the cross-sectional average of every term in equation A.4, noting that by definition  $\langle \mathbf{v}' \rangle = 0$ ,  $\langle C'_s \rangle = 0$ , and also  $\langle w \rangle = 0$  as mentioned above. Finally, we have:

$$(A.5) \quad \frac{\partial \langle C_s \rangle}{\partial t} + \frac{\partial \langle w' C'_s \rangle}{\partial z} = \frac{\partial}{\partial z} (D_z \frac{\partial \langle C_s \rangle}{\partial z})$$

or

$$(A.6) \quad \frac{\partial \langle C_s \rangle}{\partial t} = - \frac{\partial \langle w' C'_s \rangle}{\partial z} + \frac{\partial}{\partial z} (D_z \frac{\partial \langle C_s \rangle}{\partial z}).$$

Equation A.6 describes how the cross-sectionally averaged concentration,  $\langle C_s \rangle$ , changes with the correlation between the fluctuation of axial velocity and concentration

on the cross-section,  $\langle w' C'_s \rangle$ , and axial collisional diffusion. For a well-mixed initial condition, the radial segregation in the first several rotations introduces uneven distribution of species concentration,  $C'_s$ , on the cross section. At the same time, the frictional endwalls introduce uneven distribution of axial flow,  $w'$ , on the cross section (note  $\langle w \rangle = 0$ ). So axial segregation will occur if the flux associated with them dominates the diffusion flux. Axial segregation will stop when these two fluxes balance each other, and  $\frac{\partial \langle C_s \rangle}{\partial t}$  goes to zero. At this steady state equation A.5 becomes:

$$(A.7) \quad \frac{\partial \langle w' C'_s \rangle}{\partial z} = \frac{\partial}{\partial z} \left( D_z \frac{\partial \langle C_s \rangle}{\partial z} \right).$$

With the help of the no-flux boundary condition at the endwalls, at steady state we have

$$(A.8) \quad \langle w' C'_s \rangle = D_z \frac{\partial \langle C_s \rangle}{\partial z}.$$

That is, at the steady state, this flux is proportional to the concentration gradient and behaves as a Fickian diffusion. This is not surprising, since from equation A.3 the overall process of axial segregation behaves as a Fickian diffusion. So if we choose to model  $\langle w' C'_s \rangle$  using a diffusion coefficient,  $\langle w' C'_s \rangle = D' \frac{\partial \langle C_s \rangle}{\partial z}$  ( $D'$  is positive here to indicate this flux is along-gradient rather than counter-gradient in the normal diffusion), we then have

$$(A.9) \quad \frac{\partial \langle C_s \rangle}{\partial t} = \frac{\partial}{\partial z} [(D_z - D') \frac{\partial \langle C_s \rangle}{\partial z}].$$

Apparently, the competition between this negative diffusivity ( $-D'$ ) from differential convective flux and positive normal diffusivity ( $D_z$ ) from random particle collisions, equals to the generalized diffusivity,  $K$ , in equation A.3. If normal diffusion dominates,  $K$  is positive and the two species tend to mix, otherwise  $K < 0$  and they tend to segregate axially. From this viewpoint, it is clear that the non-uniformity of the axial velocity field and the particle concentration distribution on cross sections are two keys to the appearance of axial segregation.